POLITECNICO DI TORINO

PhD in Mechanic

XXVIII cycle

PhD Thesis

Fluid Mechanics in Innovative Food Processing Technology

Tutor

Prof. Vladimir Viktorov

Coordinator

Prof. Luigi Garibaldi

Candidate:

Md Readul Mahmud

29 April 2016

ABSTRACT

Generally, food industries employ traditional technologies and bulk devices for mixing, aeration, oxidation, emulsification and encapsulation. These processes are characterized by high energy consumption and result in high cost product, with limited diversity and usually with non-competitive quality. Moreover, the byproduct is also high. In recent years immense efforts have been dedicated to overcome these issues and major advances in food engineering have come from transfer and adaptation of knowledge from related fields such as chemical and mechanical engineering. It is well known that the majority of elements contribute to transport properties, physical and rheological behavior, texture and sensorial traits of foods are in micro-level. In this context invention at microscopic level is of critical importance to improve the existing foods quality while targeting also the development of new products.

Therefore, microfluidics has a significant role in future design, preparation and characterization of food micro-structure. The diminutive scale of the flow channels in microfluidic systems increases the surface to volume ratio and is therefore advantageous for many applications. Furthermore, high quality food products can be manufactured by means of innovative microfluidic technology characterized by less energy consumption and a continuous process in substitution to the problematic batch one.

To meet these challenges, this work is focused on main two tasks: (i) efficient micromixing, and (ii) production of microbubbles and microdroplets.

Firstly, two novel 3D split and recombine (SAR) micromixers are designed on an extensive collection of established knowledge. Mixing characteristics of two species were elucidated via experimental and numerical studies associated with microchannels at various inlet flow-rate ratios for a wide range of Reynolds numbers (1-100); at the same time, results are compared with two well-known micromixers. It was found that performances of the mixers are significantly affected by their design, inlet flow-rate ratios and Reynolds numbers. The proposed micromixers show better efficiency (more

than 90%) in all examined range of Reynolds numbers than the well-known basic mixers at each desired region; the required pressure-drop is also significantly less than that of the previous mixers. Furthermore, numerical residence time distribution (RTD) was also explored, which successfully predicts the experimental results. In a word, the presented new micromixers have advantages of high efficiency, low pressure-drop, simple fabrication, easy integration and ease for mass production.

Secondly, four micro-devices are designed for the mono-dispersed droplets and bubbles generation. Two different experimental setups were used to create water droplet in silicone oil (W/O) and air bubble in silicone oil (A/O) for continuous flow rate from 10 ml/h to 230 ml/h. The mean size of droplet and bubble as well as frequency of generation can be controlled by dispersed and continuous flow rate. Besides, squeezing and dripping flow regimes are observed inside the four devices over a broad range of Capillary numbers: 0.01~0.18. Among the examined four devices, T-1 and T-2 provide smaller droplet (100 μm) and higher production rate. Furthermore, negative pressure setup provides more robust bubble generation but positive pressure yields better production rate. In addition, droplet and bubble diameter is about four times less than the microchannel dimension, therefore small droplet and bubble can be generated spending less energy.

In summary, the investigation in this dissertation reflects that both SAR micromixers and micro-devices are very efficient and can be applied to meet the growing demands of food industries. The first part of the thesis, chapters 1 to 5, addresses state of art, design, experimental technique and results of micromixers. The second part, chapters 6 to 9, presents background, construction of devices, tests and results related to the production of microdroplets and microbubbles. Finally, chapter 10 summaries the whole presented work.

DEDICATION

To

Dear Father and Mother

ACKNOWLEDGEMENTS

I would like to express the deepest appreciation to my advisor, Professor Vladimir Viktorov, for his excellent guidance, caring, patience, and providing me with an excellent atmosphere for research work. He continually and convincingly conveys a spirit of adventure in regard to research, and an excitement in regard to learn and teach. Without his guidance and persistent help this dissertation would not have been possible.

It is impossible to adequately express my gratitude to Dr. Carmen Visconte, not only for her invaluable advice and assistance with experimental tests and theoretical data analyzing, but also for her consistent encouragement during the ups and downs of the research.

I would like to thank the coordinator, Prof. Luigi Garibaldi and the committee members, Prof. Carlo Ferraresi, Prof. Stefano Beretta, and Prof. Enrico Ravina for guiding my research for the past several years and also for the continuous help and best suggestions.

In addition, many thanks to Prof. Gaetano Maria Di Cicca for his assistance with experimental tests and generously allowing me to access his high speed camera and facilities at all hours of the day.

Very special thanks to Eng. Maurizio Vallana for his support in the construction of test bench and in providing the necessary instruments throughout the duration of my thesis.

I would also like to thank my parents and friends. They were always supporting me, encouraging me with their best wishes and stood by me in the good and bad times.

List of Publications:

1. Vladimir Viktorov, **Md Readul Mahmud** and Carmen Visconte, "**Comparative Analysis of Passive Micromixers at a Wide Range of Reynolds Numbers**", *Micromachines*, Vol. 6, 2015
2. Vladimir Viktorov, **Md Readul Mahmud** and Carmen Visconte, "**Design and Characterization of a New H-C Passive Micromixers up to Reynolds Number 100**", *Chemical Engineering research and Design,* 2015
3. Vladimir Viktorov, **Md Readul Mahmud** and Carmen Visconte, "**Numerical Study of Fluid Mixing at Different Inlet-Flow rate Ratios in Tear-drop and Chain Micromixers compared to a New H-C passive Micromixer**", *Engineering Applications of Computational Fluid Mechanics*, vol. 10, 2016
4. Vladimir Viktorov, Carmen Visconte and **Md Readul Mahmud**, "**Analysis of a Novel Y-Y Micromixer for Mixing at a Wide range of Reynolds Numbers**", *Journal of Fluids Engineering* (*doi:*10.1115/1.4033113)

List of Conferences:

1. Vladimir Viktorov, **Md Readul Mahmud** and Carmen Visconte, "**Development and Comparative Analysis of a New C-H Split and Recombine Micromixer**", *15th European Conference on Mixing***,** Saint Petersburg, Russia, June 2015
2. Vladimir Viktorov, **Md Readul Mahmud** and Carmen Visconte, "**Numerical Analysis of Fluid Mixing in Three Split and Recombine Micromixers at Different Inlets Flow Rate Ration**", 2nd *World Congress on Mechanical, chemical, and Material Engineering***,** Barcelona, Spain, July 2015
3. **Md Readul Mahmud,** Vladimir Viktorov and Carmen Visconte, "**Computational Design and Experimental validation of SAR Mixers**", *5th International Conference on Fluid Dynamics*, Dubai, UAE, April 2016

Nomenclature

C	Species mass concentration
Ca	Capillary number
C_i	Mass fraction of a species at a sample cell/pixel i
C_m	Mean mass fraction of a species at a cross-section/liquid dye at a target area
D	Diffusion coefficient of a species
ΔP	Pressure drop
d_h	Hydraulic diameter of the channel
Fo	Fourier number
i	Cell/pixel number
N	Total number of cells/pixels
P	Pressure
Pe	Peclet number
Q	Fluid flow rate
Q_c	Flow rate of continuous phase
Q_{c1}	Flow rate of secondary continuous phase
Q_d	Flow rate of dispersed phase
Re	Reynolds number
Sc	Schmidt number
St	Strouhal number
v	Fluid velocity
v_x	Component of the fluid velocity along the x direction
v_y	Component of the fluid velocity along the y direction
v_z	Component of the fluid velocity along the z direction
v_{yz}	Mean value of the secondary flow velocity
w	Width of the channel

Greek letters

η	Mixing efficiency
μ	Fluid viscosity
ρ	Fluid density
σ	Standard deviation
σ_m	Maximum standard deviation

TABLE OF CONTENTS

Chapter 1. Basic of Micromixer

Nowadays micromixers are key components for mixing in a microfluidic system (1) and their potential application is increasing every day. The diminutive scale of the flow channels in microfluidic systems increase the surface to volume ratio and is therefore advantageous for many applications (2). Scientists from a variety of disciplines, such as chemistry, biology, medicine, food and genetic engineering find microfluidic attractive because of a wide range of benefits including their low cost, fast reaction time, portability, rapid heat and mass transfer, low energy requirement, and multiplicity of design (3) (4) (5) (6).

In principle, the mixing of two or more different fluids depends on convection and diffusion. Species mixing within microfluidic devices, typically working at low Reynolds numbers is heavily dependent on molecular diffusion between layers of different concentrations (7). Therefore, full mixing of two fluids conveyed in a simple channel normally needs long time and long channel length (8). Introduction of vortexes is required to enhance mixing performance at low Reynolds numbers, which will increase the secondary flow or convection (9).

Different strategies have been developed to decrease the mixing length, time and improving chaotic advection, whereby micromixers can be classified into two broad categories: active and passive (4) (10) (11) (12). Active micromixers require an external actuation, such as periodic variation of pumping, electrokinetic instability, acoustically induced vibration, electrowetting induced merging of droplets, magneto-hydrodynamic action, small impellers, piezoelectrically vibrating membrane or integrated micro valves and pumps (13) (14) (15) (16), which makes the fabrication and the cleaning processes more complex (17). In contrast, passive mixers use the flow energy to create multi-lamellae structures, which are stretched and recombined to promote mixing by diffusion (18) (19). Passive mixer also uses different geometrical channel shape for splitting, stretching, folding and breaking of the flow, which ultimately introduce chaotic advection (20). Passive mixers are a popular choice over active mixers in chemical and biological applications since active mixing mechanisms can damage biological fluids (21).

Static mixers have been intensively studied in the last two decades not only because of their excellent performance in the field of mixing and two-phase dispersion but also because of their ability to redesign a discontinuous process into a continuous one (22). It is evident from the literature that micromixers based on the split and recombine (SAR) principle offer better mixing efficiency over other types of passive micromixers at low Reynolds numbers, even if they show high pressure drop due to their complex three-dimensional structure. At low Reynolds numbers (Re < 50), SAR mixers provide laminar flow and mixing is predominantly due to lamination of multiple streams in both horizontal and vertical directions (23). As the Reynolds numbers increase, vortexes build up inside the channels, which ultimately yield chaotic mixing (22) (24) and finally increase the mixing efficiency.

In this dissertation, we have developed two three-dimensional micromixers based on mixing principle of SAR and chaotic advection, which have advantages of high efficiency, low pressure-drop, simple fabrication and ease for mass production. The elements of the mixer are designed and connected with each other in way to stretch, split, recombine and rotate the flows. With an appropriate inlet velocity, these elements/geometries would help induce the chaotic advection or stretch flows to increase contact interface. Numerical simulations for different parameters such as novel geometrical configurations, same and different inlet flow-rate ratios are also conducted to investigate their effects on the mixing performance. Residence time distribution (RTD) is also studied to have an idea of mixing performance and time. It is a valuable tool for engineers to analyze and optimize micromixer design to fit their specific needs. The simulation model will provide valuable information to design a micromixer by choosing appropriate geometry to boost mixing performance and broaden implicational range to fit their specific needs. Experiment is also carried out to measure the fluids mixing performance and pressure drop in all micromixers at Reynolds number up to 100. The experimental results are used to verify the validity of the numerical model.

1.1 Micromixer

A micromixer is a device designed to mix two or more fluids within the dimensional constraints of the micro-scale. Micromixers reported in the literature can be classified as either active or passive mixer, depending on how they manipulate the fluid to be mixed. Active micromixer requires external forces but a passive type requires no external energy and agitation except that associated with producing the pressure drop for flow. For practical reasons, Passive micromixers are preferred

from active micromixers. Since high electric field, mechanical shearing, or generation of heat involved the active mixing, the active techniques are not suitable to employ in applications involving sensitive species (e.g. biological system).

1.2 Passive Micromixer

Passive micromixers are easy to design and construct due to their simple concept and structure. Due to their micro structure, flow is predominant laminar and mixing relies in the molecular diffusion and chaotic advection (21). These devices are designed with a channel geometry that increases the surface area between the different fluids and decreases the diffusion path between them improving molecular diffusion. By contrast, the enhancement of chaotic advection can be realized by modifying the design to allow the manipulation of the laminar flow inside the channels (4). The modified flow pattern shortens diffusion path and thus improves the mixing. The mixing performance of different passive mixers is presented in Table 1.1.

1. Parallel lamination
2. Sequential lamination (SAR)
3. Flow-focusing
4. Chaotic advection
5. Droplet
6. Injection

Table 1.1 Performance of passive micromixers in recent years (12)

Categories	Mixing Technique	Mixing Time (ms)	Mixing Length (μm)	Mixing Index	Reference
Lamination	Wedged shaped inlets	1	1	0.9	(25)
	90° rotation	-	-	0.95	(26)
Zigzag channels	Elliptic-shape barriers	-	10,000	0.96	(27)
3-D serpentine structure	Folding structure	489	-	0.01	(28)
	Creeping structure	-	-	0.015	(29)
	Stacked shim structure	-	-	-	(30)
	Multiple splitting, stretching and recombining flows	-	-	-	(31)
	Unbalanced driving force	-	815ψ	0.91	(32)
Embedded barriers	SMX	-	-	-	(33)
	Multidirectional vortices	-	4255	0.72	(34)
Twisted channels	Split-and-recombine	730	96,000	~1	(35)
Surface-chemistry	shape	-	1000	0.98	(36)
	T-/Y- mixer	-	1000	0.95	(37)

1.2.1 Parallel Lamination

The most common and basics design of parallel lamination mixers are T and Y shaped channel mixers (38) (39) (40) (41) (42) (43) as shown in Figure 1.1. A simple T mixer is made of two channel connected in 90˚ which has two inputs and one output. These mixers can be improved by using more complicated design that split the inlets main stream into n sub-streams and then rejoin them to form a laminated stream. There is different way to feed the fluids in to the mixers which let to different geometrical shape of mixers (21) (32) (44) (45) as shown in Figure 1.2.

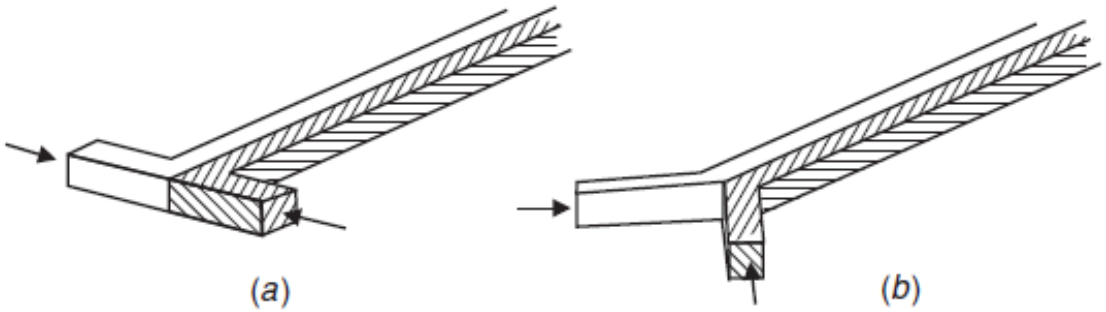

Figure 1.1 Parallel lamination micromixers: (a) basic T-mixer, (b) Y-mixer (4)

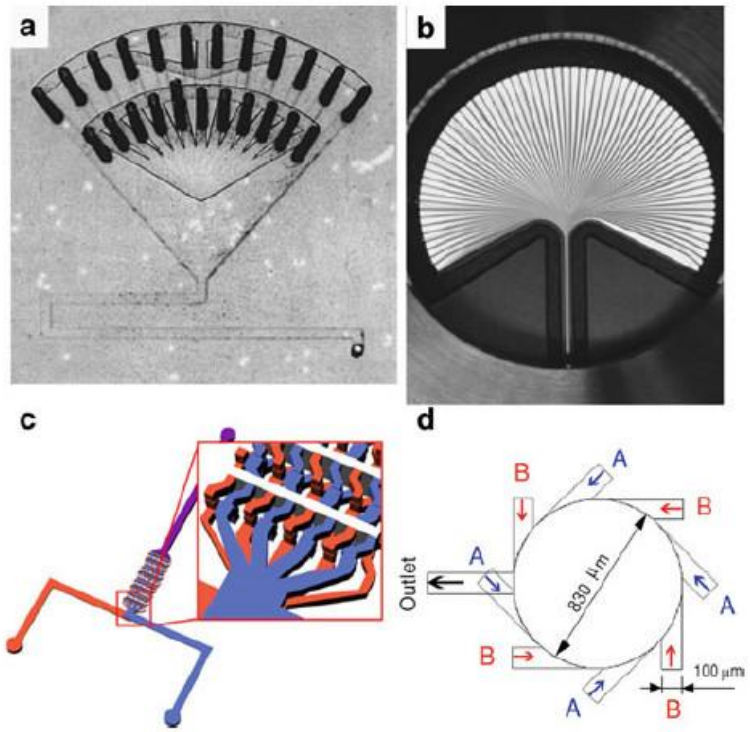

Figure 1.2 Parallel lamination micromixers: (a) Bifurcation-type feeds, (b) Interdigital-type feeds, (c) Chessboard mixer (d) Circular mixer (21)

1.2.2 Sequential Lamination (SAR)

Sequential lamination micromixers are also called split-and-recombine (SAR) micromixers. Split and recombine process in the micromixers rely on the concept of repeated inter-layering of multiple parallel streams which exponential increase the contact surface area and decrease the length path to achieve a shorter mixing time. The difference between the two types of micromixers is the method used to achieve lamination of the fluid to be mixed. Lamination in SAR micromixers is obtained by sequential processes of splitting and rejoining the fluids (46) (47) (48) (49) (Figure 1.3).

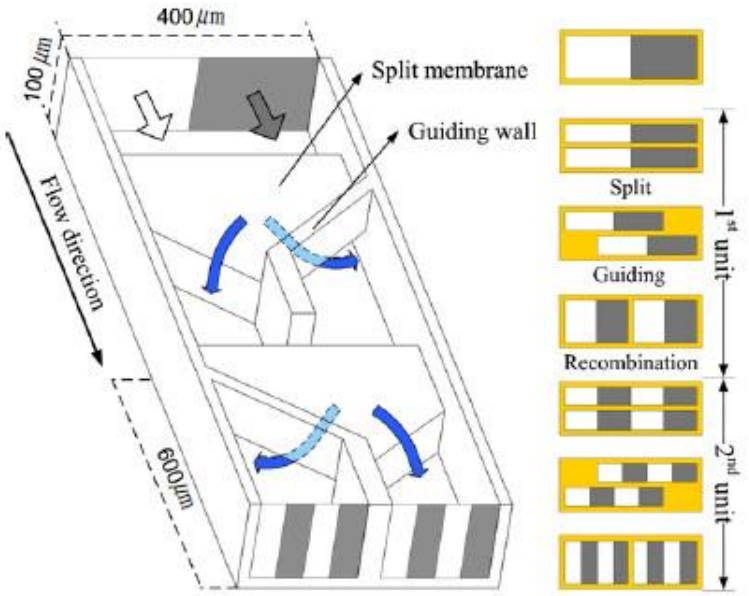

Figure 1.3 Sequential lamination mixer: (a) Mixing unit of a SAR micromixer, (b) the corresponding cross-sectional view of the flow (46)

Fang et al. (50) proposed a SAR micromixer incorporating chaotic advection features named (SAR μ-reactor design) to mix fluids in a wide range of Reynolds number and viscosity. Another way of obtaining a SAR-like effect within a planar microfluidic chip was introduced by Sudarsan et al. (51). It works with a multistep action: initially, this geometry leveraged the generation of Dean vortices that arise in the vertical plane of curved channels to induce a 90° rotations in the fluid. At this point, the fluid is divided into many sub-streams that undergo the same 90° rotations in the fluid. At the end, the transformed sub-streams rejoin to create a multi-lamellae arrangement.

1.2.3 Flow-focusing

Another way to reduce the diffusion length and increase the mixing is hydrodynamic focusing (52) (53) (54) (55) as shown in Figure 1.4. The basic design for hydrodynamic focusing is a long microchannel with three inlets. In hydrodynamic focusing, a central sample solution (supplied from the middle inlet) flows within the sheath of outer fluids (supplied from the side inlets), which constrain laterally the inner sample flow to achieve a smaller stream and the inner lamination width. The extent of the width decrease of the focused stream depends on the volumetric flow rate ratio between the sample flow and sheath flows. The greater the flow rate difference, the greater the degree of width reduction. Mixing time is inversely proportional to the square of the diffusion path length (in this case represented by the focused stream width), therefore, decreasing the stream width results in faster mixing.

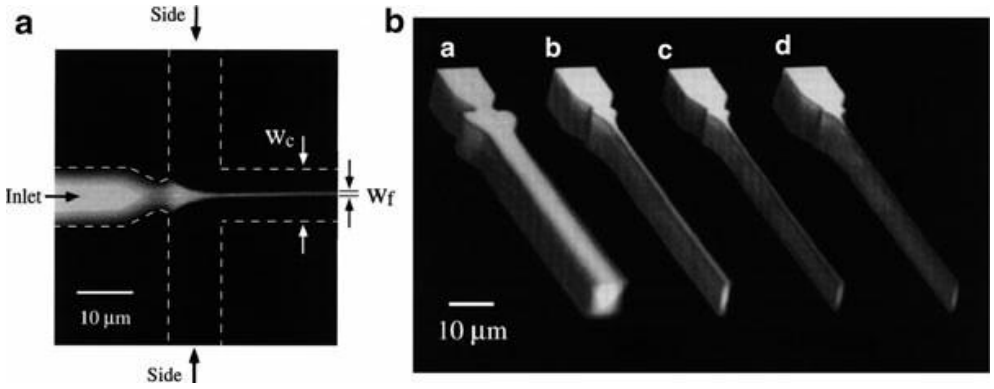

Figure 1.4 (a) Focusing enhanced mixer. (b) Effect of ratio a of the side pressure to the inlet pressure on the width of the focused stream: (a) 0.5, (b) 1.0, (c) 1.1, and (d) 1.2 (52)

1.2.4 Chaotic Advection

Advection is another important form of mass transfer in flows with a low Reynolds number. However, advection is often parallel to the main flow direction, and is not useful for the transversal mixing process. The so called chaotic advection can improve mixing significantly. Generally, chaotic advection can be generated by special geometries in the mixing channel (see Figure 1.5) or induced by an external force. These generated transverse flow components cause an exponential growth of the interfacial area and a corresponding decrease in the striation thickness, which can significantly improve mixing. The basic idea is the modification of the channel shape for splitting, stretching, folding and breaking of the flow over the cross-sectional channel. This effect can be achieved using 2D curved (56) (57) (58) or 3D convoluted channels (59) (60) and by inserting obstacles (61) and bas-reliefs on the channel walls (62) (63).

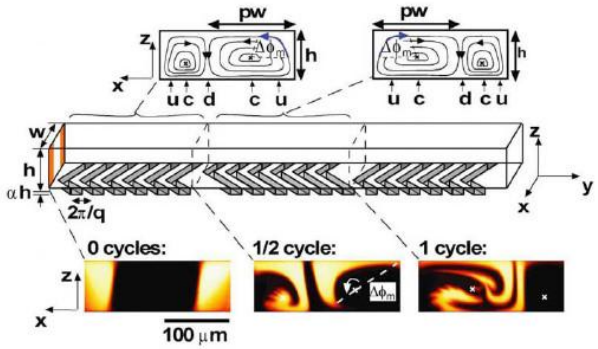

Figure 1.5 Staggered herringbone micromixer for the generation of chaotic flows with schematic and real flow patterns (64)

1.2.5 Injection

The concept of injection-type micromixer (65) (66) (67) is similar to parallel lamination, except that only one of the inlet flow is split into multiple layers and then injected into the flowing stream. In fact, arrays of the micro-nozzles are used to inject one fluid on top of the other (see Figure 1.6) to increase diffusing mixing. The mixer is first filled with one sample and the second fluid is injected directly into the first fluid via micro-nozzles. These plumes increase the contact surface and decrease the mixing path. Mixing efficiency can be improved significantly.

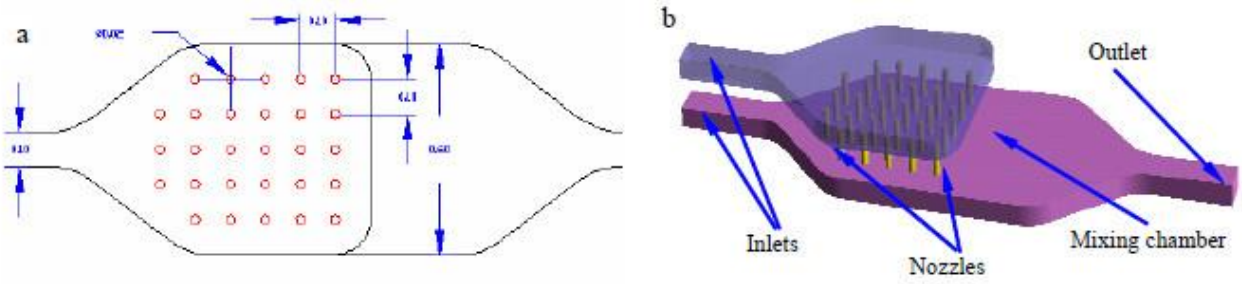

Figure 1.6 2D layout of micronozzles and 3D schematic model of an injection mixer (65)

1.2.6 Droplet

To overcome complexities associated with fabrication of 3D structure, micromixers based on droplet mixing are suggested. Fluid elements trapped in droplets get rapidly intermixed because of the attendance of an internal flow field which is the characteristic of motive droplets. Generally speaking, mixing inside microdroplets is enhanced by a reduction in diffusion length and by the intimate contact between the fluids to be mixed due to the geometrical confinement of the droplet itself. Furthermore, the contact between the droplet surface and the channel walls causes the generation of recirculating flow within the droplet fluid. When the droplet is transported through a straight channel, these flows are generated in the two halves of the channel. Each flow pattern

consists of two counter-circulating flows. This flow pattern provides a mixing of the two halves; however, mass transport is not activated between the two halves that thus remain separated and unmixed (21). By varying the viscosity of the two phases, the relative flow rates, or the channel dimension it is possible to tune the dimensions of the produced microdroplets (68) (69) (70). An impediment of this technique is that since immiscible liquids are needed to generate droplets, an additional separation step would be required if the mixed elements inside the droplet are to be extracted.

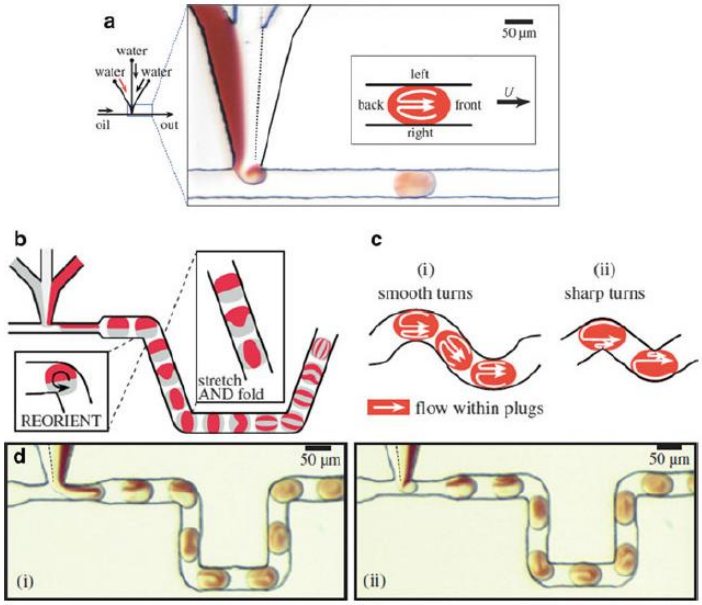

Figure 1.7 Mixing in microdroplets flowing in a microchannel: (a) Recirculation flow generated in a straight channel. (b, c) Mixing patterns generated in winding channels that causes (b) stretch, fold, and reorientation of the fluids interface and (c) asymmetrical recirculation patterns in the droplet halves. (d) Experimental results showing the chaotic advection thus generated in microdroplets (71)

1.3 Active Micromixers

As described previously, active micromixers rely on an external energy input to introduce perturbation within the fluid streamlines to achieve mixing. Therefore, they are categorized with respect to the type of external perturbation energy (4) (11) (12) (19):

1. Pressure field
2. Elecrokinetic
3. Eelectrodynamics
4. Dielectrophoretic
5. Electrowetting
6. Magneto-hydrodynamic

7. Acoustic
8. Thermal

In passive mixing devices, samples can typically be mixed within 55–300 ms, and hence the requirement for high device throughputs can be readily achieved (12). Besides increasing the contact area, the mixing performance can also be improved by increasing the time of contact between the multiple species. However, such schemes typically result in a lower mixing efficiency, and thus require longer mixing channel to achieve a satisfactory mixing result as presented in Table 1.2.

Table 1.2 Performance of active micromixers in recent years (12)

Categories	Mixing Technique	Mixing Time (ms)	Mixing Length (μm)	Mixing Index	Reference
Acoustic/Ultrasonic	Acoustically driven sidewall trapped microbubbles	120	650	0.025	(72)
	Acoustic streaming induced by surface acoustic wave	600	10,000	0.9	(73)
Dielectrophoretic	Chaotic advection based on Linked Twisted Map	-	1000	0.85	(74)
Electrokinetic time pulsed	Chaotic electric fields	100	Width 5.0	0.95	(75)
	Periodic electro-osmotic flow	-	200	0.88	(76)
Electrohydrodynamic force	Staggered herringbone structure	-	825	0.2	(77)
	Staggered herringbone structure	-	2300	0.5	(78)
Thermal actuation	Thermal	-	6000	-	(79)
Magneto-hydrodynamic flow	High operating frequency	1100	500	0.977	(80)
Electrokinetic instability	Low Reynolds number	-	1200	0.98	(81)
	Low Reynolds number	-	1200	0..98	(82)

1.4 Fundamental Parameters

To characterize the flow in the microchannel different dimensionless parameters such as, Reynolds number (Re), Peclet number (Pe), Strouhal number (St), Schmidt number (Sc), and Fourier number (Fo) are commonly used (11) (21).

1.4.1 Reynolds Number

The Reynolds (*Re*) number is defined as the ratio between inertial forces and viscous forces.

$$Re = \frac{inertial\ forces}{viscous\ forces} = \frac{\rho u d_h}{\mu} \qquad \textbf{1.1}$$

Where ρ and μ are the fluid density and dynamics viscosity, respectively; u is the mean velocity in the flow direction and d_h is the hydraulic diameter of the channel. Reynolds number is used to indicate the nature of the flow, i.e. it is laminar flow or turbulent flow. At low *Re* number, the viscous effects dominate inertial force and laminar flow occurs. Laminar flow is characterized by smooth and constant fluid motion, whereas turbulent flow is characterized by vortices and flow fluctuations. In the laminar flow system, fluid streams flow parallel to each other inside the micro channel and mass transfer occurs only in the direction of fluid flow as convective process. Therefore in case of laminar flow the mixing relies only on molecular diffusion (83). On the contrary, at high *Re* number the flow is dominated by inertial forces and characterized by turbulence. In a turbulent flow, the mass transport occurs mainly by convection due to the random motion of fluid in both space and time (84). There is a transitional Re range where flow goes from laminar to turbulent. The exact values of this number range are a function of many parameters, such as channel shape, surface roughness, and aspect ratio (21).

1.4.2 Peclet Number

The Peclet number represents the ratio between the mass transfer due to advection/convection and that of diffusion. Convection is dominant for higher Peclet number.

$$Pe = \frac{advection\ transport\ rate}{diffusion\ transport\ rate} = \frac{vl}{D} \qquad \textbf{1.2}$$

Where *l* is the characteristics length and *D* is the mass diffusion coefficient. For simple spherical particles, *D* can be derived by the Einstein–Stokes equation:

$$D = \frac{KT}{6\pi\mu R} \quad \textbf{1.3}$$

Where *k* is Boltzmann's constant, *T* is the absolute temperature and *R* is the radius of the particles (or molecules). The diffusion coefficient for a small molecule in water at room temperature has the typical value of 10^{-9} m^2/s (21).

1.4.3 Strouhal Number

Strouhal numbers represents the ratio between the residence time of a species and the time period of disturbance.

$$St = \frac{f d_h}{v} \quad \textbf{1.4}$$

Where f is the frequency of the disturbance action; it is generally associated with active micromixers.

1.4.4 Schmidt Number

The Schmidt number is the ratio between momentum transport and diffusive mass transport and is used to characterize fluid flows in which there are simultaneous momentum and mass diffusion convection processes. It is the ratio of the shear component for diffusivity viscosity/density to the diffusivity for mass transfer *D*. It physically relates the relative thickness of the hydrodynamic layer and mass-transfer boundary layer.

$$Sc = \frac{viscous\ diffusion\ rate}{molecular\ (mass) diffusion\ rate} = \frac{\mu}{\rho D} \quad \textbf{1.5}$$

1.4.5 Fourier Number

The average diffusion time t_{diff} over the characteristic mixing length *l*, also called the striation thickness, is represented by the Fourier number.

$$Fo = \frac{D t_{diff}}{l^2} \quad \textbf{1.6}$$

The Fourier number is usually in ranging between 0.1 and 1. The mentioned equation reveals that a very compact micromixer can be designed using sequentional lamination or chaotic advection. In general, fast mixing can be achieved with smaller mixing path and larger interfacial area. If the channel geometry is very small, the fluid molecules collide most often with the channel wall and not with other molecules.

1.5 Summary and Motivation

Designing micromixers is a challenge, because existing designs in macro-scale cannot simply be scaled down for micro-scale applications. One of the main challenges related to miniaturization is the dominance of surface effects over volume effects. Besides surface phenomena, the laminar flow condition is another challenge for designing micromixers. For many applications, the flow velocity in micromixers cannot be too high. The small size of micromixers leads to an extremely large shear stress in mixing devices, even at relatively slow flow velocities. Advection allows improved mixing in fluid flows at low Reynolds numbers. In most passive micromixers based on molecular diffusion, advection is parallel to the main flow direction. Thus, transversal transport of species relies entirely on molecular diffusion. Advection with a three-dimensional orbit can cause secondary transversal transport and significantly improve mixing. The basic design concept for the generation of advection is the modification of the channel shape for stretching, folding, and breaking of the laminar flow.

Degree of mixing is characterized by flowing of two parallel liquids and observing the minimum distance from inlet part over which they become intermixed. Foremost, results of experiments in micromixers are detected visually. In order to characterize the micromixers, this study makes use a syringe pump to inject water and blue liquid dye in the two inlets of the microchannel. The simple visual study of the color gradient during mixing is not sufficient to provide valuable data to assess the system performance; other more objective techniques are hence required. Different researchers employ different techniques to determine the efficiency of the micromixers. For instance, some research groups utilized, “top view” measurement technique, and some researchers employed confocal microscopy at the cross section of the microchannel. The situation becomes more complex when the different experimental characterization technique is further combined with the use of different fluid and different data analysis regulation. However, in order to develop advanced micromixers, the data precisely needed to be analyzed to satisfy the demands on this field. In this

thesis, we employed image-based technique to analyze the experimental data and an image analysis technique is developed to evaluate the mixing performance.

Residence time distribution (RTD) is also explored by many researchers to get the knowledge of exact prediction of yield for first order reaction and allows close estimation for reactions of order than first. In addition, the general reaction performance and mixing can be evaluated. Among other characteristics (like mixing efficiency, pressure drop) knowledge of the RTD of a certain microfluidic device would be a useful to identify the most appropriate one. In this work, RTD is investigated using the pulse input method to compute various parameters such as mean residence time, CoV, variance and skewness.

SAR mixers presented in the literatures have many limitations, such as poor mixing efficiency at low Reynolds numbers (Re<50), high pressure drop due to 3D complex structures, intricate and expensive fabrication process, difficult to maintain and to integrate into micro systems etc.

The motivation behind this work is to overcome some of these limitations. Micromixers are in a crucial need of improved method where passive micromixing can be achieved in the shortest possible distance by less energy consumption using simplified microchannel that can be easily constructed. The technique proposed for designing SAR mixers will be helpful to construct desired mixers with specific need in particular applications. This study proposes two novel passive micromixers. Mixing characteristics of two species are elucidated via experimental and numerical studies associated with microchannel at various inlet flow-rate ratios for a wide range of Reynolds numbers and results are compared with the previous well-known micromixers.

1.6 Objectives

While current passive micromixing techniques have made useful contribution in microfluidic field of research, many micromixers need channel geometries which utilize complex manufacture techniques. Although patterning surface with complicated geometry is becoming accurate, the problem appears when two patterned surfaces require be assembled, aligned, and bonded with precision. Mentioned problem is not only time consuming but also expensive to perform in the laboratories. Considering all these factors, there still exist the needs to build micromixers that achieve high micromixing performance with low energy in the shortest possible distance by using simplified microchannel.

The main purpose of this investigation is to achieve higher mixing performance with low energy consumption by exploiting splitting and recombination (SAR) process in simplified constructed microchannel. The detail objectives of this investigation are given below:

- ✓ To build new designs of microchannel using split and recombined technique with simple structure without any groves/obstacles inside.
- ✓ To inspect the fluids mixing performances via color changes, standard deviation and mixing efficiency among the selected micromixers.
- ✓ To analyze the fluids mixing performances and pressure drop via numerical simulation among the selected micromixers.
- ✓ To investigate the flow pattern of fluids and contribution of secondary flow (transverse flow) to increase the efficiency at different flow rates.
- ✓ To study the residence time distribution (RTD) to have a better understanding of the flow of the fluids.
- ✓ To perform a comparative analysis and to select the optimum design among the selected four micromixers given below:
    - Tear-drop micromixer
    - Chain micromixer
    - Y-Y micromixer
    - H-C micromixer

Chapter 2. Development of New Y-Y and H-C Micromixers

In this research, two new passive micromixers, Y-Y and H-C, were designed exploiting split, stretch, recombine, rotate and fold principle. Two well-known existing SAR micromixers, Tear-drop and Chain are also studied to have a point of reference for comparison. The geometrical structure and split-recombine, and folding mechanism inside the channel for all the mixers were presented in detail.

2.1 Tear-drop Micromixer

The basic idea and design of a Tear-drop mixer was presented in (28). A slightly modified version of the Tear-drop micromixer consisting of plate symmetrical modules was constructed and studied by Viktorov and Nimafar (85). Figure 2.1 shows the Tear-drop micromixer which is made up of four identical elements connected in series.

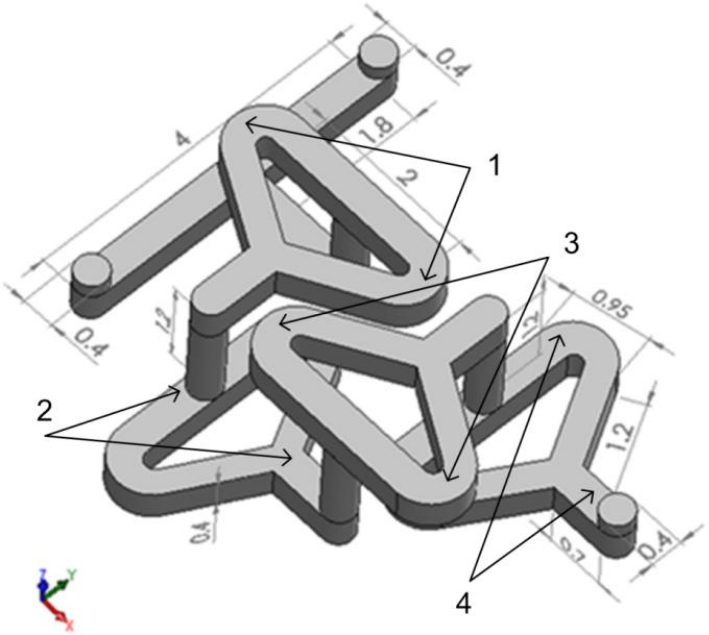

Figure 2.1 Design of the Tear-drop micromixer (all dimensions are in mm)

The Tear-drop mixer has a two-layer structure. The modules of the upper layer and lower layer are connected by simple vertical channels. Channel width and height are 0.4 mm as can be seen in figure 2.1. The inlet to the mixer is designed as a T-junction element (left side of figure).

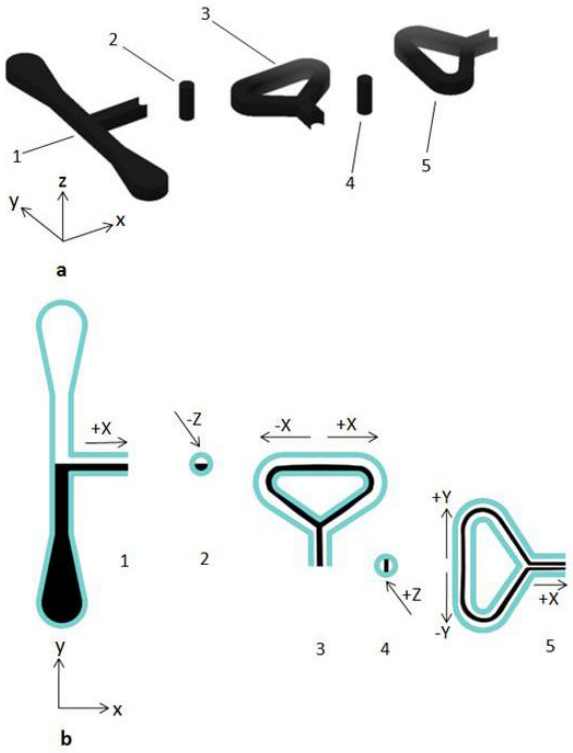

Figure 2.2 Tear-drop structural detail; (a) Tear-drop microchannel segments; (b) Sequential lamination of layers.

Figure 2.2 shows structural details of the Tear-drop micromixer. Two miscible liquids move through the entrance and reach the mixing region of the T-junction element, where they flow along the +X direction. The fluids flow in parallel through the first element. The stream then reaches the vertical channel (segment 2) and moves in the –Z direction. At the end of the vertical channel, the stream reaches the first Y segment (principal module) and is split into two flows (segment 3). One stream moves in the +X direction and the other moves in the –X direction. Both flows then cross the Y segment of the principal module, at the end of which they are recombined and move in the –Y direction. Subsequently, the reunited stream reaches the vertical channel and moves in the +Z direction. At the end of the vertical channel, it arrives at the Y segment and is again split into two streams. One stream moves in the +Y direction and the other in the –Y direction, and both then pass through the Y segment. At the end of the Y segment, they are once again recombined and move in the +X direction. This process continues to the end of the mixer microchannel.

2.2 Chain Micromixer

A novel generation of 3D passive micromixer concept was first introduced by Viktorov and Nimafar (23). This type of micromixer, called the 'Chain micromixer', is based on the SAR process, meaning that the two fluids to be mixed are split and recombined to optimize the diffusion process. The main working principle for this type of microchannel is to make 90° rotation of a flow, folding the stream and then split and recombine the flow to enhance the efficiency of the microchannel. This process is repeated during the microchannel until achieving the desired degree of mixing. Figure 2.3 shows some important dimension of Chain mixers. As shown, the mixer is made up of four identical elements 1 ÷ 4 repeated in series.

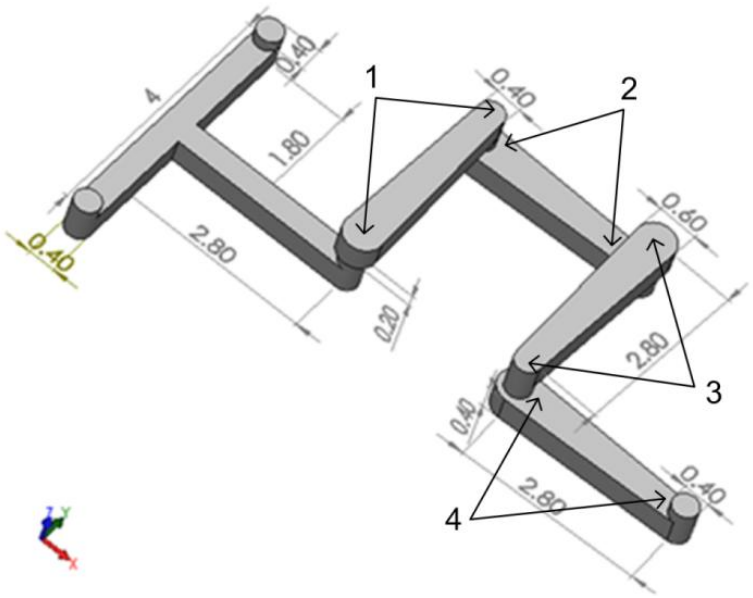

Figure 2.3 Design of the Chain micromixer (all dimensions are in mm)

As shown in Figure 2.3, after each vertical part (y direction), the diameter of the new section is 0.6 mm and extended 0.2 mm rather than the outlet of vertical part (0.4 mm). This characteristic of the geometry causes the splitting of the flow in the inlet of new part as depicted in Figure 2.4, segments 3, 5, 7 and 9, and in the central part of the segment the recombination effect takes place. At the outlet of the segment, the diameter is again 0.4 mm like the vertical part (Figure 2.4 a, segments 3, 5, 7 and 9. Indeed, after extension in the inlet, the flow getting constricted while go across these parts and the maximum constriction occurs at the outlet of this section. The maximum width of the microchannel is 0.6 mm and reduces during this part to minimum value of 0.4 mm.

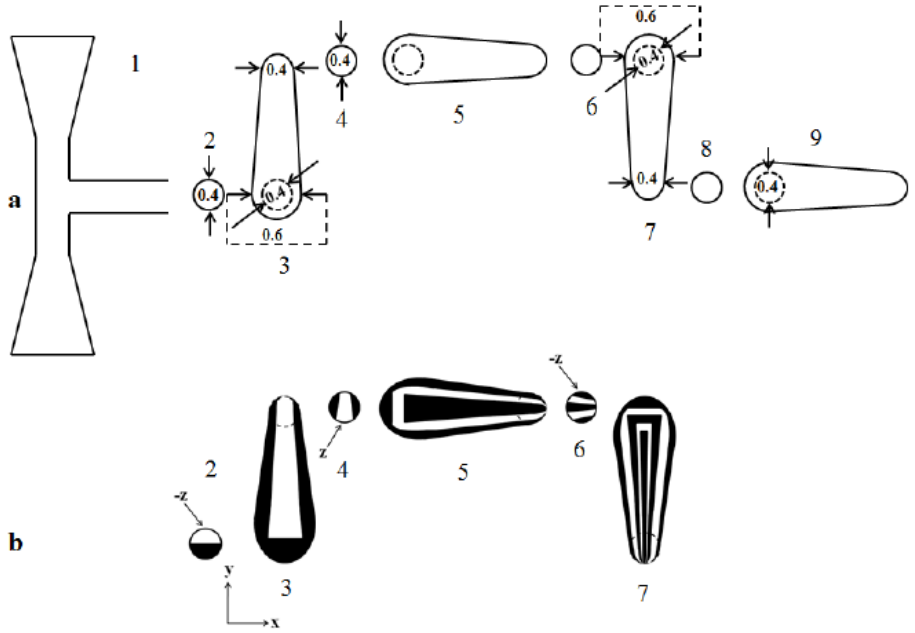

Figure 2.4 structural design of Chain micromixer; (a) of Chain microchannel segments; (b) Sequential lamination of layers

As Chain micromixer depicted in Figure 2.4 b, two mixing flows meet along the entrance microchannel and move along the entrance part until to reach the vertical part. In the vertical part the flow moves in –Z direction. At the end of the vertical channel the stream reaches the first chain element. The black color flow is then moved against a wall and the white color flow is moved to central part of the chain segment 3. In this way the flow is first splitted and then recombined into three layers flow, white and two black flows, as depicted in Figure 2.4 b section 4. After reaching to the vertical part, where these layers rotate 90^{o}, in the next mixer segment 5, five layers are created as illustrated in Figure 2.4 b part 6. By the same procedure, after segment 7 nine flow layers are formed. This process continues to the end of the Chain-micromixer. In fact, splitting and recombination causes large number of different layers and with increasing the layers, thickness of the layers will be smaller and the thickness of the poor mixed zone will be shorter and part of this zone moves to other mixed zone and this process proceed. This property enhances the mixing and also results in homogeneity. Therefore with splitting and recombination, mixing can be improved significantly.

2.3 H Micromixer

This type of passive micromixer is based on the SAR process. In this case, the H-shape makes it possible to move part of the flow near the wall, in the central zone of the channel along the axial direction and vice versa. Design and a photograph of the prototype are shown in Figure 2.5 (86).

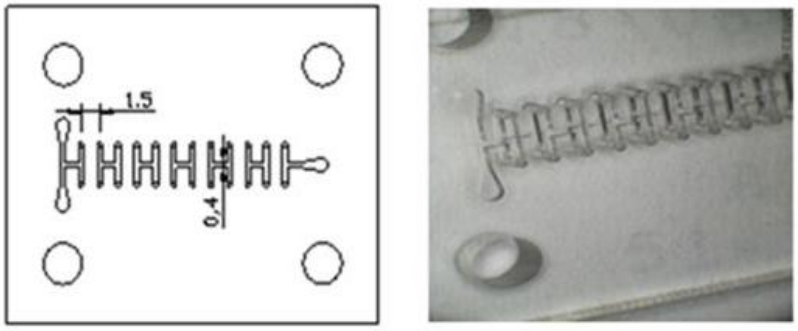

Figure 2.5 H micromixer

As illustrated in Figure 2.6, the H-micromixer geometry consists of two parts: the straight channel and the H-segment.

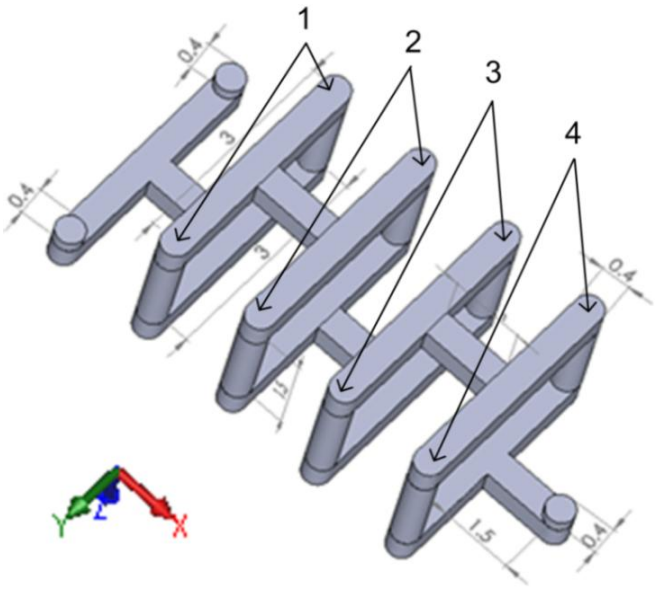

Figure 2.6 Design of the H micromixer

Figure 2.7 shows the 3D path and describes the SAR process: first, two species move in the +X direction, after which the flow reaches the H segment and is split into two flows: one moving in the +Y direction and the other moving in the –Y direction. Both flows then move to –Z. Afterwards, one moves in the +Y direction and the other moves in the –Y direction until the two flows are connected. The reunited flow then moves in the +X direction and the SAR process starts again.

This 3D path increases the micromixer efficiency. In particular, Figure 2.7 shows that when the flow is split and recombined, the part of the flow near the wall is moved into the central zone of the channel.

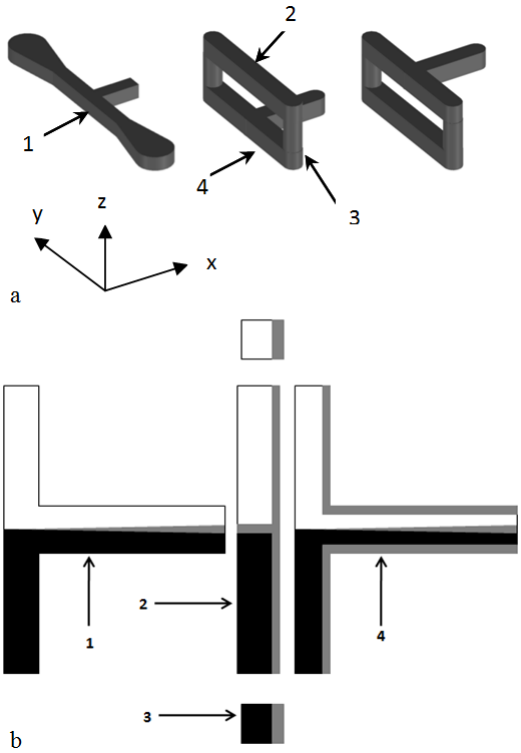

Figure 2.7 Detail of H-micromixer structure: (a) H-microchannel segments, (b) Sequential lamination of layers

As depicted in segment 1 of Figure 2.7 b, when the two mixing flows (shown in black and white) meet along the entrance microchannel, only the central zone is mixed (shown in grey). The mixed zone is then moved against a wall and the flow is split into two new flows (one is shown in white and grey and the other is black and grey). The mixed zone (grey) is now near the wall. When these two flows are recombined again, a new central zone (unmixed) is generated. As occurs in segment 1, the new central zone is then mixed at the end of segment 4. The stream is thus split into five layers (Figure 2.7 b, part 4) and this process continues to the end of the H-micromixer. As the SAR process is more effective than molecular diffusion, mixing can be improved significantly. After each splitting and recombining, the number of layers increases. In this regime (assuming no slip condition, Newtonian fluids and laminar flow), the speed of the flow near the wall is zero and the velocity profile in a channel is approximately parabolic. The shear stress is proportional to the derivative of the velocity profile, and absolute shear stress ($\tau = \mu \frac{du}{dy}$) is maximum at the wall and zero in the central zone, as shown in Figure 2.8.

Because of the SAR process described above, which occurs in every H-segment, the fluid in the central zone with maximum speed (no shear stress) moves to the wall (maximum shear stress) and the speed of this layer drops from maximum to minimum. Conversely, the fluid in the wall moves in the central part of the channel. By this means each fluid element of the mixed fluids moves in the mixer channels with a periodically changing velocity and shear stress. In such a situation, the mean velocities of the fluid elements in the mixer are roughly equal. These effects also contribute to increase the mixing efficiency.

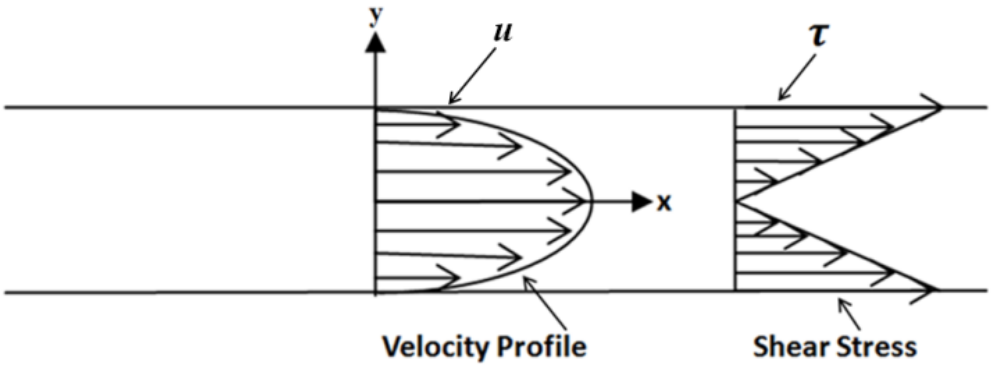

Figure 2.8 Velocity profile and shear stress in laminar flow

In some cases, the mixed fluid contains particles. It is known that the shear stress gradient turns the particles, which helps increasing mixing efficiency. In the proposed mixer the periodical shifting of the fluid element position assures that fluid elements move through the mixer with a sufficient shear stress gradient.

2.4 H-C Micromixer

A new micromixer, denoted as the H-C mixer and based on the SAR principle, was designed. It is basically a modified version of the Chain mixer (23) and the H mixer (86). The main working principle of Chain segment is to make 90° rotation of a flow, folding the stream and then split and recombine the flow to enhance the mixing. On the other hand, H-shape segment makes it possible to move part of the flow, which is initially at the central zone of the channel, and vice versa. Thus, both Chain and H modules contribute to improve the mixing efficiency.

Figure 2.9 shows the new design with an H-shaped module added at the end of each element to make the fluid flow closer to an ideal plug-flow. This module, in fact, is able to move the fluid

particles placed at the center of the upstream Chain module towards the wall of the downstream rectangular channel. Therefore, the fluid particles that according to the laminar parabolic velocity profile initially have the highest velocity are then slowed down and vice versa. This mechanism is expected to improve the performance of the mixer at the mid-range of Reynolds numbers, where there is a shorter residence time for the fluid particles to diffuse and secondary flows are not still intense enough to enhance mixing.

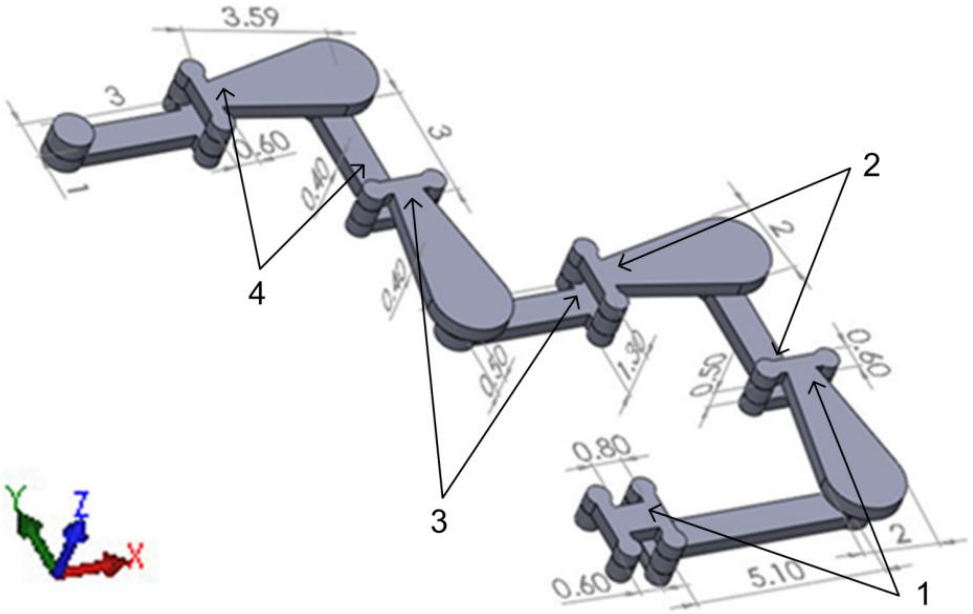

Figure 2.9 Design of the H-C micromixer (all dimensions are in mm)

For a better understanding, Figure 2.10 offers a simplified representation of the SAR mechanism inside the H-C mixer. The two fluids (black and white) meet at the rectangular channel of segment 2, fluids flow side by side along segment 4 and enter the first Chain module through a vertical cylindrical channel (segment 5, +Z flow direction). In segment 6, a three-layer flow is formed: the black fluid flows against the walls while the white fluid flows in the central part of the channel. At the end of the Chain module, the white fluid impinges on the upper wall of the splitting channel and then flows along it. Thus, a two-layer flow enters the H-shape module through the circular connecting channels of segment 7. At the exit of the H-shape module the black and white fluids flow as layers stratified along the Z-direction in segment 8 (see cross-section A-A). Finally, the flow enters the second Chain module through the vertical cylindrical channel 9 and the process is repeated. The splitting, recombination and rotation processes cause the formation of a large number of different vertical and horizontal layers, which highly increases the contact area between fluids; therefore, mixing is improved significantly.

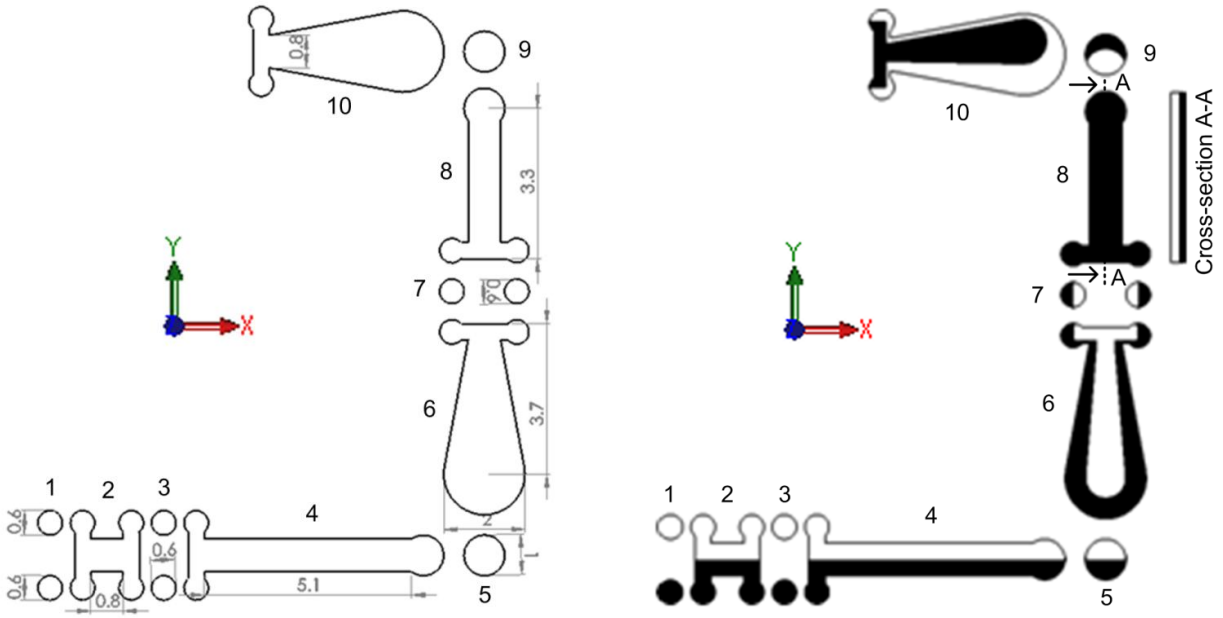

(a) (b)

Figure 2.10 Design of the H-C micromixer (a) 2D view (all dimensions are in mm), (b) Sequential lamination of layers

2.5 Y-Y Micromixer

Another novel micromixer, denoted as the "Y-Y", based on the SAR principle was designed. As shown in Figure 2.11, the Y-Y mixer is made up of four identical elements repeated in series. Each element is made up of two Y channels laying over parallel planes connected by vertical ducts. Two individual species enter via inlets (cylindrical ducts, Φ= 0.4 mm) and flow through its elements; the sequence has the aim to produce repeated folding and layering of the fluids, to reduce diffusion distance and thereby mixing time.

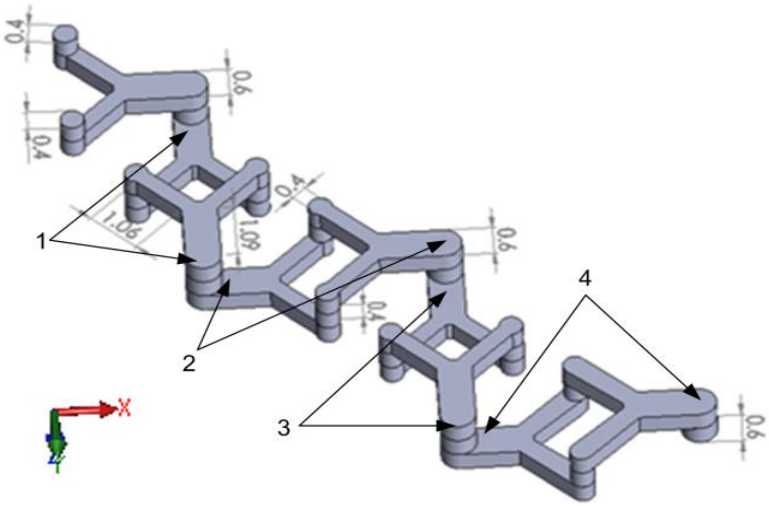

Figure 2.11 Design of the Y-Y micromixer (all dimensions are in mm)

The simple 2D structure of the Y-Y mixer is shown in Figure 2.12 (a). The split and recombine of process of fluids is represented in Figure 2.12 (b). The white and black fluids inter into the mixer through two inputs (segment 1) and fluids flow through side by side along +X direction (segment 2) until fluids reaches the cylindrical connector (segment 3). Afterword, the fluids make 90° change of direction (+Z direction) and inter into first Y module (segment 4) where the fluids changes their position; the white fluid goes to the bottom plane and black fluid goes to the top plane of the channel (see cross-section B-B).These vertical layers increases the fluids contact/surface area which eventually contribute to maximize mixing. In the end of second Y module (segment 6), three horizontal layers of fluids are created. Similarly, in the third Y module (segment 8), three vertical layers are created where white fluid is sandwiched between black fluids (cross-section C-C). After the second element of Y-Y mixer (segment 10), five vertical layers of fluids can be found and the process goes on. The splitting, recombination and rotation processes create a large number of different vertical and horizontal layers, which highly increases the contact area between fluids which improve mixing significantly.

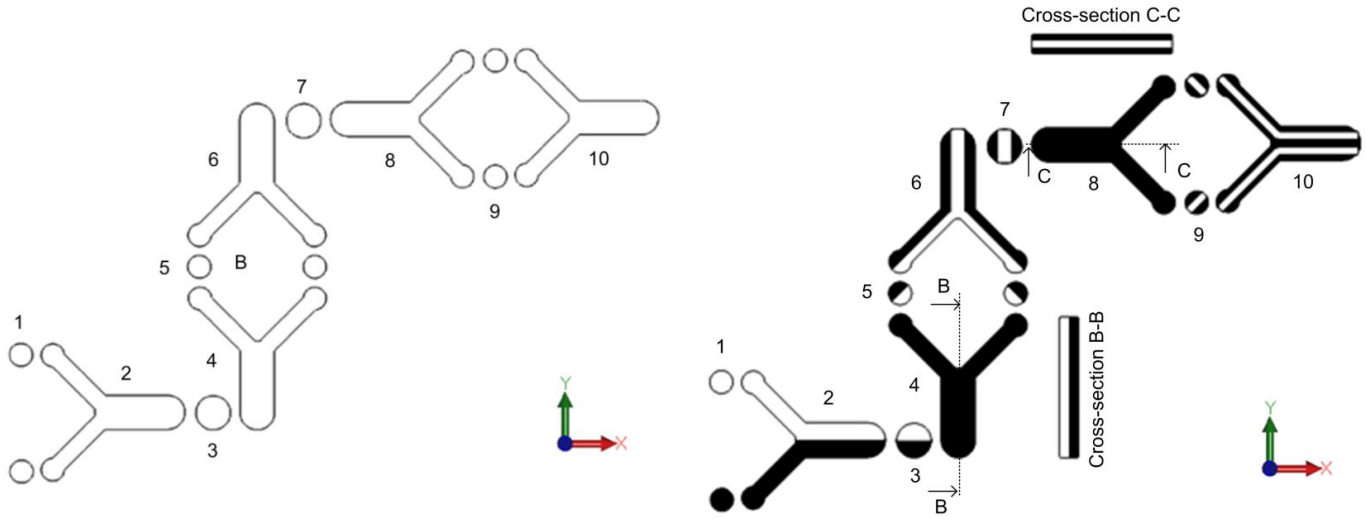

(a) (b)

Figure 2.12 Design of the Y-Y micromixer (a) 2D view, (b) Sequential lamination of layers

2.6 Fabrication of Micromixers

All micromixer geometries were micro-milled in polycarbonate by a computer numerical control (CNC) Milling and Engraving Machine P20S, KUHLMANN (Germany) at I.T.D sas di Borgna Daniela e Borgna Eugenio &C. (Turin, Italy). The prototypes were made up by overlapping and then clamping a central lamina and two covers, one of them provided by two entrances and one exit port as shown in Figure 2.13. The dimensions of prototypes were verified by a profilometer and a maximum error of 2% was found. In case of the Chain and Tear-drop mixers, the connecting ducts and edges of the channel were not in perfect shape (wear and tear in the structure). On the Y-Y mixer, the axis of the ducts connecting parallel millings were found to be not well perpendicular to the millings themselves; in this case, only a visual inspection was possible and no quantitative measurements were carried out.

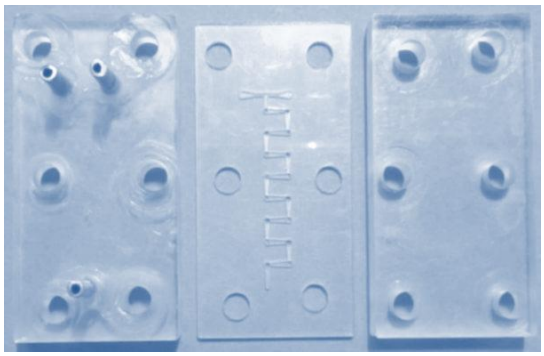

(a) Chain micromixer

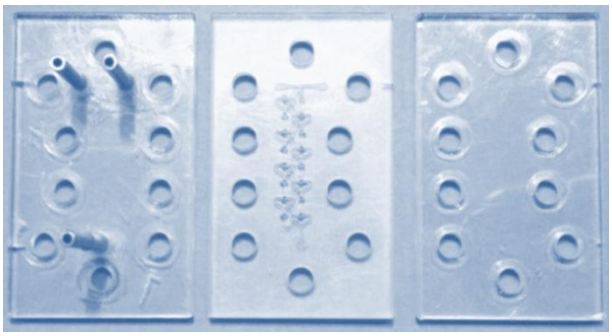

(b) Tear-drop micromixer

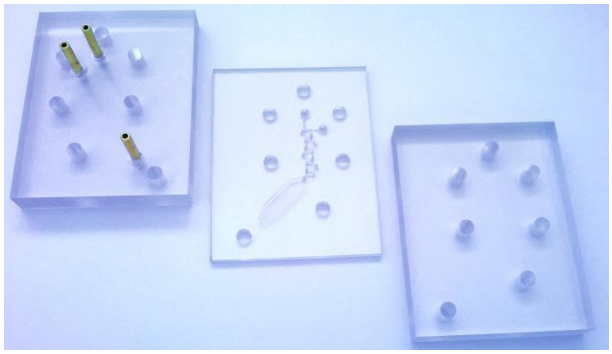

(c) Y-Y micromixer

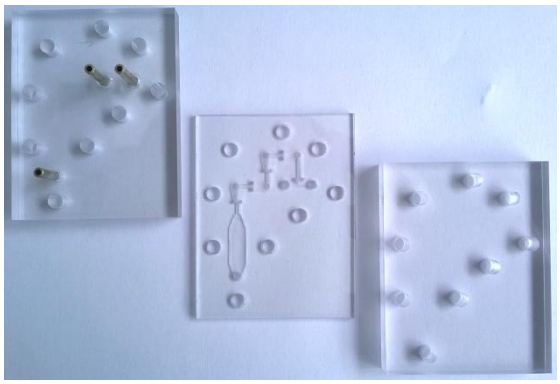

(d) H-C micromixer

Figure 2.13 Prototypes of the micromixers

Chapter 3. Experimental Technique: Micromixer

This chapter details the experimentation techniques used in computing mixing performance and pressure-drop. The procedures can be easily performed in any research laboratory. Flow experiments were carried out using a standard syringe pump and top-view imaging technique was obtained. The extent of mixing was quantified from these images by simple and straightforward methods.

3.1 Analyzing Technique of Mixing Efficiency

Imaging techniques and optical microscopy is the key tool for characterization micromixers. Optical microscopy offers a fine measurement at the micro scale that is useful for analyzing the micromixers. As mentioned before, together with digital cameras and digital image processing, a number of measurements in microchannels can be carried out with optical microscopy. Optical microscopy works with the part of the electromagnetic spectrum which is visible to human eyes. A typical human eye responds to wavelengths in air from 400 to 700 nm (22). The corresponding wavelengths in other media are reduced by a factor of refractive index. A human eye has maximum sensitivity about 555 nm, which is the green region.

The understanding of physical phenomena, such as flow behavior and mass transfer of the microfluidic devices is needed in order to develop these microsystems for industrial applications (87). Different researchers apply various techniques in micro-scale. Huchet et al. (88) used electrodiffusion technique to measure local value of wall shear rate. While Chen et al. (89) proposed the fluorescent resonant-energy transfer (FRET) to analyze the performance of the micro-reactors.

As alluded before it is a complicated task to achieve a high level of mixing inside a microchannel because of the flow characterized by low Reynolds number (*Re*) (90) (91) (92).

Mixing in microfluidic systems starts almost from regular periodical concentration profiles with steep gradient, which is governed by molecular diffusion proceeding in deformed fluid elements (93) and grows during the microchannel length. In order to quantitatively evaluate the degree of

mixing some techniques reported by researchers (94). For determination of the degree of mixing at different position in the SAR mixer, a photometric technique was used by Hardt et al. (35). Zolgharni et al. (95) explained that a Chen and Shie (96) reported that in the design of any micromixer, one of the most important performance parameters is a measure of mixing intensity. They quantified the mixing intensity by calculating the mass concentration distribution and described that the uniformity of mixing at sampled section is assessed by determining the mixing index (MI). Cook et al. (97) employed induced fluorescence to obtain quantitative data in terms of concentration distribution within the scaled micromixer channels.

Aoki et al. (98) evaluated mixing performance of the microchannels using parallel-competitive redox and neutralization reactions called the Villermaux / Dushman reaction. The reactions occur by mixing two reactant fluids. One is a solution of diluted strong acid (referred as solution 1), and the other is a buffer solution (mixture of weak acid and strong base) containing KI and KIO3 (redox reagents). Then, they used the UV light absorbance at 352 nm as a measure of mixing performance. They sampled mixed solutions and measured the absorbance of the solutions with a UV-Vis spectrometer.

Suh et al. (99) expressed that the easiest method for judging the mixing efficiency in micromixer structures is by flow visualization, which is done using dilution-type experiments and also notified that to quantitatively represent the composition uniformity, the coefficient of variation, CoV, which is the ratio of the standard deviation of each cross section, to the mean of each cross section has used. Also they quantitatively characterized the mixing efficiency of electro-kinetic micromixer by defining the mixing index (MI).

Fang and Yang (50) studied based on a concept encompassing splitting and recombination (SAR) and chaotic advection in a novel micro-reactor with 3D rotating flow. They used a methods to assess the mixing performance of a micro device involve blending of dye liquors (food dye and fluorescent dye) and the reaction of chemical indicators to approach to the reaction length. They reported that a reaction length assessed based on an analysis of the gray scale intensity of image captured via image processing. They calculated the average intensity of all pixels from a sampling image. The sampling image was determined on trimming the captured images and the average intensity of the sampled images extracted in sequence from upstream to downstream be normalized to get the normalized intensity which expresses the efficiency.

Also Lee et al. (8) studied on rotation effect in split and recombination micromixing and in order to quantify the degree of mixing in micromixers, a standard deviation of the distribution of intensity values (I) for the image data was calculated, when black is 0 and white is 255. These values were obtained by the image process using 8 bit depth lens.

Jeong et al. (100) reported that the mixing performance could be evaluated by two different methods. The first method was to focus on the upper part to measure how fast the fluorescent dye, which was initially located at the lower region of the microchannel, disseminated to the upper region. The other was to focus on the lower part to evaluate how fast the fluorescent dye located in the lower region disappeared. They found that the second method more suitable for mixing strategy and therefore adopted it to estimate the mixing performance.

Hardt et al. (101) studied based on passive micromixers for applications in the micro-reactor and expressed that a typical scenario encountered in μTAS is the mixing of liquid samples at small Reynolds (*Re*) numbers (*Re* <10). Also they reported that analyzing the data using both CFD methods and photometric techniques, allowing quantifying the progress of mixing.

Sheu et al. (102) surveyed the mixing of a split and recombine micromixer with tapered curved microchannels. For evaluating the degree of mixing, they used the standard deviation of the concentration on a cross-section normal to the flow direction and introduced the normalize standard deviation is the average value of the concentration over the sampled section and then reported that the uniformity of mixing at sampled sections is assessed by determining the mixing index of the solute concentration.

As mentioned above, because measurement of intensity distribution is important for quantitative characterization of micromixers, the quality of the illuminating system is important for the microscope setup. The illuminating system of a research grade microscope should fulfill three basic criteria of:

- Allowing maximum resolution and maximum contrast
- Being simple and easy to adjustment
- Having uniform illumination.

The most illumination source of modern microscopes is a laser. The laser light produces an output beams that is both coherent and collimated, which is ideal for illumination purposes.

3.2 Digital Image Processing

An image captured with an optical instrument is continuously varying array of shades and color tones. Images captures on films for instance are referred to as continuous –tone because the shade and hues blend together without disruption. Continuous-tone images are captured with analog optical and electronic devices. Optical signals are converted to analog electrical signals or to continuous change of the chemical properties. In the world of digital system, this continuous –tone images need to be converted to digital format and continuous –tones of an analog image are divided into individual intensity value. Similar to the analog-to-digital converting process in electronics, the conversion to a digital image requires two steps: sampling and quantization (22). With the pixel array, sampling and quantization occur in a CCD or CMOS image sensor automatically. Each pixel contains specific information about intensity and can be described by a specific digital data value in a precise location. Each image pixel is represented by the intensity value and a coordinate-pair with specific *x* and *y* values arranged in a Cartesian coordinate system. In many situations, the *x* location is referred to as the pixel number, and the *y* location is known as the line number. In the literature the aspect ratio of a digital image defined as the ratio between the width and the height of the image M/N. For instance the recommended NTSC (National Television System Committee) commercial broadcast standard aspect ratio for television and video equipment is while for digital high-definition television (HDTV) is M/N = 4/3. The image resolution determines the quality of a digital image and referred to as special resolution and gray scale resolution. The special resolution is determined by the number of pixels $M \times N$. Within a given physical dimensions, a digital image with a higher number of pixels will have a higher special resolution.

3.2.1 Gray Scale Image

In photography a gray scale digital image is an image in which the value of each pixel is a single sample that carries only intensity information. Image of this sort, also known as black- and-white, are composed exclusively of shade of gray, varying from black at the weakest and white at the strongest (22).

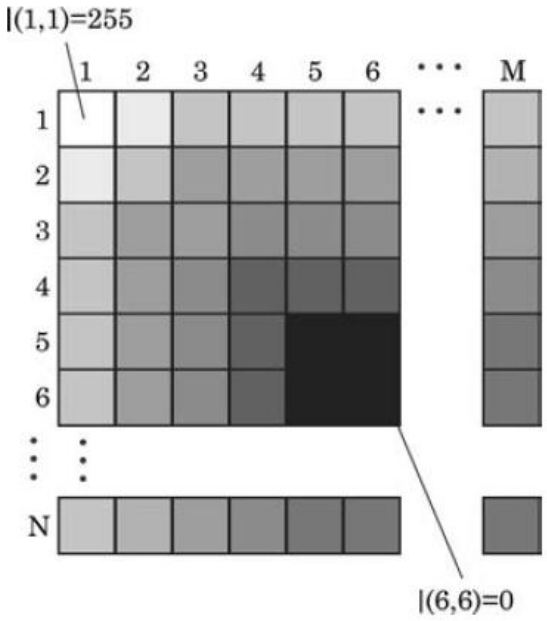

Figure 3.1 Schematic representation of the intensity array of an M×N digital image (22)

Gray scale images are distinct from one-bit bi-tonal black-and-white images, which in the context of computer imaging are images with only the two colors black and white also called binary images or monochromatic, denoting the presence of only mono color (chrome). Gray scale images are often the result of measuring the intensity of light at each pixel in a single band of the electromagnetic spectrum and can be synthesizes from a full color image. The intensity of a pixel is expressed within a given range between a minimum and maximum (that is applied in the program Matlab code for calibration of the program). This range is represented in an abstract was as a range from 0 (black) and 1 (white), with any fractional in between. Another convention is to employ percentage, so the scale is then from 0% to 100%. This range is used for a more intuitive approach. In computing, although the gray scale can be computed through rational numbers, image pixels are stored in binary, quantized form. Some early gray scale monitors can only show up to 16 (2^4, with a camera with bit depth of 4) shades, but today gray scale images intended for visual display are commonly stored with 8 bit per sampled pixel, which allows 256 (2^8) different intensities. A bit depth of n can generate different gray scales. Recently, most common CCD and CMOS sensors provide bit depth of 8, 10 or 12 that can describe 256,1024 and 4096 different gray levels respectively. If the image depicted in Figure 3.1 has a bit depth of 8, the value of the white pixel (1, 1) is 255, while the value of the black pixel (6, 6) is 0. The human eye can better discriminate between different shades of color than between varying shades of gray.

Therefore, gray scale images are often rendered in pseudo color by assigning specific gray level ranges to particular color values. This technique is useful for highlighting regions of interest, especially concentration fields in micromixers (22).

A digital image can be stored in a single file. Intensity values are stored in a single vector. Also the horizontal and vertical dimension of an image is stored in a header of the image. Reading the files with known dimension can restore the two-dimensional matrix for further processing. The size of a digital image file depends on the pixel dimension format and bit depth of the image. Uncompressed file format, such as tagged image file format (TIFF) results in the largest file sizes. In this thesis TIFF format are used for analyzing the captured images to import to the Matlab program.

3.3 Quantification Methods of Micromixing

3.3.1 Indirect Method

Indirect methods measure the extent of mixing based on the products of chemical reactions or change in fluorescent dye to a change of PH level in the mixed fluids.

To evaluate the degree of mixing parallel competing reaction can be used. For example, when a mixture of iodate, iodine, sodium hydroxide and boric acid is mixed with sulfuric acid, the so-called Dushman reaction occurs:

$$\begin{gathered} H^2BO_3^- + H^+ \leftrightarrow H_3BO_3 \\ 5I^- + IO_3^- + 6H^+ \leftrightarrow 3I_2 + 3H_2O \\ I^- + I_2 \leftrightarrow I_3^- \end{gathered} \qquad \textbf{3.1}$$

As eluded in the introduction, the first reaction is a neutralization, which is very fast compared to the second reaction. If mixing is well-done, there is no acid left for the second reaction to form iodine. In fact, the amount of iodine produce depends on the efficiency of mixing process. The concentration of I_3^- in the mixing products indicates the degree of mixing. The concentration of I_3^- in the mixing measured via the absorbance at 353 nm. Using this method, the mixing efficiency can be determined as:

$$\eta_{mixing} = \frac{ABS}{ABS_\infty} \qquad \textbf{3.2}$$

Where ABS is the result of the absorbance measurement and ABS_∞ is the absorbance of the fully mixed solution.

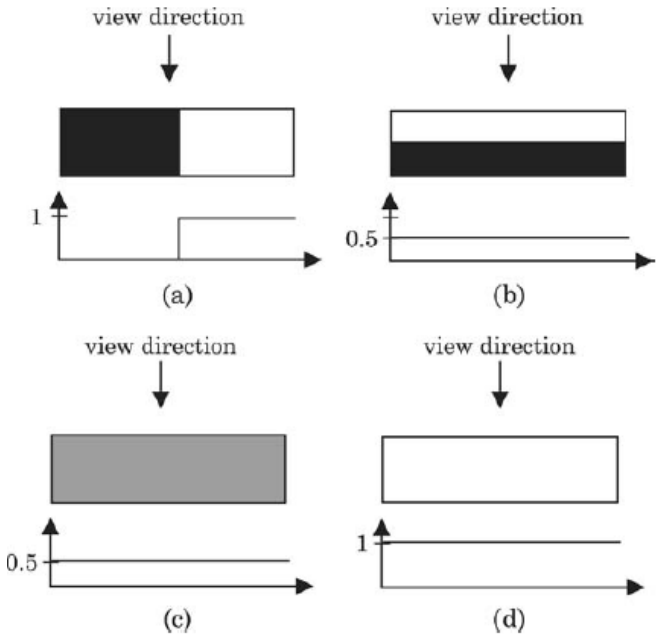

Figure 3.2 Mixing evaluation using fluorescent dye: (a) before mixing, view direction parallel to fluid interface; (b) before mixing, view direction perpendicular to fluid interface; (c) results of mixing, using conventional fluorescent technique; (d) results of mixing, using fluorescent technique based on PH sensitivity (22)

The disadvantage of this technique is that the absorbance measurement would normally need to be carried out off the chip and also integration of fiber optics for on-chip measurement would be expensive. Characterization of the microchannel is still challenging due to the two dimensional nature of fluorescent measurement with a camera – microscope system. The use of mixing index and PDF is based on statistical evaluation of the fluorescent dye and these methods are useful for analyzing the image during the microchannel, as depicted in Figure 3.2. For considering the concentration distribution along the microchannel, measurement would only be possible with the more expensive laser scanning confocal system. Munson and Yager (48) suggested a fluorescent detection techniques based on the PH sensitivity. Two species are mixed with an equal concentration (10 μm) of fluorescein. They only differ in the PH levels. Then they used an equation 3.3 to evaluate the mixing efficiency.

$$\eta = \frac{I - I_0}{I_\infty - I_0} \qquad \textbf{3.3}$$

Where I_0 the average intensity measured across the both fluids at the inlet, I_∞ the fully mixed solution and is the averaged intensity of the region of interest.

3.3.2 Direct Statistical Method

As far as we know, there are several quantification methods for analyzing the micromixers. In this thesis, direct statistical method is used to analyze the micromixers. Because good mixing is understood as the homogeneity of the mixed fluids, the distribution of the concentration (or distribution of the intensity) values of an image can be used for evaluating the degree of mixing.

In this method, the region of interest is selected by a mouse as a rectangle in the displayed image as shown in Figure 3.10. Subsequently, concentration values of region of interest are calculated and finally mixing efficiency is calculated using equations 3.4 and 3.5 (6) (17) (103).

$$\sigma = \sqrt{\frac{1}{N}\sum_{i=1}^{N}(C_i - C_m)^2} \quad \textbf{3.4}$$

$$\eta = 1 - \sqrt{\frac{\sigma^2}{{\sigma_{max}}^2}} \quad \textbf{3.5}$$

where σ is the standard deviation of mass fraction of blue liquid dye, N is the number of pixels at the target area, C_i is the mass fraction of blue dye at a pixel i, and C_m is the mean mass fraction of a blue dye at the target area; η is the mixing efficiency, and σ_{max} is the maximum standard deviation of the blue dye, which is 0.5 for identical flow rates at the inlets of the micromixer (103) (104). When the two species are fully mixed, mixing efficiency η is 1 (100%); efficiency between 80% and 100% is generally acceptable for mixing process applications (22).

3.4 Experimental Equipment

The experimental equipment used for this investigation is:

1. Injection Syringe
2. Syringe Pump
3. Microscope
4. Digital pressure gauge

3.4.1 Injection Syringe

Injection glass syringes (20.0 ml) from Tomopal Inc. (Sacramento, USA) were used for the experiments and shown in Figure 3.3.

Figure 3.3 Glass Syringe (20.0 ml)

3.4.2 Syringe Pump

The syringe pump used in this study is a KDS 210 series as shown in Figure 3.4.

Figure 3.4 Syringe pump KDS 210

Features for KDS 210 series are:

- Holds two syringe
- Backlit LCD display
- Knob locks / unlocks drive block for effortless, drag-free adjustment
- Simple menu-driven setup:
- select syringe size from display table
- dispense flow rates
- Continuous dispense volume display

- Preset volume control and automatic shut-off
- Setting can be reviewed or changed during operation
- Choice of unit selection

The flow rate range for this instrument is from 0.1 µl/hr (10µl syringe) to 506 ml/hr (60 ml syringe) with errors less than 1%.

3.4.3 Microscope

The microscope used during the mixing process is a Veho model VMS-004D-400x USB microscope (Figure 3.5), with 400X magnification, 2 Megapixel lens (interpolated) and measurement software.

Figure 3.5 Microscope Veho

The VMS-004D-400x USB microscope provides many uses from laboratory research and comes with integrated snapshot and recording functions. Some characteristics such as fine slider adjustment for brightness and hue are too important for analyzing the experimental data.

- Features for Veho VMS-004D-400x are:
- Adjustable LEDs for object illumination
- 2Mp CMOS sensor (interpolated)
- Measurement function using enclosed software
- Snapshot and video recording function
- With a base zoom level 20x, the VMS-004 can also magnify 400x

- Fine slider adjustment for brightness, hue, saturation and sharpness, plus a black and white display mode
- The lens can be adjusted to point in any direction using the moveable arm
- Simply install the drivers, plug the microscope into the computer via USB

3.4.4 Digital Pressure Gauge

Pressure-drop between the inputs and the output of the microchannel was measured using a Digibar digital pressure gauge (Hottinger Baldwin Messtechnik, Darmstadt, Germany) as shown in Figure 3.6.

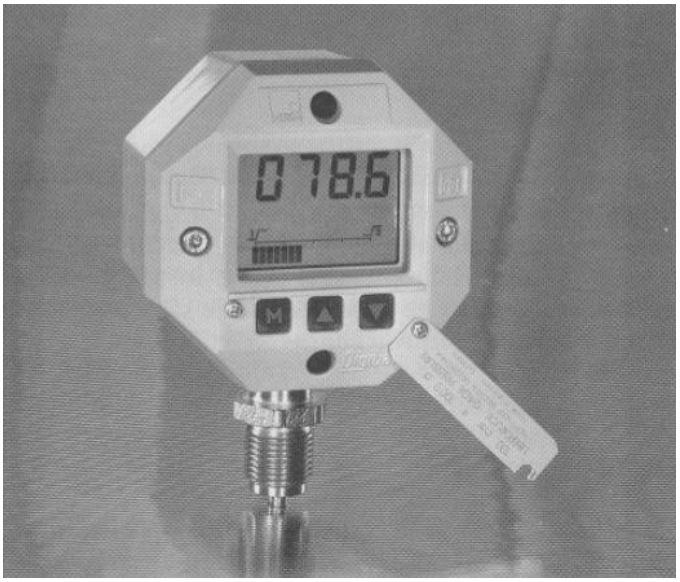

Figure 3.6 Digital pressure gauge

Special features Digibar pressure gauge:

- Operated as a manometer with battery operation and
- Operated as a pressure transmitter with 4-20 mA current output, freely adjustable
- Clear multi-function display, exact and fast pressure readings on the spot
- Limit-relay board, (option) (changeover contacts, fail-safe)
- Operating voltage failure proof storage of settings in EEPROM
- Up to 500 mbar with a sensitivity of 0.5 mbar

3.5 Experimental Setup

The experimental setup used for this investigation is shown in Figure 3.7. A syringe pump and two glass syringes were used to individually supply distilled water and a commercial blue liquid dye (Rebecchi F.Lli Valtrebbia, Rivergaro, Italy) through the inlets of the micromixer at the same flow rate. A high speed image acquainting microscope was used to capture images of the prototype.

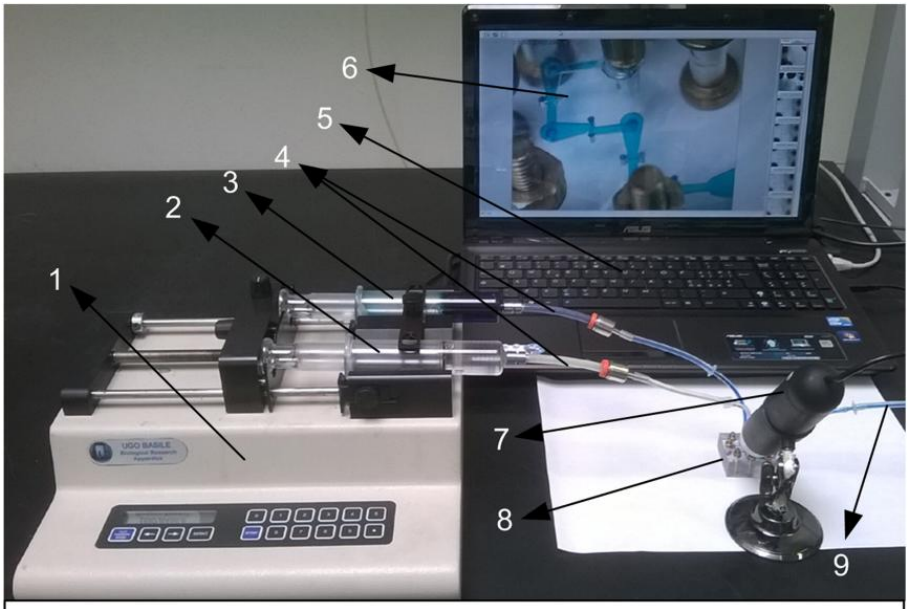

1 Syringe pump;	2 Syringe one;	3 Syringe two;
4 Connection tubes;	5 Notebook;	6 Image of H-C mixer;
7 Microscope;	8 H-C mixer;	9 Output

Figure 3.7 Experimental setup

3.6 Experimental Procedure

Equipment were always cleaned and dried before experiment; all tests were performed at room temperature (25° C). The syringe pump was always started at least one minute before each test to ensure a steady flow.

At first, a calibration was carried out at four target areas, denoted as C, D, E, and F in

Figure 3.8 near to the exit of each element of the H-C mixer; in this way problems related to dissimilarities in lighting could be overcome. Using a syringe the micromixer was filled with a mixture of blue liquid dye and water at known concentrations from 0 up to 100%.

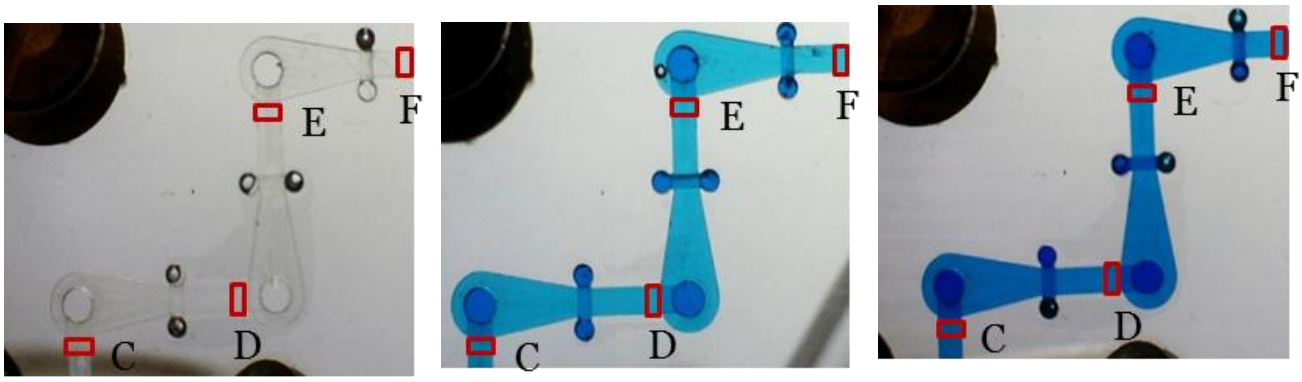

0% blue liquid dye 50% blue liquid dye 100% blue liquid dye

Figure 3.8 H-C micromixers after filling with mixture of water and blue liquid dye

Images of the bottom side of the prototype were captured by the microscope. The related color images were then converted into grey-scale images and post-processed by a custom made Matlab code; in particular, an average value of the grey intensity distribution inside each image of the target area was picked up. In this way it was possible to associate mixture concentration values to grey intensities of image; a linear relationship was found out in case of H-C mixer as shown in Figure 3.9.

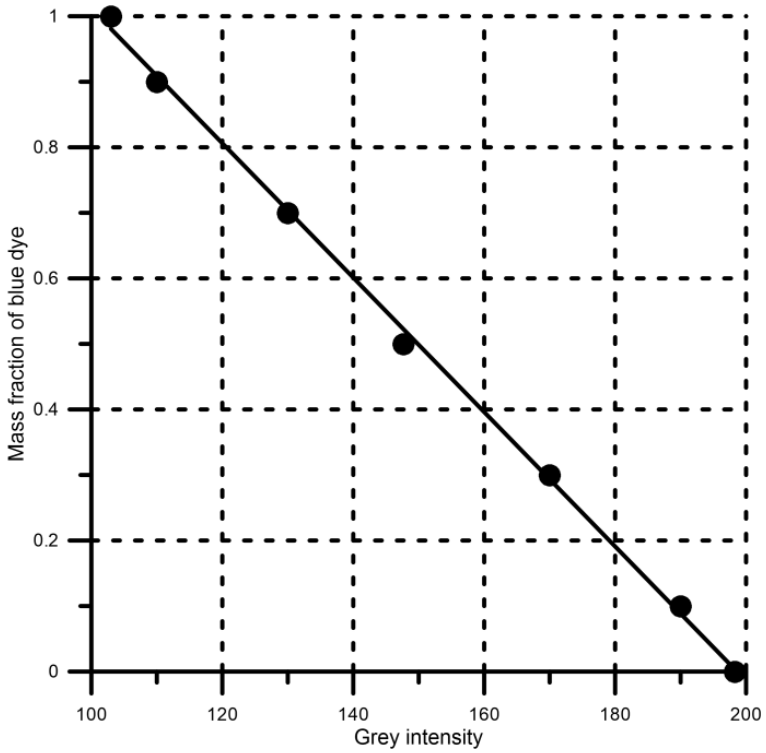

Figure 3.9 Relationship between the mass fraction of blue dye and the grey intensity of the corresponding image at the fourth element of the H-C mixer

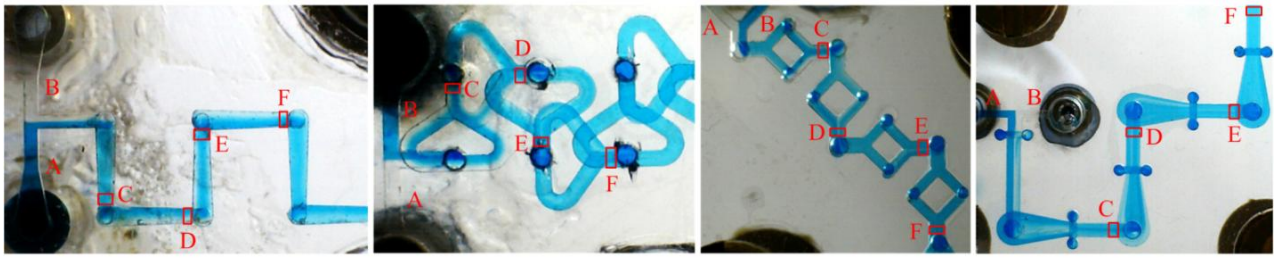

Figure 3.10 Micromixers after filling with fluids at Re = 1

Subsequently, the programmable syringe pump was used to supply water and blue liquid dye into two inlet ports of the micromixer at the same flow-rate, as an example in Figure 3.10. The values of flow rate corresponding to the desired Reynolds numbers were set digitally. It must be noted that calibration and experiment were carried out under the same operating conditions, such as prototype position and lighting. For each flow-rate value, i.e. for each Reynolds number, an image of the bottom side of the prototype including the fluid path from the entrance area to the end of the microchannel was captured; all tests were carried out at Reynolds numbers ranging from 1 to 100.

Table 3.1 Reynolds (Re) number, velocity and flow rate values during experimental investigation

Re	V (m/s)	V (mm/s)	Chain	Tear-drop	Y-Y	H-C
			Q_v (m^3/s)	Q_v (m^3/s)	Q_v (m^3/s)	Q_v (m^3/s)
1	0.0025	2.5	4.00E-10	4.00E-10	6.00E-10	8.00E-10
10	0.025	25	4.00E-09	4.00E-09	6.00E-09	8.00E-09
20	0.05	50	8.00E-09	8.00E-09	1.20E-08	1.60E-08
30	0.075	75	1.20E-08	1.20E-08	1.80E-08	2.40E-08
40	0.1	100	1.60E-08	1.60E-08	2.40E-08	3.20E-08
50	0.125	125	2.00E-08	2.00E-08	3.00E-08	4.00E-08
60	0.15	150	2.40E-08	2.40E-08	3.60E-08	4.80E-08
70	0.175	175	2.80E-08	2.80E-08	4.20E-08	5.60E-08
80	0.2	200	3.20E-08	3.20E-08	4.80E-08	6.40E-08
90	0.225	225	3.60E-08	3.60E-08	5.40E-08	7.20E-08
100	0.25	250	4.00E-08	4.00E-08	6.00E-08	8.00E-08

Then colored images were converted into grey-scale and post-processed by another custom made Matlab code. From each main image four cropped images of the fluid at the four target areas were taken. The grey level distribution associated at each pixel of the image was then converted into a concentration distribution by means of the calibration curve previously obtained. Finally, the standard deviation of mass fraction of blue dye at each target area was worked out as an index of

homogeneity of the mixture. Tests were carried out following the same procedure on all the mixers to evaluate mixture quality at each element. The velocity, flow rate and Reynolds (Re) numbers for different mixers are presented in Table 3.1.

Pressure drop between the inputs and the output of the microchannel was measured using a digital pressure gauge (Digibar). The measuring range of the pressure gauge is from0 to 500 mbar with a sensitivity of 0.5 mbar.

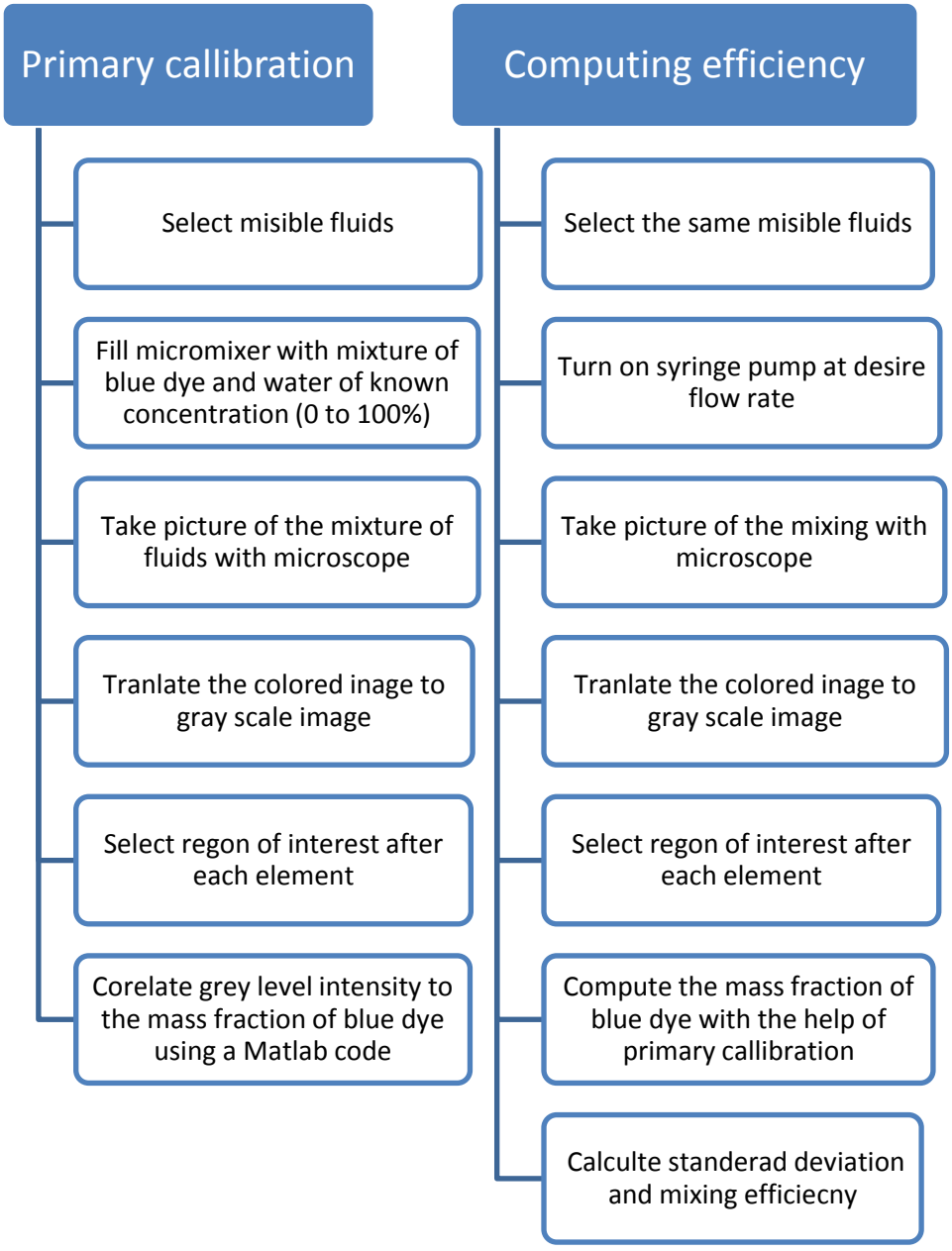

Figure 3.11 Flow chart for the experimental analysis

Chapter 4. Numerical Simulation

Fluid motion is governed by the Navier-Stokes equations (99), a set of coupled and nonlinear partial differential equations derived from the basic laws of conservation of mass, momentum and energy. In the micromixer analysis, the unknowns are usually the velocity and the pressure (pressure drop) alongside the microchannel (98) and some tracers like temperature. The analytical solution of these equations is practically impossible. The simplifications can take the form of geometrical simplification (the flow in rectangle or circle), and physical simplification (homogeneous density, linearity, etc...). Occasionally, it is possible to develop by using asymptotic analyses technique, and there has been considerable success in the past years, like the development of boundary layer theory. Scientist had to resort to laboratory experiments when theoretical analysis was impossible. Physical complexity can be resorted to the system. The answers delivered are usually qualitatively different since dynamic and geometric similitude is difficult to enforce simultaneously between the lab experiment and the prototype. A good example is the Reynolds number similarity (97) which if violated can turn a turbulent flow laminar. Furthermore, the design and construction of these experiments can be difficult and costly.

Computational fluid dynamics (CFD) is an additional tool in the arsenal of the scientists. In its early days CFD was often controversial, as it involved additional approximation to the governing equations and raised additional issues (96). Nowadays CFD is an established discipline alongside theoretical and experimental methods (17) (94) (101) (93) (91). This position is in large part due to the exponential growth of computer power which has allowed us to tackle ever large and more complex problems. In order to evaluate each type of micromixer, the flow and diffusion between two solutions were numerically analyzed by CFD in some research articles (8) (35) (50) (87). The result is a wealth of predictions for flow velocity, temperature, pressure, density, and chemical concentration for any region where flow occurs. CFD calculation is used in this research for detecting the required pressure drop in the micromixers.

Hence, in this work ANSYS Fluent 15 was used to analyze the flow and pressure-drop, mixing efficiency and residence time distribution (RTD) in the microchannel of different mixers.

4.1 Numerical Model of Mixing

4.1.1 Mathematical Model

To analyze flow structure and mixing behavior of the fluids in the micromixers, the commercial fluid dynamics (CFD) code ANSYS Fluent 15 was used. This code solve the mass and momentum (Navier-Stokes) conservation equations by using a finite volume approximation and is capable of modeling the fluid mixture, whose components have distinct sets of physical properties (17).

The mathematical model for the above design is based on a number of assumptions and approximations: i) the flow in the microchannel is laminar; ii) the fluids are incompressible and Newtonian; iii) there is no gravitational effect, and no chemical reaction between the species is considered; iv) the temperature variation due to Joule heating is negligible.

The motion of the fluid flow is governed by continuity equation, Navier-Stokes equation, and species convection-diffusion equation (105) (106) (107):

$$\begin{aligned} \nabla . V &= 0 \\ \rho V . \nabla V &= -\nabla P + \mu \nabla^2 \mathrm{V} \\ V . \nabla C &= D \nabla^2 \mathrm{C} \end{aligned} \qquad \textbf{4.1}$$

where V is the fluid velocity vector, ρ is the fluid density, P is the pressure, μ is the fluid dynamic viscosity, C is the species mass concentration, and D is the diffusion coefficient of the species.

4.1.2 Boundary Condition

The numerical simulation is not free from numerical diffusion error comes from the discretization of the convection terms in the Navier-Stokes equations. However the error can be minimized by adopting a higher-order numerical scheme for the convection terms (108). A high resolution scheme, i.e., second-order-accurate upwind scheme, was used to discretize the advection terms in the governing equations. Pressure-based and steady laminar flow with the species transport model on was used for simulation. The SIMPLEC scheme was assigned as solution method to calculate pressure velocity coupling to ensure convergence of the computations (93) (109). The fluid concentration at the two inlets was set to 1 and 0, respectively. In the boundary conditions, inlets were set to velocity inlets, static gauge pressure of the outlet was set to 0 Pa, and all walls were set to stationary walls with no-slip condition. The second order upwind scheme for momentum and

pressure was employed to obtain more accurate results. To ensure a satisfying convergence, the residuals are monitored and targeted residuals values are set to 10^{-6} for the continuity and momentum equations. The value of physical parameters used in this simulation work is presented in Table 4.1.

Table 4.1 Physical parameters

Parameter	Value	Unit
Velocity (V)	0.0025 to 0.25	m/s
Density (ρ)	1000	Kg/m^3
Viscosity (μ)	1×10^{-3}	Kg/m s
Diffusivity	1×10^{-9}	m^2/s

The computations were done in two stages. First, the continuity and momentum equations were solved numerically to obtain the velocity profile that was eventually inserted into the convection-diffusion equation. Then the solution of the latter provided the concentration distribution inside the whole domain to get the secondary (transverse) flow and mixing efficiency.

4.1.3 Mixing Efficiency

The following equations were employed to quantify the numerical mixing performance (110) (106) (111):

$$\sigma = \sqrt{\frac{1}{N}\sum_{i=1}^{N}(C_i - C_m)^2} \quad \textbf{4.2}$$

$$\eta = 1 - \sqrt{\frac{\sigma^2}{{\sigma_{max}}^2}} \quad \textbf{4.3}$$

where σ is the standard deviation of mass fraction of a species, N is the number of sample cells at a cross section, C_i is the mass fraction of blue liquid dye at a sample cell i, and C_m is the mean mass fraction of a species at a cross section; η is the mixing efficiency, and σ_{max} is the maximum standard deviation of a species. When $\eta = 0$, it represents no mixing and $\eta = 1$, it represents maximum (100%) mixing efficiency. The value of maximum standard deviation for different inlets flow-rate ratio is shown in Table 4.2.

Table 4.2 Simulation parameters

Inlet flow-rate ratio	1		2		3	
Fluid	Liquid A	Liquid B	Liquid A	Liquid B	Liquid A	Liquid B
Flow rate	q	q	2q/3	q/3	3q/4	q/4
Mass fraction	1	0	1	0	1	0
Maximum standard deviation	0.50		0.67		0.75	

4.1.4 Meshing

The studied geometries and meshes have been built with Fluent. Cut cell Cartesian method was used to generate hexahedral cells, which are suitable for complex geometries. A high quality mesh was necessary to avoid errors due to numerical diffusion. A mesh sensitivity test was implemented before running simulations used for the analysis. The mesh must be appropriately refined to ensure that the simulations results are independent of mesh size with optimal computational time and minimum mesh refinements were implemented as shown in Figure 4.1and Figure 4.2. Different meshing sizes for the hexahedral were investigated in order to find the most appropriate mesh refinement for simulation.

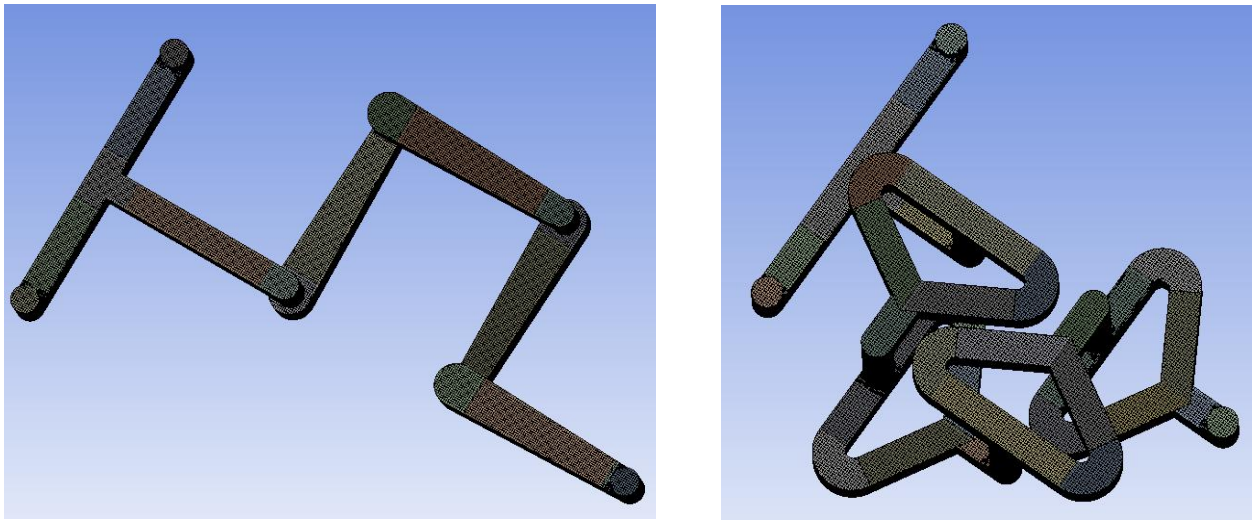

(a) Chain mixer (b) Tear-drop mixer

Figure 4.1 Hexahedral cells created in Chain and Tear-drop mixers

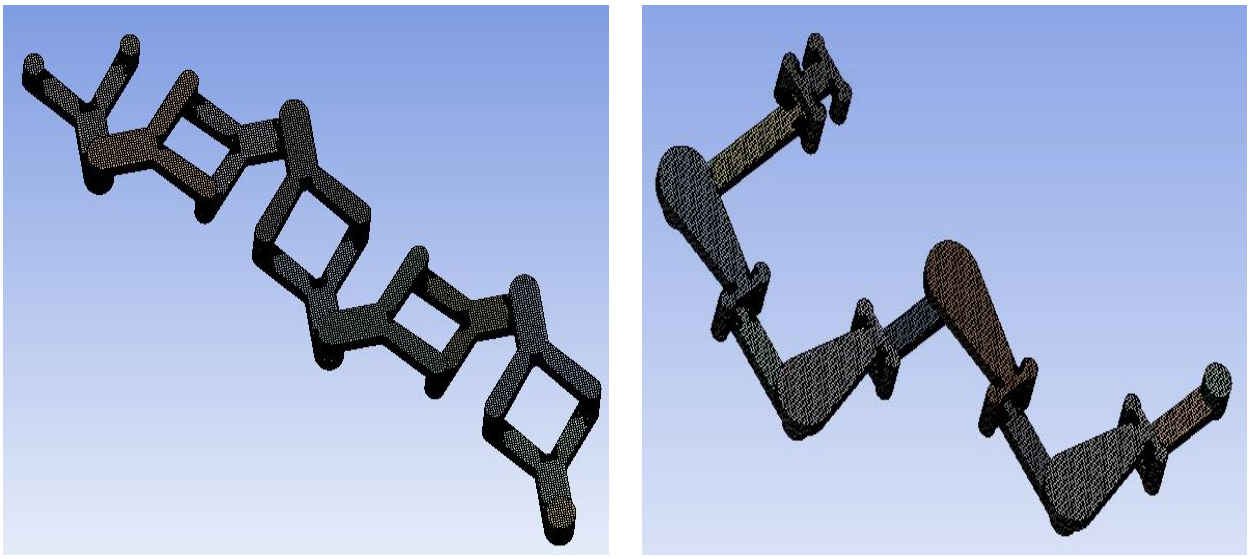

(a) Y-Y mixer (b) H-C mixer

Figure 4.2 Hexahedral cells created in Y-Y and H-C micromixers

The variance of species concentration was determined at the exit of all the micromixers. The variance is based on the intensity of segregation using mean concentration. The variance (standard deviation) of the mass fraction was computed using equation **4.2**. Different grid systems with numbers of elements ranging from 2.5×10^5 to 5.2×10^5 were used in this test and the corresponding values of standard deviation (σ) at different Re numbers are given in Table 4.3.

Table 4.3 Standard deviation of mass fraction at the output of four mixers

Name of mixer	Number of elements (Approximate)	Standard deviation (σ)			
		Re = 1	Re = 10	Re = 30	Re = 100
Chain	2.5×10^5	0.027225	0.0289	0.0289	0.027225
	3.2×10^5	0.015625	0.019321	0.026115	0.025027
	4.1×10^5	0.070225	0.018851	0.021199	0.023409
	5.2×10^5	0.001225	0.001406	0.0016	0.001806
Tear-drop	2.5×10^5	0.0092	0.0501	0.121	0.0163
	3.2×10^5	0.0096	0.05427	0.1344	0.0176
	4.1×10^5	0.01129	0.06695	0.1527	0.0267
	5.2×10^5	0.0123	0.0766	0.1609	0.0332
Y-Y	3.2×10^5	0.0016	0.00395	0.0335	0.0119
	4.1×10^5	0.0017	0.00468	0.0345	0.0131
	5.03×10^5	0.00175	0.00545	0.0347	0.0132
H-C	3.2×10^5	0.02231	0.0252	0.019	0.0223
	4.1×10^5	0.0224	0.02525	0.01961	0.0225
	5.1×10^5	0.0225	0.0253	0.01974	0.0236

For example, the deviation of standard deviation of the Chain mixer after four elements was less than 4% as shown in Figure 4.3. So a grid number of about 3.21×10^5 was chosen for the Chain mixer to minimize the computational time. Similarly, grids of around 4.1×10^5, 5.03×10^5 and 5.1×10^5 were used to perform simulations on the Tear-drop, the Y-Y and the H-C mixers, respectively.

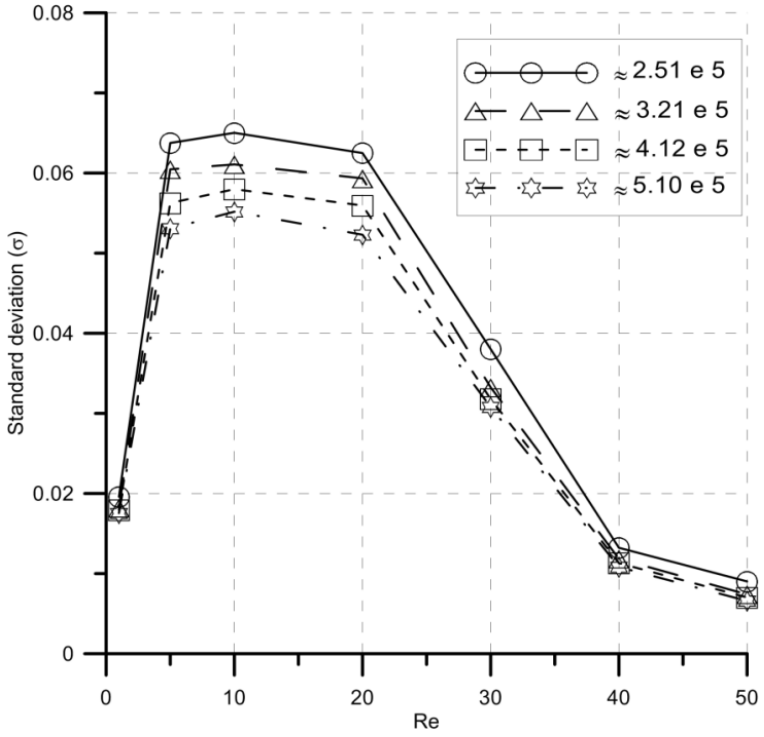

Figure 4.3 Grid dependency of the Chain mixer: standard deviation at the exit

4.2 Numerical Model of RTD

In ideal reactor systems (e.g. batch and plug flow reactors) an equal residence times of fluid elements is assumed, whereas the knowledge of the distribution of times that fluid elements spend in a real mixer or reactor, or simply their RTD, is needed for the characterization of flow and mixing in a non-ideal mixing or reaction system. And since the complete velocity distribution of the system is usually not available, RTD information is especially needed. The concept of RTD, although earlier proposed by MacMullin and Weber (112) was first extensively used by Danckwerts (113) to describe important distribution functions and to study the flow and mixing performance of flowing fluids in non-ideal tubes (empty and packed), mixers, and reactors.

The RTD is obtained commonly by injecting a tracer instantaneously (a pulse input) or at a constant rate (a step input) at the inlet of a flow system, and then measuring the tracer concentration at the outlet as a function of time. The RTD (or exit age-distribution) function, *E(t)*, which describes

quantitatively how much time different fluid elements have spent in a continuous flow system is defined mathematically such that *E(t)* dt is the fraction, at the outlet, of fluid elements that have spent a time of between *t* and *t+dt* in the flow system (114). In the determination of RTD in this study, the pulse input method is used in order to avoid the numerical errors from data differentiation that is inherent in the step input method. The time steps for each simulation are appropriately adjusted so as to limit the necessary number of calculation steps needed by the time-consuming transient simulations. For pulse tracer input method, *E(t)* is given by equation 4.4:

$$E(t) = \frac{C(t)}{\int_0^\infty C(t)dt} \approx \frac{C(t_i)}{\sum_{i=0}^{\infty} C(t_i)\Delta t_i} \quad \textbf{4.4}$$

where Δt_i is the physical time step used in the simulation. When the mixing performance of flow systems of different sizes or flow conditions is to be compared, a normalized RTD function, *E(θ)* is used instead of *E(t).* Both functions are related by equation 4.5 (115)

$$E(\theta) = t_m E(t) \quad \textbf{4.5}$$

where t_m is the mean residence time of the RTD defined by equation 4.6:

$$t_m(t) = \frac{\int_0^\infty tC(t)\,dt}{\int_0^\infty C(t)dt} \approx \frac{\sum_{i=0}^{\infty} t_i C(t_i)\Delta t_i}{\sum_{i=0}^{\infty} C(t_i)\Delta t_i} \quad \textbf{4.6}$$

and θ is the dimensionless time defined by equation 4.7:

$$\theta = \frac{t}{t_m(t)} \quad \textbf{4.7}$$

The CFD simulations the plots of *E(θ)* vs. θ are constructed for all the cases studied. Another important parameter is coefficient of variance (CoV), defined by equation 4.8:

$$CoV = \frac{\sigma'(t)}{t_m(t)} \quad \textbf{4.8}$$

where σ' is the standard deviation, defined by equation 4.9:

$$\sigma'(t)^2 = \left(\sum_{i=o}^{\infty} (t_i - t_m)^2 E(t_i)\,\Delta t_i\right) \quad \textbf{4.9}$$

And the skewness, *S*:

$$s = \frac{\int_0^\infty (t_i - t_m)^2 E\,(t) dt}{\sigma(t)^{3/2}} \qquad \textbf{4.10}$$

Once the RTD function is obtained, certain parameters, which are used to quantify the degree or extent of mixing in continuous flow systems, can then be calculated. These statistical parameters are mathematically given by equations 4.6 to 4.10. They are: the mean residence time (t_m) or the first moment of RTD, which gives the average time the exiting fluid elements spend in the flow system; variance or the second moment ($\sigma'(t)^2$) of RTD, which is a measure of the spread of the distribution; and coefficient of variation (CoV), which is a measure of the relative standard deviation of the distribution.

The RTD of a microchannel mixer will deviate from an ideal plug flow mixer depending on the hydrodynamics within the microchannel. In the context of the static microchannel mixers designed to effect radial/transverse mixing, a CoV of zero would imply complete plug-flow mixing while a non-zero CoV implies that there is axial dispersion or mixing caused by non-uniform or laminar velocity profile and molecular diffusion. In this case, the smaller the variance or the CoV, the narrower is the RTD, the closer is the distribution to the mean residence time, and the better the mixing quality (114).

4.2.1 RTD Analysis Setup

A commercial CFD code, namely ANSYS Fluent 15, is employed to simulate the flow and to obtain results concerning the mixing efficiency inside the micromixers. Initially, each simulation runs in steady state conditions until convergence is achieved. Then the seed particles are set to be injected for specific time and the simulation rerun under unsteady (transient) conditions. Particle tracking with the Langrangian tracking model was employed.

Chapter 5. Results and Discussion: Micromixer

This section presents the numerical and experimental results obtained in microfluidic laboratory at same and different inlet flow-rate ratios varying Reynolds numbers in all mentioned micromixers. Firstly, the primary qualitative mixing behavior (without diffusion) is presented in respect of path lines. Secondly, numerical and experimental mixing efficiency are evaluated using Direct Statistical Method. Thirdly the RTD is also computed along with pressure-drop. Finally a detailed comparison is made among the selected four micromixers.

5.1 Preliminary Analysis

Firstly, the flow patterns inside the four mixers were examined to know the overall distribution of fluid particles. These preliminary simulations were carried out without taking into account molecular diffusion. In fact, the analysis of path line distributions permits qualitative forecasting of mixing quality: the more tangled the path lines, the larger the interfacial area between the fluids to be mixed and better the mixing performance.

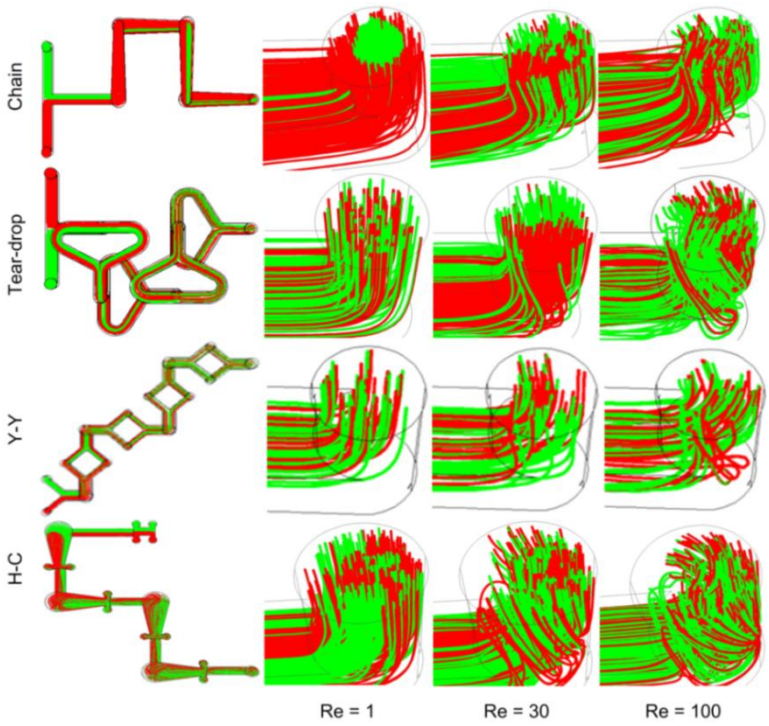

Figure 5.1 Path line at the outlet of micromixers at inlet flow-rate ratio of 1

Figure 5.1 shows the path line distributions both inside and at the exit of the micromixers, when two fluids (red and green) with identical flow rates enter the inputs. In the case of the Chain mixer at *Re* = 1 and *Re* = 30, clusters of path lines of the same fluid can be detected, which indicates the non-homogeneity of mixing; only at *Re* = 100, path lines of different fluids seem to be well tangled. On the other hand, the Tear-drop micromixer shows well tangled path lines except at the mid-range of Reynolds numbers. On the contrary, the H-C and the Y-Y mixers show well tangled path lines at all Reynolds numbers. Therefore, both H-C and Y-Y mixers are expected to have a better mixing ability than the other mixers. The path line distribution for inlet flow-rate ratios of 3 is shown in Figure 5.2; same scenario was found as like inlet flow-rate ratio of 1, with some minor differences.

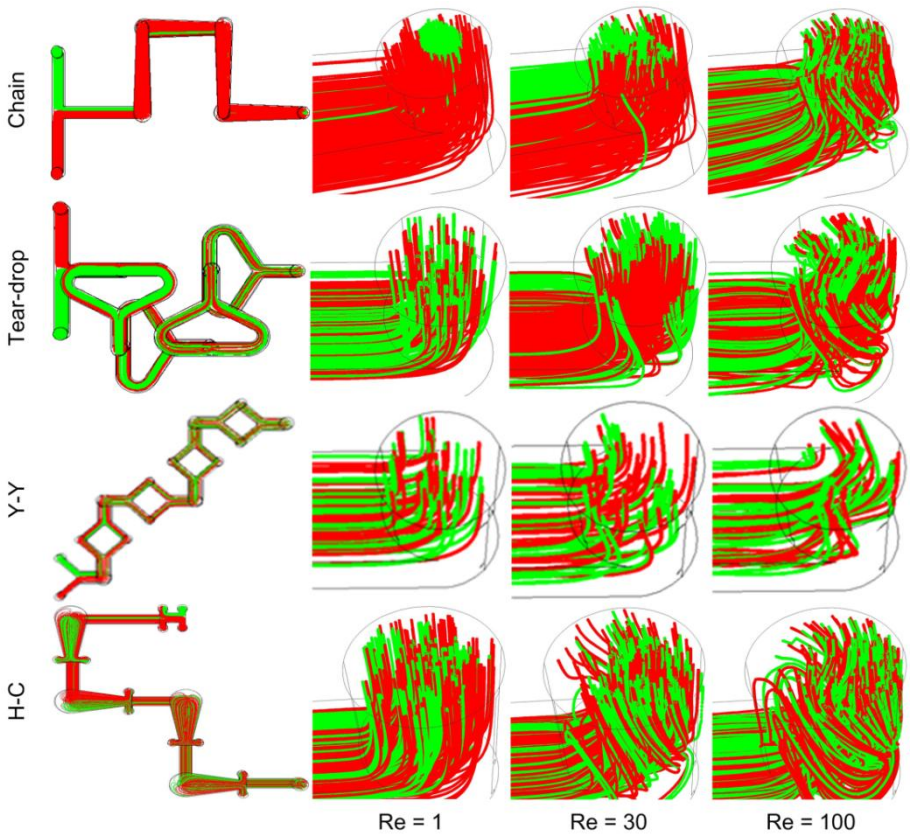

Figure 5.2 Path line at the outlet of mixers at inlet flow-rate ratios of 3

5.2 Mixing Efficiency

Secondly, mixing efficiency and pressure-drop of the Chain, the Tear-drop, the H-C and the Y-Y mixers was evaluated experimentally and numerically in a range of Reynolds numbers from 1 to 100. The mixing efficiency for inlet flow-rate ratios of 1 to 3 was also studied. The detail experimental and numerical results for each mixer are present below in separate section:

5.2.1 Chain Micromixer

The mixing efficiency of the Chain mixer was evaluated experimentally and numerically in a range of Reynolds numbers from 1 to 100. Figure 5.3 shows the concentration distribution of fluids along the length of the mixer in both experimental tests and numerical simulations. As seen, there is a reasonable agreement between the simulation and the experimental results. However, there are still differences in some sections. The main reason lies in the fact that simulation images show horizontal mid-plane. Therefore, it was not possible to take into consideration the multiple laminations of fluid layers. By contrast, the experimental images cover the whole depth of the channel view able from below.

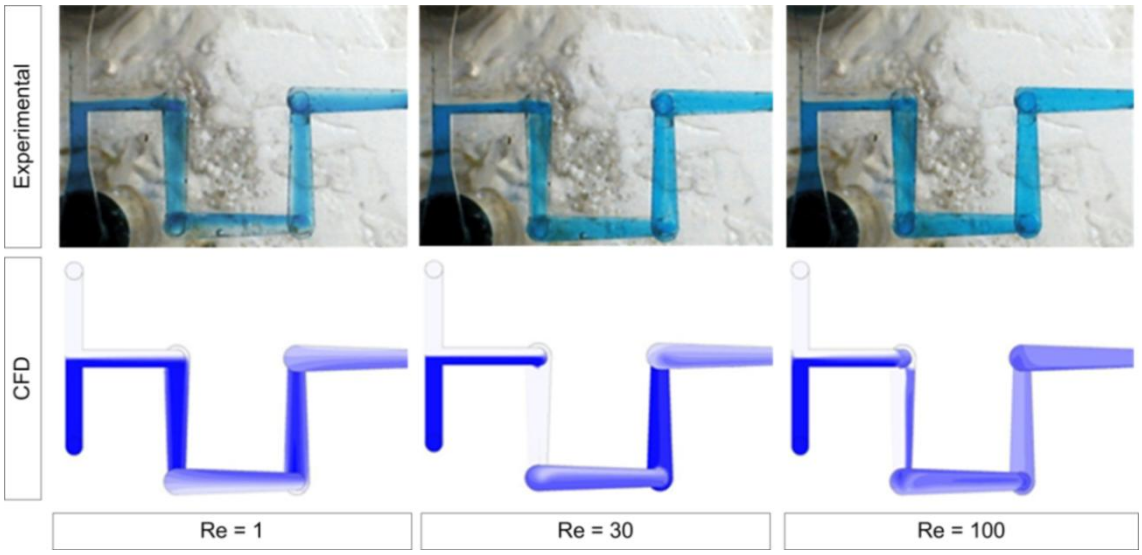

Figure 5.3 Comparison between the images taken from the computer simulation and the experiments of the Chain mixer

Table 5.1list standard deviation (σ), mixing efficiency (η) and pressure drop (ΔP) of the Chain mixer during experimental and numerical investigation.

Figure 5.4 compares the mixing efficiency of the Chain mixer at the exit of the fourth element; as shown, experimental and numerical mixing efficiency curves show reasonable agreement and the maximum relative error is less than 10%. Mixing efficiency is less than 80% at low and mid-range of Reynolds (1<Re<50) numbers and afterward, efficiency increase with the Re numbers and finally the efficiency becomes 90% at high Reynolds (Re>60) numbers.

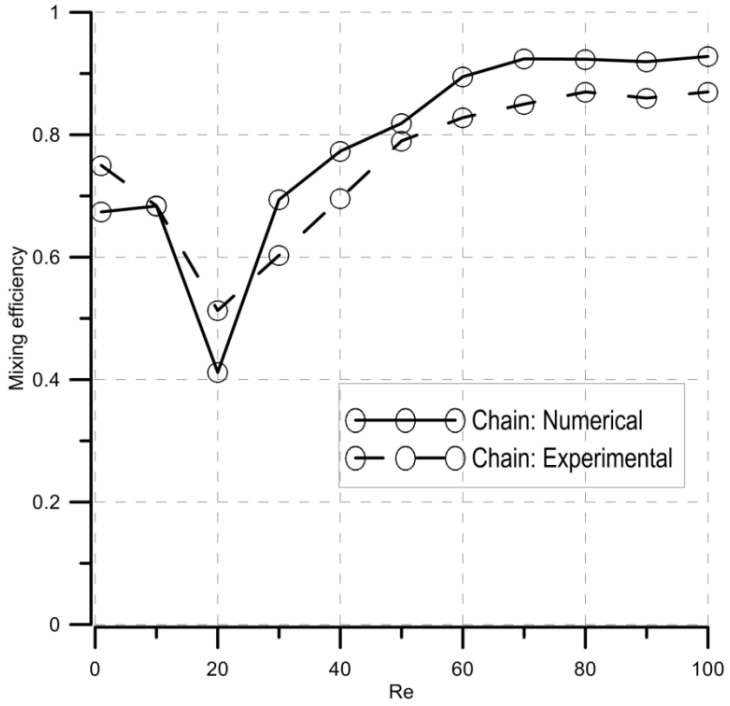

Figure 5.4 Experimental and numerical mixing efficiency of the Chain mixer at the exit of the fourth element

Table 5.1 Standard deviation (σ), mixing efficiency (η) and pressure-drop (Δ*P*) during experimental and numerical investigation of the Chain mixer (Flow-rate ratio of 1)

Re	Flow rate (Q) (m^3/s)	Experimental			Numerical		
		Standard deviation (σ)	Mixing efficiency (η)	Pressure drop (Δ*P*) (Pa)	Standard deviation (σ)	Mixing efficiency (η)	Pressure drop (Δ*P*) (Pa)
1	4.00E-10	0.1725	0.655	12.5	0.192	0.616	5.678
10	4.00E-09	0.2155	0.569	62.5	0.226	0.548	58.875
20	8.00E-09	0.2165	0.567	125	0.212	0.576	126.51
30	1.20E-08	0.1995	0.601	200	0.191	0.618	209.33
40	1.60E-08	0.12	0.76	300	0.1195	0.761	304.09
50	2.00E-08	0.085	0.83	400	0.0705	0.859	411.4
60	2.40E-08	0.075	0.85	525	0.047	0.906	550
70	2.80E-08	0.07	0.86	650	0.045	0.91	667.93
80	3.20E-08	0.06	0.88	800	0.0341	0.9318	814.94
90	3.60E-08	0.06	0.88	975	0.0325	0.935	1005
100	4.00E-08	0.06	0.88	1150	0.03	0.94	1200

Pressure-drop (Δ*P*) of the Chain micromixer was evaluated experimentally as well as numerically. As shown in Figure 5.5, numerical and experimental curves have the same trend, i.e. pressure-drop increases with the increase of flow rate. The maximum relative error is of about 10% and the maximum pressure drop is about 1200 Pa at *Re* = 100.

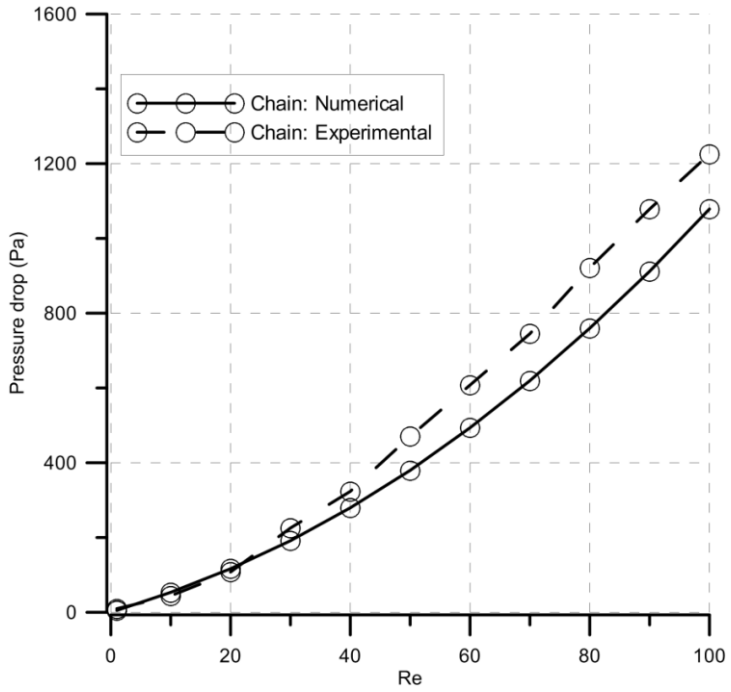

Figure 5.5 Experimental and numerical pressure-drop of the Chain micromixer, varying *Re* numbers

Finally, the mixing efficiency of the Chain mixer was evaluated for inlet flow-rate ratios of 1 to 3 and Table 5.2 shows the corresponding values of mixing efficiency.

Table 5.2 Standard deviation (σ) and mixing efficiency (η) during numerical investigation of the Chain mixer

Re	Flow rate (Q) (m^3/s)	Flow-rate ratio 1		Flow-rate ratio 2		Flow-rate ratio 3	
		Standard deviation (σ)	Mixing efficiency (η)	Standard deviation (σ)	Mixing efficiency (η)	Standard deviation (σ)	Mixing efficiency (η)
1	4.00E-10	0.192	0.616	0.16214	0.758	0.1515	0.798
10	4.00E-09	0.226	0.548	0.12328	0.816	0.10125	0.865
20	8.00E-09	0.212	0.576	0.24388	0.636	0.1935	0.742
30	1.20E-08	0.191	0.618	0.17286	0.742	0.164025	0.7813
40	1.60E-08	0.1195	0.761	0.05427	0.919	0.04425	0.941
50	2.00E-08	0.0705	0.859	0.06432	0.904	0.04275	0.943
60	2.40E-08	0.047	0.906	0.06566	0.902	0.045	0.94
70	2.80E-08	0.045	0.91	0.05427	0.919	0.033	0.956
80	3.20E-08	0.0341	0.9318	0.03618	0.946	0.02025	0.973
90	3.60E-08	0.0325	0.935	0.02211	0.967	0.01275	0.983
100	4.00E-08	0.03	0.94	0.01541	0.977	0.01005	0.9866

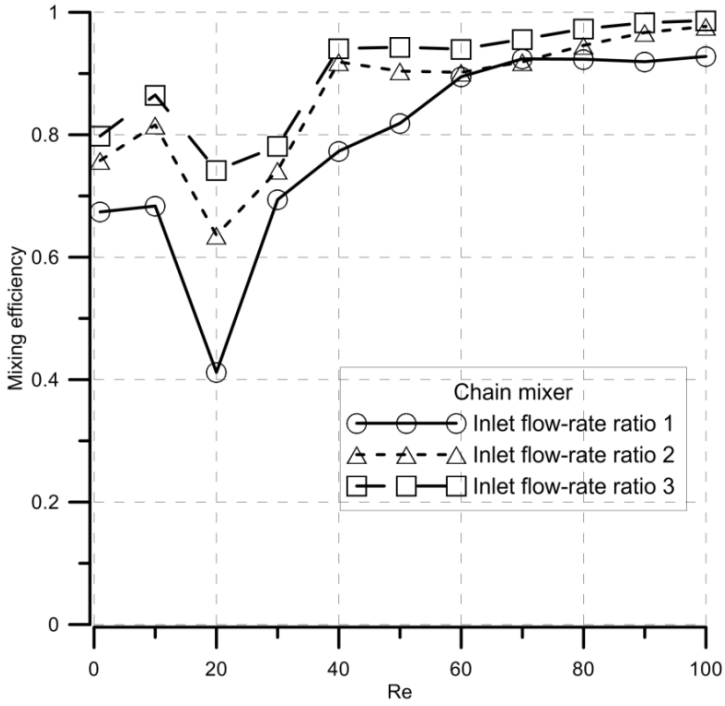

Figure 5.6 The numerical mixing efficiency of the Chain micromixer for different inlet flow-rate ratios and varying Reynolds numbers ($1 \leq Re \leq 100$)

Figure 5.6 compares the numerical results obtained for the Chain mixer varying the inlet flow-rate ratios from 1 to 3. In case of inlet flow-rate ratio of 1, the mixing efficiency is about 70% at low Reynolds numbers, relatively poor for mid-range Reynolds numbers and finally exceeds 80% at $Re \geq 50$. It is also clear that mixing efficiency depends strongly on the inlet flow-rate ratios up to $Re = 60$; in particular, efficiency increases significantly with the increase of inlet flow-rate ratios.

5.2.2 Tear-drop Micromixer

The mixing efficiency of the Tear-drop mixer was evaluated and Figure 5.7 gives the concentration distribution of fluids along the length of the mixer in both experimental tests and numerical simulations. Qualitatively, the images obtain in experimental analysis represents acceptable agreements with the numerical simulation but there are still differences in some sections. The experimental images cover the whole depth of the channel whereas, the simulation images show horizontal plane. Therefore, it was not possible to take into consideration the multiple laminations of fluids layers.

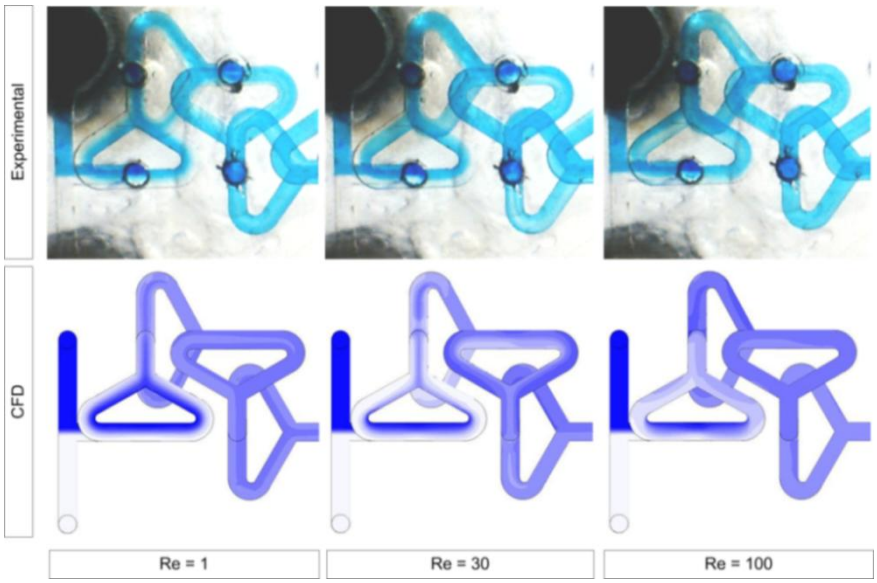

Figure 5.7 Comparison between the images taken from the computer simulation and the experiments of the Tear-drop mixer

Table 5.3 list standard deviation (σ), mixing efficiency (η) and pressure drop (ΔP) of the Tear-drop mixer during experimental and numerical investigation.

The mixing efficiency of the Tear-drop mixer at the exit of the fourth element is illustrated in Figure 5.8. Experimental and numerical mixing efficiency curves show reasonable agreement and the maximum relative error is less than 10%. Mixing efficiency is more than 80% at both low (Re<5) and high (Re>50) Reynolds numbers. But at mid-range of Reynolds (20<Re<50) numbers, the mixing efficiency is relatively low (η≈80%). A decrease of efficiency at the mid-range of Reynolds numbers can be explained considering that, increasing the flow velocity, there is a shorter residence time for the fluid particles to diffuse.

Table 5.3 Standard deviation (σ), mixing efficiency (η) and pressure-drop (Δ*P*) during experimental and numerical investigation of Tear-drop mixer (Flow-rate ratio of 1)

Re	Flow rate (Q) (m^3/s)	Experimental			Numerical		
		Standard deviation (σ)	Mixing efficiency (η)	Pressure drop (Δ*P*) (Pa)	Standard deviation (σ)	Mixing efficiency (η)	Pressure drop (Δ*P*) (Pa)
1	4.00E-10	0.048	0.904	37.5	0.00615	0.9877	7.69
10	4.00E-09	0.079	0.842	112	0.0525	0.895	78.525
20	8.00E-09	0.1	0.8	175	0.1162	0.7676	180.65
30	1.20E-08	0.14	0.72	250	0.1245	0.751	297.75
40	1.60E-08	0.1275	0.745	350	0.1105	0.779	429.25
50	2.00E-08	0.0805	0.839	487	0.0865	0.827	577
60	2.40E-08	0.07	0.86	587	0.058	0.884	738.25
70	2.80E-08	0.063	0.874	712	0.03385	0.9323	907.5
80	3.20E-08	0.053	0.894	862	0.02	0.96	1106
90	3.60E-08	0.0435	0.913	1000	0.0144	0.9712	1269
100	4.00E-08	0.0485	0.903	1150	0.0131	0.9738	1441

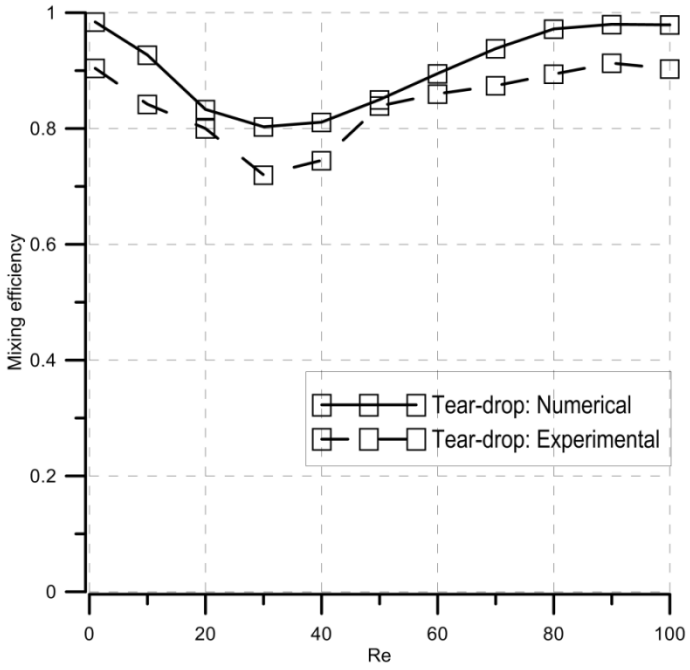

Figure 5.8 Experimental and numerical mixing efficiency of the Tear-drop mixer at the exit of the fourth element

Figure 5.9 shows the Pressure-drop (Δ*P*) of the Tear-drop micromixer; numerical and experimental curves have the same behavior, i.e. pressure drop increases with the increase of Reynolds numbers.

The maximum relative error is of about 17%, which can be explained by some defects of the prototype.

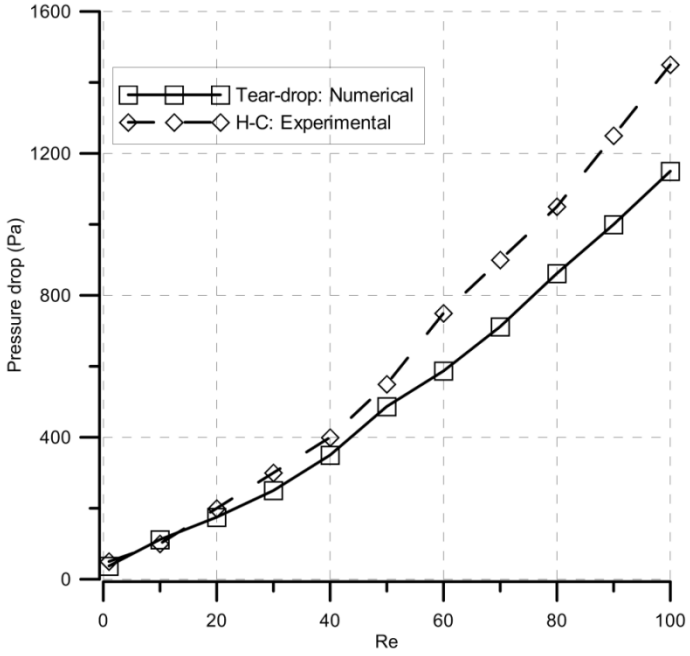

Figure 5.9 Experimental and numerical pressure drop of the Tear-drop micromixer, varying *Re* numbers

The mixing efficiency of the Tear-drop mixer was evaluated at Reynolds numbers from1 to 100 for inlet flow-rate ratios of 1 to 3 and Table 5.4 shows the corresponding values of mixing efficiency.

Table 5.4 Standard deviation (σ) and mixing efficiency (η) during numerical investigation of the Tear-drop mixer

Re	Flow rate (Q) (m^3/s)	Flow-rate ratio 1		Flow-rate ratio 2		Flow-rate ratio 3	
		Standard deviation (σ)	Mixing efficiency (η)	Standard deviation (σ)	Mixing efficiency (η)	Standard deviation (σ)	Mixing efficiency (η)
1	4.00E-10	0.00615	0.9877	0.012931	0.9807	0.006	0.992
10	4.00E-09	0.0525	0.895	0.041004	0.9388	0.024	0.968
20	8.00E-09	0.1162	0.7676	0.084018	0.8746	0.07575	0.899
30	1.20E-08	0.1245	0.751	0.08308	0.876	0.066	0.912
40	1.60E-08	0.1105	0.779	0.06834	0.898	0.051	0.932
50	2.00E-08	0.0865	0.827	0.0536	0.92	0.037125	0.9505
60	2.40E-08	0.058	0.884	0.03886	0.942	0.0285	0.962
70	2.80E-08	0.03385	0.9323	0.0268	0.96	0.018375	0.9755
80	3.20E-08	0.02	0.96	0.01608	0.976	0.012	0.984
90	3.60E-08	0.0144	0.9712	0.01005	0.985	0.00975	0.987
100	4.00E-08	0.0131	0.9738	0.0067	0.99	0.006	0.992

The mixing efficiency of the Tear-drop mixer for inlet flow-rate ratios of 1 to 3 is plotted in Figure 5.10 and efficiency curves show the same progression as like the Chain mixer. The mixing efficiency of the Tear-drop mixer depends moderately on the inlet flow-rate ratios, which interestingly increases for higher value of the ratios, especially at mid-range of Reynolds numbers. In the case of inlet flow-rate ratio of 1, the efficiency is less than 90% when Reynolds numbers vary from 20 to 60. Moreover, the efficiency is more than 90% for all Reynolds numbers in the case of inlet flow-rate ratios of 3.

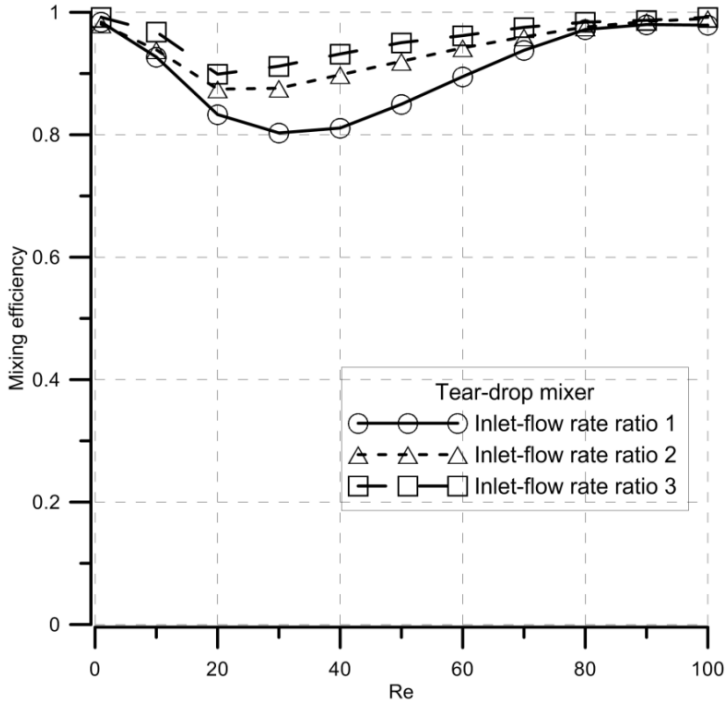

Figure 5.10 The numerical mixing efficiency of the Tear-drop micromixer for different inlet flow-rate ratios and varying Reynolds numbers ($1 \leq Re \leq 100$)

5.2.3 Y-Y Micromixer

The mixing efficiency of the new Y-Y mixer is also computed experimentally and numerically at a range of Reynolds number from 1 to 100. A reasonable agreement is found in the images taken in experimental test and numerical simulation at different Re numbers as indicated in Figure 5.11. They nicely show the diffusion of fluids at the middle of Y channel. Nevertheless, there are some differences in the first and third Y channels. As described in section 2.5, there are different horizontal layers of fluids inside each Y channel and it is not possible to see all layers form top or bottom view in numerical simulation. In contrary, experimental images can capture the whole depth of the different horizontal layers.

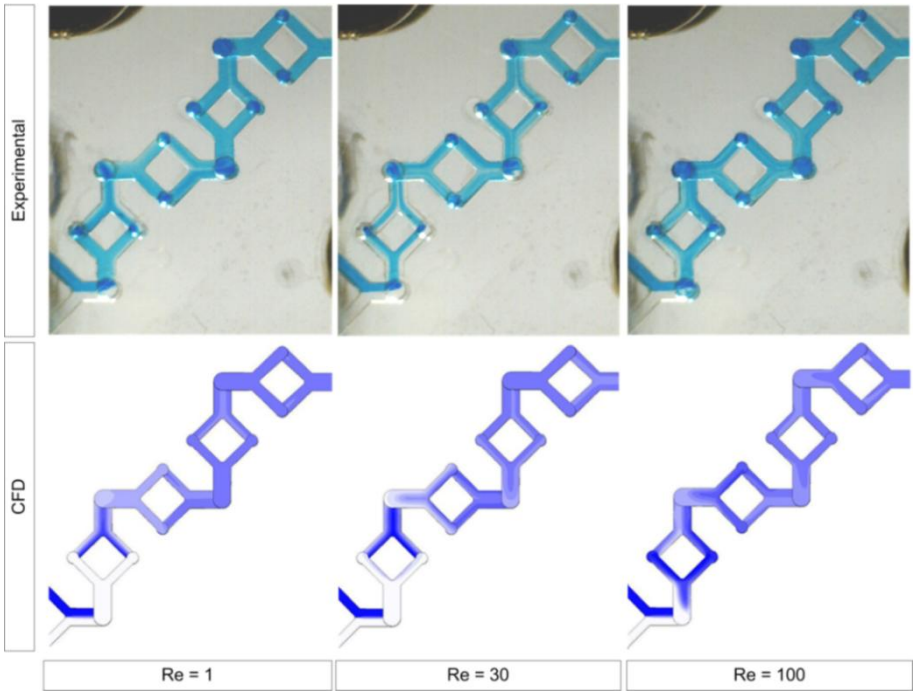

Figure 5.11 Comparison between the images taken from the computer simulation and the experiments of Y-Y mixer

Standard deviation (σ), mixing efficiency (η) and pressure-drop (ΔP) of the Y-Y mixer during experimental and numerical investigation is presented in Table 5.5.

Table 5.5 Standard deviation (σ), mixing efficiency (η) and pressure-drop (Δ*P*) during experimental investigation of Y-Y mixer (Flow-rate ratio of 1)

Re	Flow rate (Q) (m^3/s)	Experimental			Numerical		
		Standard deviation (σ)	Mixing efficiency (η)	Pressure drop (Δ*P*) (Pa)	Standard deviation (σ)	Mixing efficiency (η)	Pressure drop (Δ*P*) (Pa)
1	6.00E-10	0.0352	0.93	5	0.003	0.99	5
10	6.00E-09	0.0422	0.92	50	0.01	0.98	48.6
20	1.20E-08	0.0269	0.95	100	0.032	0.94	100
30	1.80E-08	0.0518	0.90	175	0.052	0.90	154
40	2.40E-08	0.0353	0.93	250	0.042	0.92	213
50	3.00E-08	0.036	0.93	350	0.027	0.95	276
60	3.60E-08	0.0504	0.90	450	0.036	0.93	345
70	4.20E-08	0.0265	0.95	550	0.042	0.92	420
80	4.80E-08	0.0269	0.95	650	0.03	0.94	499
90	5.40E-08	0.0484	0.90	750	0.015	0.97	583
100	6.00E-08	0.0369	0.93	900	0.004	0.99	673

An overall comparison of the experimental and numerical gathered data is given by Figure 5.12, which shows the mixing efficiency obtained at the exit of the examined mixers, varying Reynolds numbers. First of all, a good agreement was found between numerical and experimental results; in fact, both methods highlighted an almost flat efficiency curve for the Y-Y mixer, with a mixing efficiency higher than 90%.

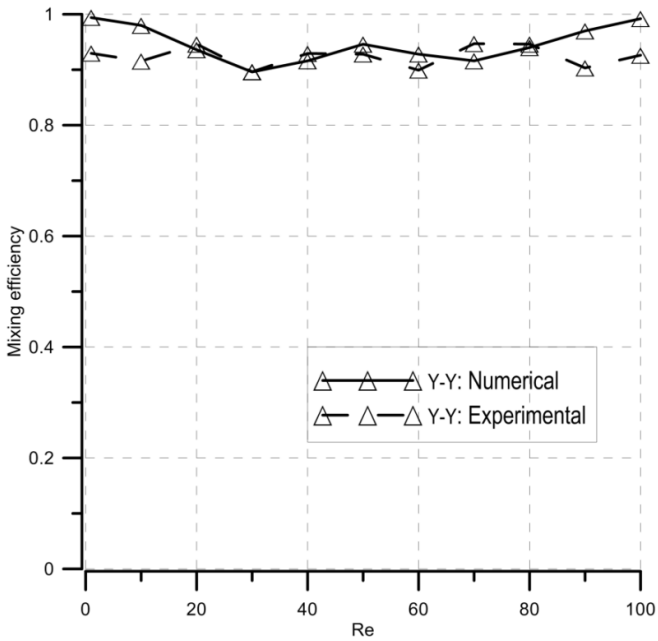

Figure 5.12 Experimental and numerical mixing efficiency of the Y-Y mixer at the exit of the fourth element

Figure 5.13 shows pressure-drop dependence on corresponding Re numbers. It can be noted that experimental and numerical pressure drop increase with the Reynolds numbers and the final pressure drop is around 800 Pa at *Re* = 100.

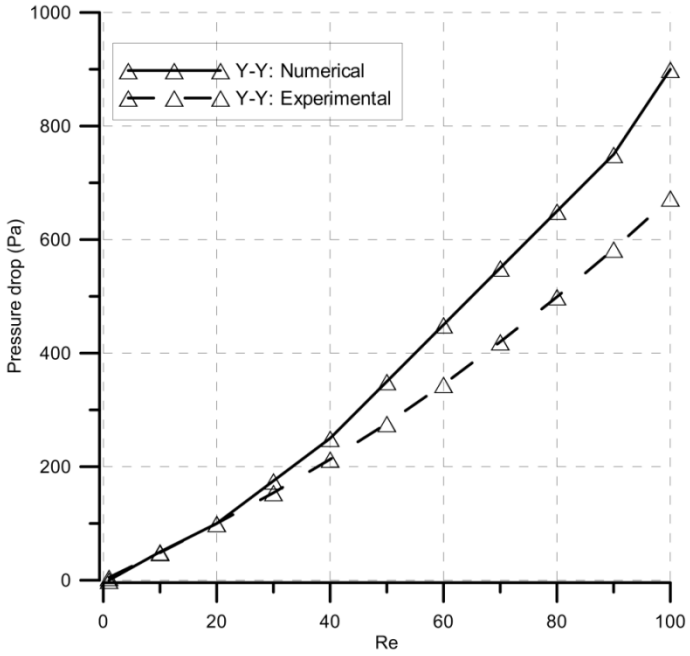

Figure 5.13 Experimental and numerical pressure-drop of the Y-Y mixer, varying *Re* numbers

Standard deviation (σ) and mixing efficiency (η) of the Y-Y mixer during numerical investigation for different inlet flow-rate ratios is shown in Table 5.6.

Table 5.6 Standard deviation (σ) and mixing efficiency (η) during numerical investigation of Y-Y mixer

Re	Flow rate (Q) (m^3/s)	Flow-rate ratio 1		Flow-rate ratio 2		Flow-rate ratio 3	
		Standard deviation (σ)	Mixing efficiency (η)	Standard deviation (σ)	Mixing efficiency (η)	Standard deviation (σ)	Mixing efficiency (η)
1	6.00E-10	0.003	0.99	0.000938	0.9986	0.006075	0.9919
10	6.00E-09	0.01	0.98	0.000201	0.9997	0.0027	0.9964
20	1.20E-08	0.032	0.94	0.000402	0.9994	0.00345	0.9954
30	1.80E-08	0.052	0.90	0.003283	0.9951	0.01275	0.983
40	2.40E-08	0.042	0.92	0.004556	0.9932	0.0174	0.9768
50	3.00E-08	0.027	0.95	0.001809	0.9973	0.009	0.988
60	3.60E-08	0.036	0.93	0.000737	0.9989	0.00435	0.9942
70	4.20E-08	0.042	0.92	0.00134	0.998	0.005925	0.9921
80	4.80E-08	0.03	0.94	0.00134	0.998	0.005625	0.9925
90	5.40E-08	0.015	0.97	0.000536	0.9992	0.00375	0.995
100	6.00E-08	0.004	0.99	0.00067	0.999	0.001875	0.9975

Figure 5.14 provides the mixing efficiency of the Y-Y mixer for inlet flow-rate ratios from 1 to 3. The efficiency curves show the same trend for different inlet flow-rate ratios and the efficiency slightly increases for higher ratios. Mixing efficiency is about 90% at inlet flow-rate ratio of 1 but efficiency is more than 95% for both flow-rate ratios of 2 and 3.

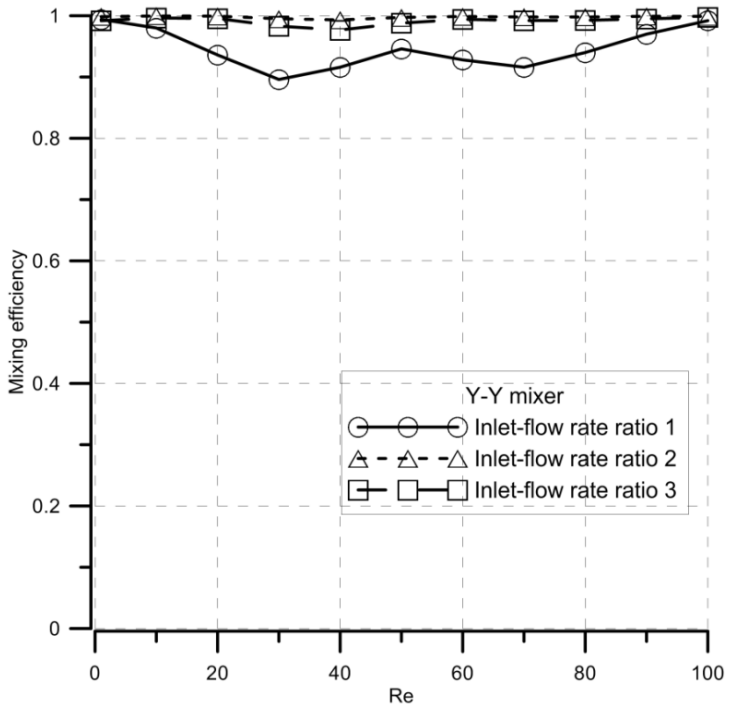

Figure 5.14 The numerical mixing efficiency of the Y-Y micromixer for different inlet flow-rate ratios and varying Reynolds numbers ($1 \leq Re \leq 100$)

5.2.4 H-C Micromixer

Mixing efficiency and pressure-drop of the H-C mixer was computed at different Reynolds numbers. Figure 5.15 illustrates the concentration distribution of fluids along the length of the mixer in both experimental tests and numerical simulations. There is a satisfactory agreement between experimental and numerical images taken at different *Re* numbers which shows various vertical layers of fluids.

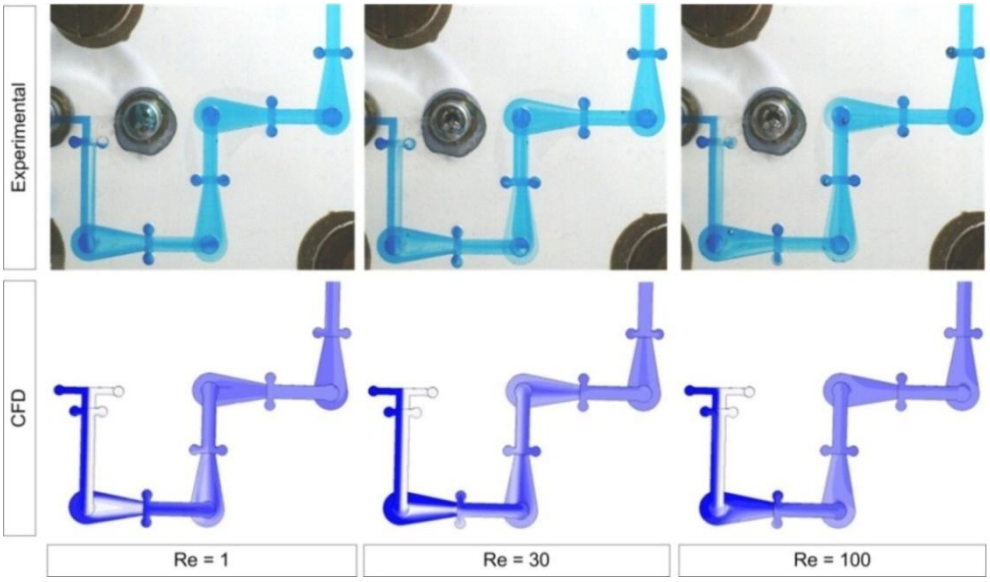

Figure 5.15 Comparison between the images taken from the computer simulation and the experiments of H-C mixer

Standard deviation (σ), mixing efficiency (η) and pressure-drop (ΔP) of the H-C mixer during experimental and numerical investigation is given in Table 5.7.

Table 5.7 Standard deviation (σ), mixing efficiency (η) and pressure-drop (ΔP) during experimental investigation of H-C mixer (Flow-rate ratio of 1)

Re	Flow rate (Q) (m^3/s)	Experimental			Numerical		
		Standard deviation (σ)	Mixing efficiency (η)	Pressure drop (ΔP) (Pa)	Standard deviation (σ)	Mixing efficiency (η)	Pressure drop (ΔP) (Pa)
1	8.00E-10	0.0385	0.923	50	0.01925	0.9615	8.228
10	8.00E-09	0.0795	0.841	100	0.0225	0.955	84.88
20	1.60E-08	0.05	0.9	200	0.01	0.98	181.19
30	2.40E-08	0.035	0.93	300	0.01445	0.9711	293.6
40	3.20E-08	0.0525	0.895	400	0.0243	0.9514	423.52
50	4.00E-08	0.0425	0.915	550	0.0307	0.9386	570.96
60	4.80E-08	0.0525	0.895	750	0.03015	0.9397	735.9
70	5.60E-08	0.049	0.902	900	0.0275	0.945	918.33
80	6.40E-08	0.0425	0.915	1050	0.0246	0.9508	1118.3
90	7.20E-08	0.0385	0.923	1250	0.0226	0.9548	1335.5
100	8.00E-08	0.0375	0.925	1450	0.02105	0.9579	1570.3

Figure 5.16 displays the mixing efficiency of the H-C mixer with increasing Reynolds numbers at the output of fourth element. As shown, experimental and numerical curves have reasonable

agreement. Mixing efficiency curves show a flat characteristic and efficiency is almost 90% irrespective of Re numbers.

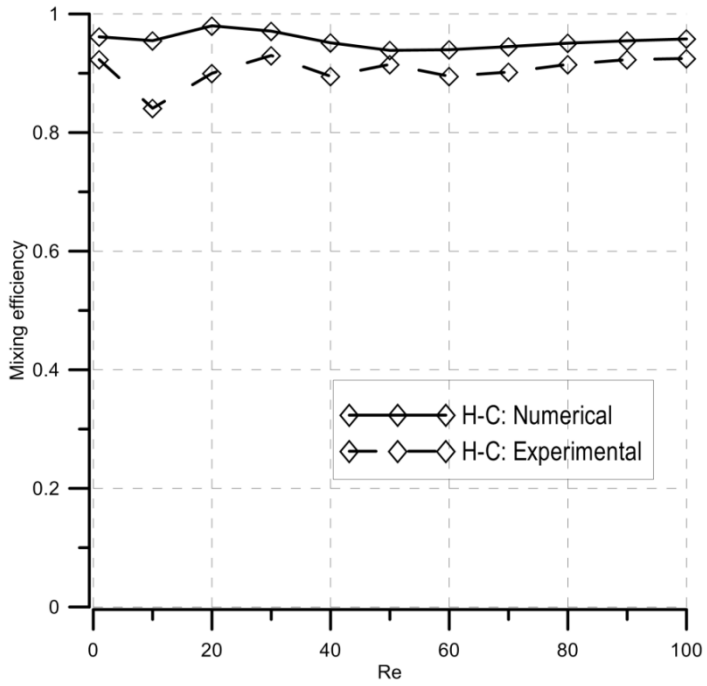

Figure 5.16 Experimental and numerical mixing efficiency of the H-C mixer at the exit of the fourth element

Figure 5.17 reports the comparison of experimental and numerical pressure-drop (ΔP) of the H-C micromixer. Numerical and experimental curves shows good agreement and have the same behavior, i.e. pressure drop increases with the increase of Re numbers. The maximum pressure drop is about 1600 Pa at *Re*= 100.

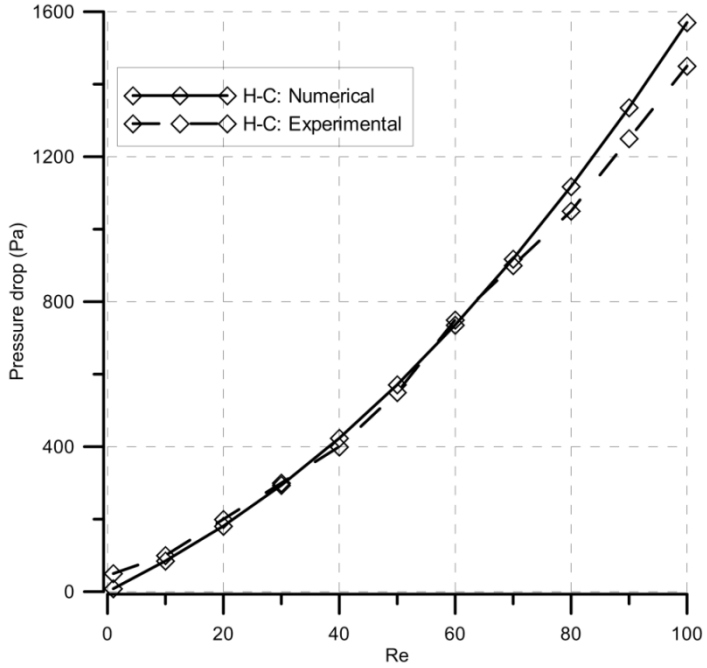

Figure 5.17 Experimental and numerical pressure drop of the H-C micromixer

The mixing efficiency of the H-C mixer for different inlet flow-rate ratios is listed in Table 5.8.

Table 5.8 Standard deviation (σ) and mixing efficiency (η) during numerical investigation of H-C mixer

Re	Flow rate (Q) (m^3/s)	Flow-rate ratio 1		Flow-rate ratio 2		Flow-rate ratio 3	
		Standard deviation (σ)	Mixing efficiency (η)	Standard deviation (σ)	Mixing efficiency (η)	Standard deviation (σ)	Mixing efficiency (η)
1	8.00E-10	0.01925	0.9615	0.008308	0.9876	0.005647	0.9925
10	8.00E-09	0.0225	0.955	0.015745	0.9765	0.009789	0.987
20	1.60E-08	0.01	0.98	0.00737	0.989	0.005271	0.993
30	2.40E-08	0.01445	0.9711	0.009648	0.9856	0.007078	0.9906
40	3.20E-08	0.0243	0.9514	0.01407	0.979	0.009864	0.9869
50	4.00E-08	0.0307	0.9386	0.017554	0.9738	0.011596	0.9846
60	4.80E-08	0.03015	0.9397	0.019028	0.9716	0.012274	0.9837
70	5.60E-08	0.0275	0.945	0.019832	0.9704	0.013253	0.9824
80	6.40E-08	0.0246	0.9508	0.020435	0.9695	0.014081	0.9813
90	7.20E-08	0.0226	0.9548	0.020904	0.9688	0.014864	0.98026
100	8.00E-08	0.02105	0.9579	0.021507	0.9679	0.015512	0.9794

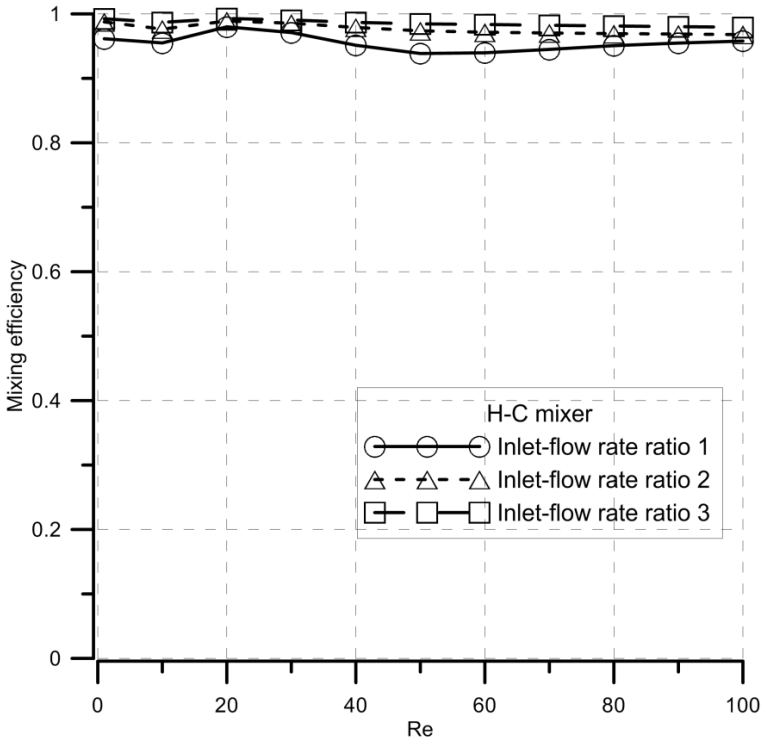

Figure 5.18 The numerical mixing efficiency of the H-C micromixer for different inlet flow-rate ratios and varying Reynolds numbers ($1 \leq Re \leq 100$)

Figure 5.18 revels the efficiency curves for different inlet flow-rate ratios and the curves show the same trend and the efficiency slightly increases for higher inlet flow-rate ratios, especially at 30 ≤ *Re* ≤ 100. In the case of the Chain and Tear-drop mixers, the efficiency is relatively low at 10 ≤ *Re* ≤ 40, whereas the Y-Y and the H-C mixers show considerably higher efficiency. The overall mixing efficiency is more than 90% at all Reynolds numbers, regardless of the inlet flow-rate ratios.

5.2.5 Comparison of Mixing Efficiency

The mixing efficiency of the Chain, the Tear-drop, the H-C and the Y-Y mixers was evaluated experimentally and numerically in a range of Reynolds numbers from 1 to 100. Figure 5.19 shows the concentration distribution of liquid (water) on various cross-sectional planes along the channel of the four mixers at *Re* =50.

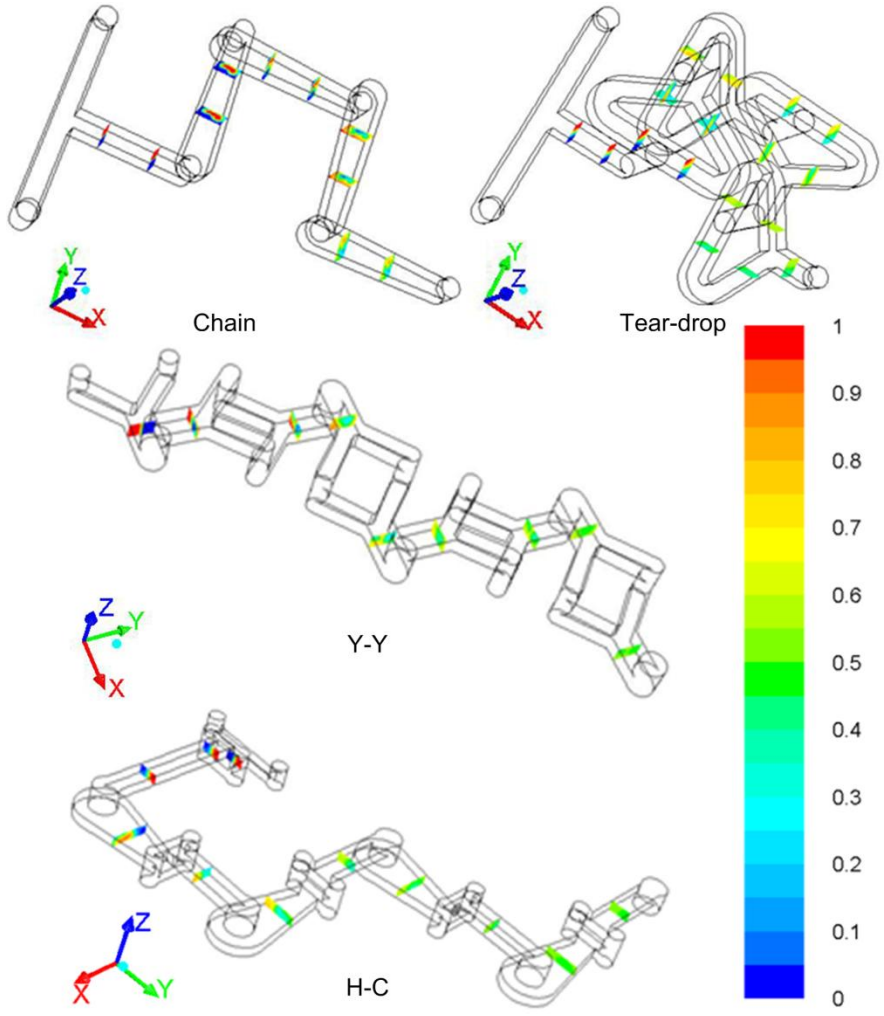

Figure 5.19 The mass fraction of water along the micromixers at *Re* = 50

The overall comparison of the mixing efficiency of all the examined mixers is reported in Figure 5.20. It is evident that the efficiency of the Chain and the Tear-drop mixers strongly depends on Reynolds numbers. At *Re* = 1, efficiencies of the Chain and the Tear-drop mixers are equal to 70% and 90%, respectively; then, they decrease as the Reynolds numbers increase up to around 30. Afterwards, efficiencies increase again until a value of 90% is obtained at high Reynolds numbers. In particular, mixing efficiencies are less than 80% at the middle range of Reynolds numbers ($20 \leq Re \leq 50$). On the other hand, the efficiency of both the H-C and the Y-Y mixers is independent on Reynolds numbers with a value of more than 90%.

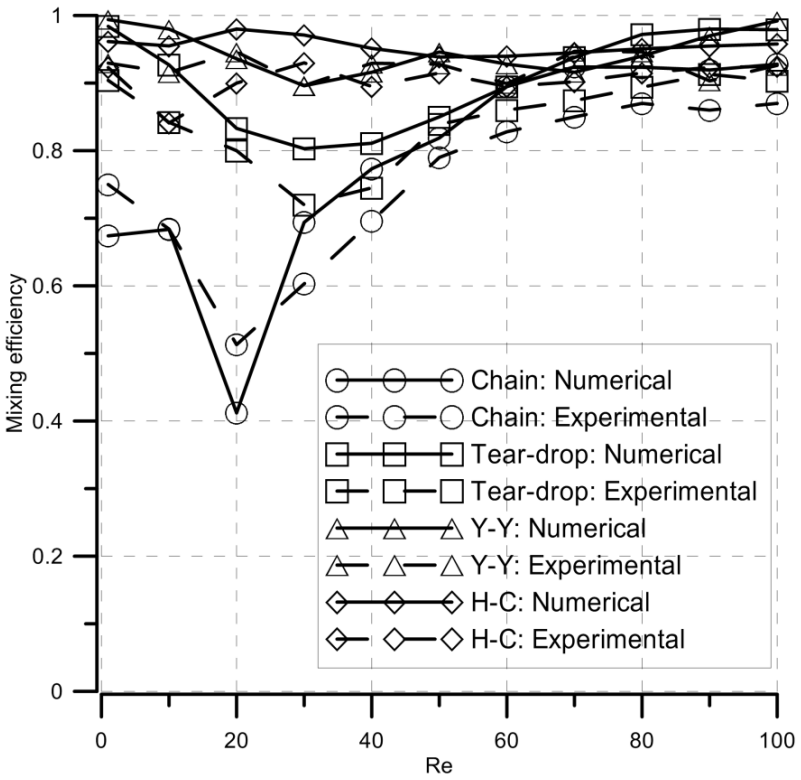

Figure 5.20 Experimental and numerical mixing efficiency of the mixers at the exit of the fourth element

The dependency of mixing efficiency on the number of elements was also studied and Table 5.9 provides the numerical and experimental values.

Table 5.9 Mixing efficiency (η) during numerical and experimental investigation of Chain, Tear-drop, H-C and Y-Y mixers corresponding to number of elements (Flow-rate ratio of 1)

Re	Number of element	Chain		Tear-drop		Y-Y		H-C	
		Experimental	Numerical	Experimental	Numerical	Experimental	Numerical	Experimental	Numerical
1	1	0.356	0.377	0.477	0.515	0.64	0.654	0.611	0.632
	2	0.584	0.6511	0.635	0.623	0.92	0.954	0.828	0.849
	3	0.754	0.8033	0.728	0.768	0.925	0.982	0.86	0.9088
	4	0.83	0.8391	0.839	0.827	0.93	0.996	0.915	0.9386
30	1	0.31	0.335	0.42	0.459	0.515	0.523	0.58	0.6359
	2	0.45	0.489	0.55	0.595	0.8	0.802	0.76	0.8019
	3	0.5	0.55	0.67	0.6964	0.89	0.924	0.88	0.9164
	4	0.601	0.618	0.72	0.751	0.91	0.955	0.93	0.9711

Figure 5.21 demonstrates the dependency of mixing efficiency on the number of elements at *Re* = 1 and at *Re* = 30. As expected, mixing efficiency increases with the number of elements. At low Reynolds (*Re* = 1) numbers, efficiency is less than 60% at the exit of first element; it gradually increases with the number of elements and finally efficiency exceeds 80% at the exit of the forth element. Increasing Reynolds numbers up to 30, the performance of the Tear-drop and the Chain mixers is clearly reduced. On the contrary, the Y-Y and the H-C mixers show good performance and efficiency is about 80% after the second element which is about two times more than the other two mixers.

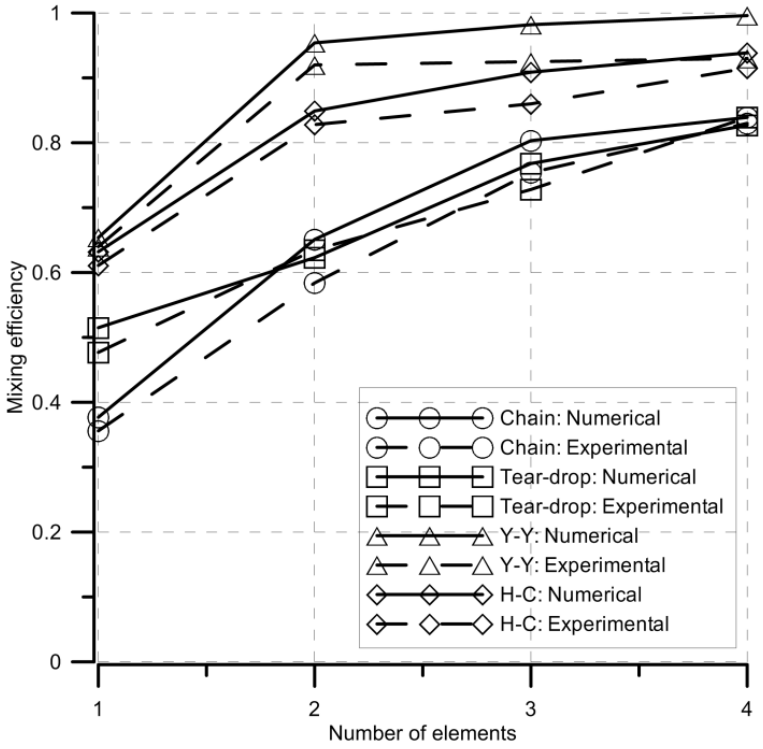

(a) Re = 1

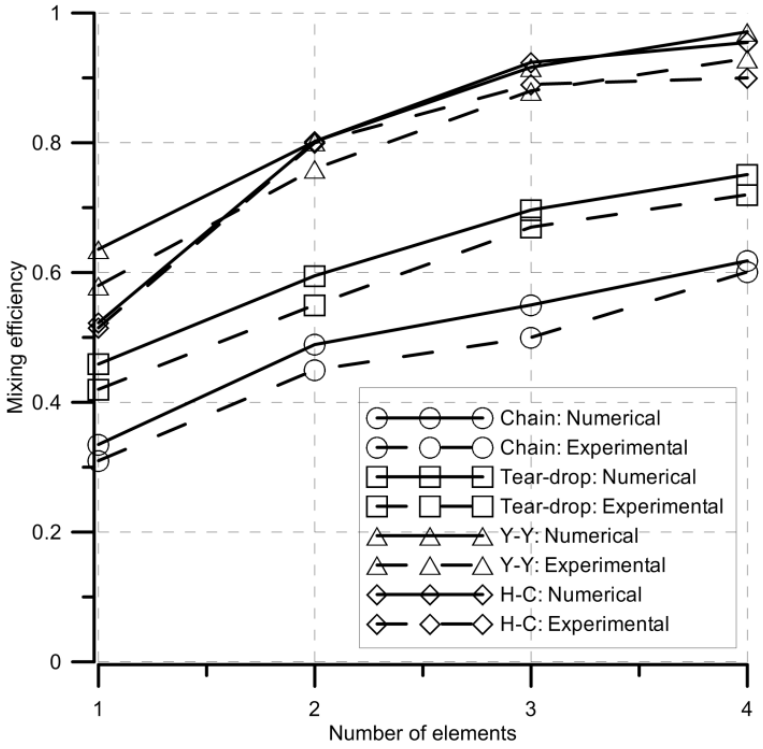

(b) Re = 30

Figure 5.21 Experimental and numerical mixing efficiency of the micromixers, varying their number of elements

5.2.6 Comparison of Pressure-drop

Pressure-drop (ΔP) of the four micromixers was evaluated experimentally as well as numerically. As an example, Figure 5.22 presents a comparison of numerical pressure-drop of the four micromixers at a flow rate of 2×10^{-8} m^3/s.

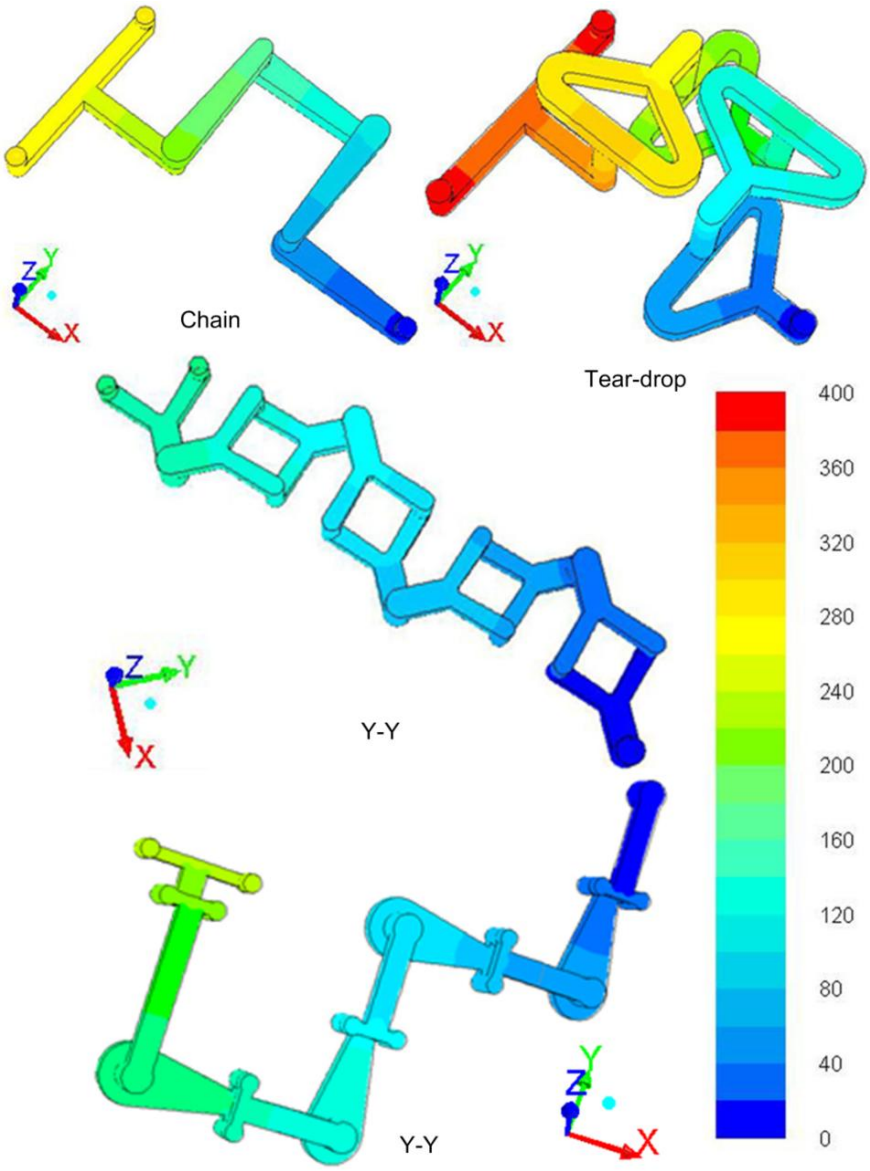

Figure 5.22 Numerical pressure-drop along the four mixers at a flow rate of 2×10^{-8} m^3/s

As demonstrates in Figure 5.23, numerical and experimental curves have the same trend, i.e. pressure-drop increases with the increase of flow rate. The maximum relative error is of about 10% except for the Chain mixer; in this case, a maximum error of 17% is detected, which can be explained by some defects of the prototype. At low flow rates, the pressure drop is linearly

dependent on flow rate, due to the multi-laminated flow of fluids. As flow rate increases, vortexes are introduced in the fluid stream and, consequently, the pressure drop curve moves away from the linearity. It is also clear that both Y-Y and H-C mixer have two times less pressure drop than the other two mixers

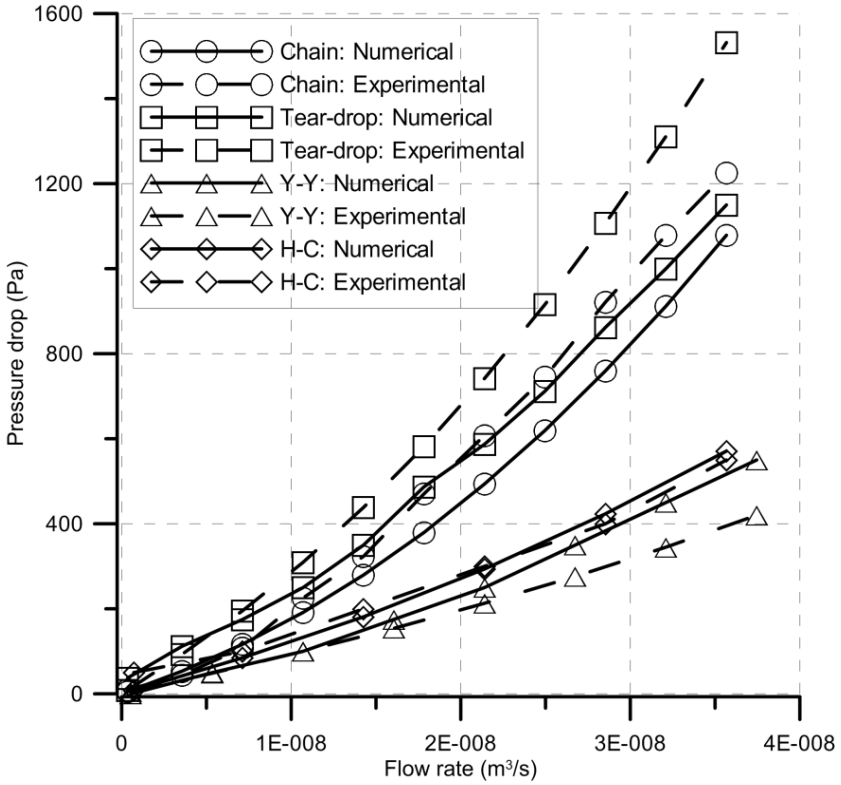

Figure 5.23 Experimental and numerical pressure drop of the four micromixers, varying flow rate

A dimensionless pressure drop (K) was also introduced to facilitate a comparison with other SAR micromixers. It was calculated as

$$K = \frac{\Delta P}{(1/2)\rho v^2} \qquad \textbf{5.1}$$

where ΔP is the pressure-drop, ρ is the fluid density, and v is the fluid velocity.

Figure 5.24 plots the dimensionless pressure-drop dependency on Reynolds numbers obtained numerically as well as experimentally for all the micromixers. As shown, four micromixers have almost the same behavior.

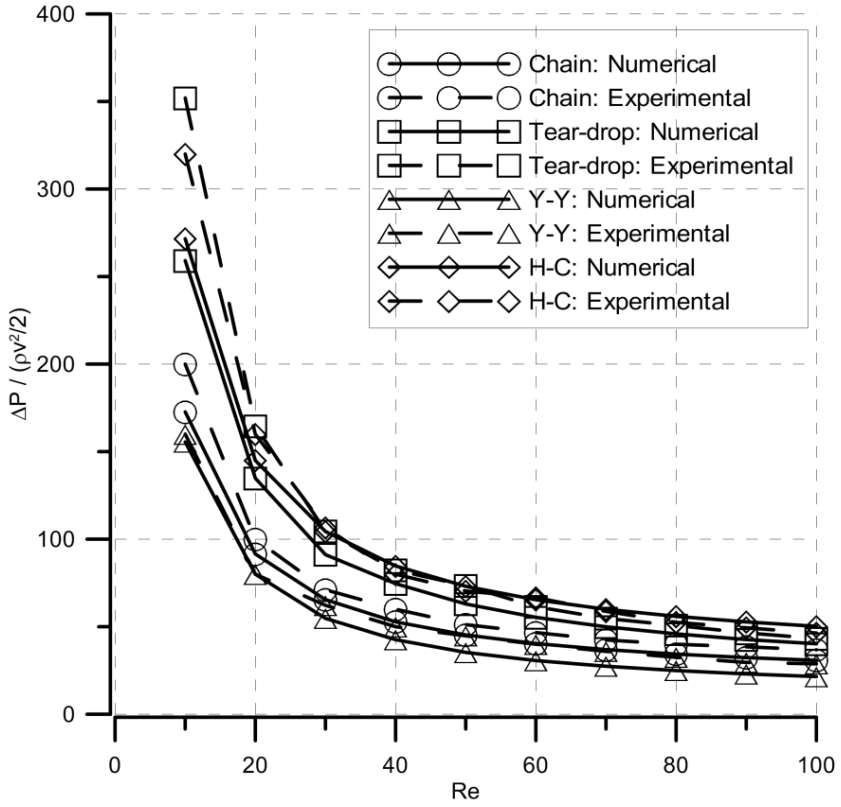

Figure 5.24 Experimental and numerical dimensionless pressure-drop of the four micromixers, varying Reynolds numbers

5.3 Flow Regime

The flow patterns inside the four mixers were examined numerically. Figure 5.25 shows the three-dimensional path line distributions inside the Chain, the Tear-drop, the Y-Y and the H-C micromixers at *Re* = 1, *Re* = 30 and *Re* = 100.

At low Reynolds numbers (*Re* =1) there is a stratified flow in which the streamlines are scarcely bent and follow the channel walls, as shown in Figure 5.25. Under this flow regime, mixing is entirely due to diffusion and a good mixing efficiency is expected, as found in the experimental and numerical results (Figure 5.20). At *Re* = 30 (medium velocity), the vortex flow regime is obtained. Here, vortices start building up inside the channels. Since there is a shorter residence time for the fluid particles to diffuse, a worse mixing efficiency could be expected. Never the less, in the case of the H-C and the Y-Y mixers the three-dimensional change of direction in the channel geometry promotes a helical fluid motion, which occurs at the inlet of each Chain module, H module and Y module. Consequently, the fluid path is lengthened and the interfacial area between fluids is increased, which compensate for residence time reduction. This swirling effect is less evident in both the Chain and the Tear-drop mixers, as can be seen in Figure 5.1 and Figure 5.2; the trend of

the mixing efficiency characteristic shown in Figure 5.20 also supports this argument. At high Reynolds numbers (higher velocity), the path line distributions become more intricate, amply compensating for the increase of fluid velocity. Therefore, all mixers present good mixing efficiency (see Figure 5.20).

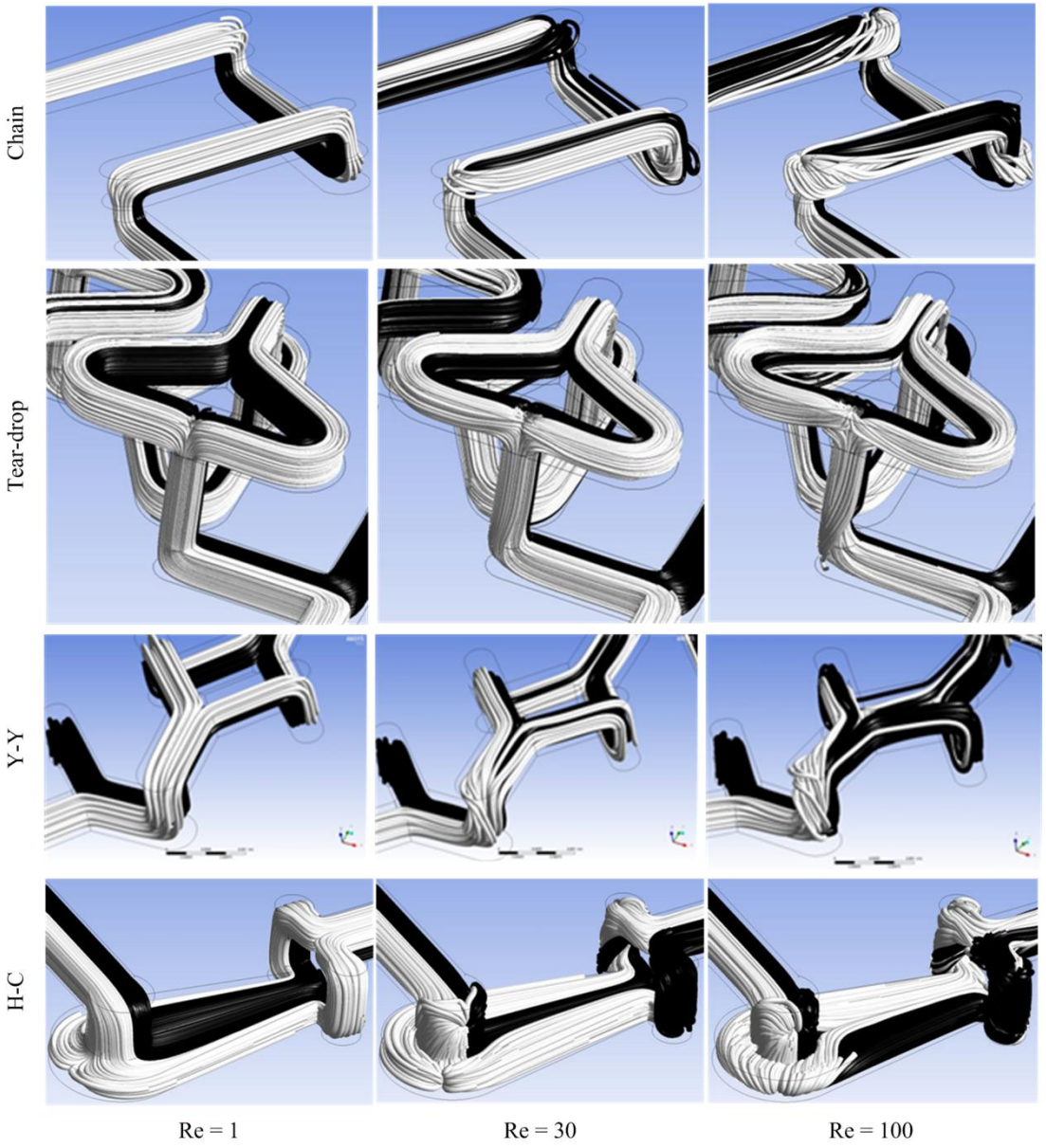

Figure 5.25 Path line inside the four mixers at the exit of the first element, varying Reynolds numbers

A closer inspection of the fluid inside the microchannels permits to highlight secondary flow. Figure 5.26 provides velocity vectors plotted on the *Y–Z* plane at the rectangular channel just after the inlets of the three micromixers, varying Reynolds numbers. As shown, at low Reynolds numbers the secondary flow is almost negligible in all the mixers. At the mid-range of Reynolds

numbers, a couple of two counter rotating vortexes appear which is typical of the vortex flow regime. This vortex structure persists at *Re* = 100 with a higher intensity.

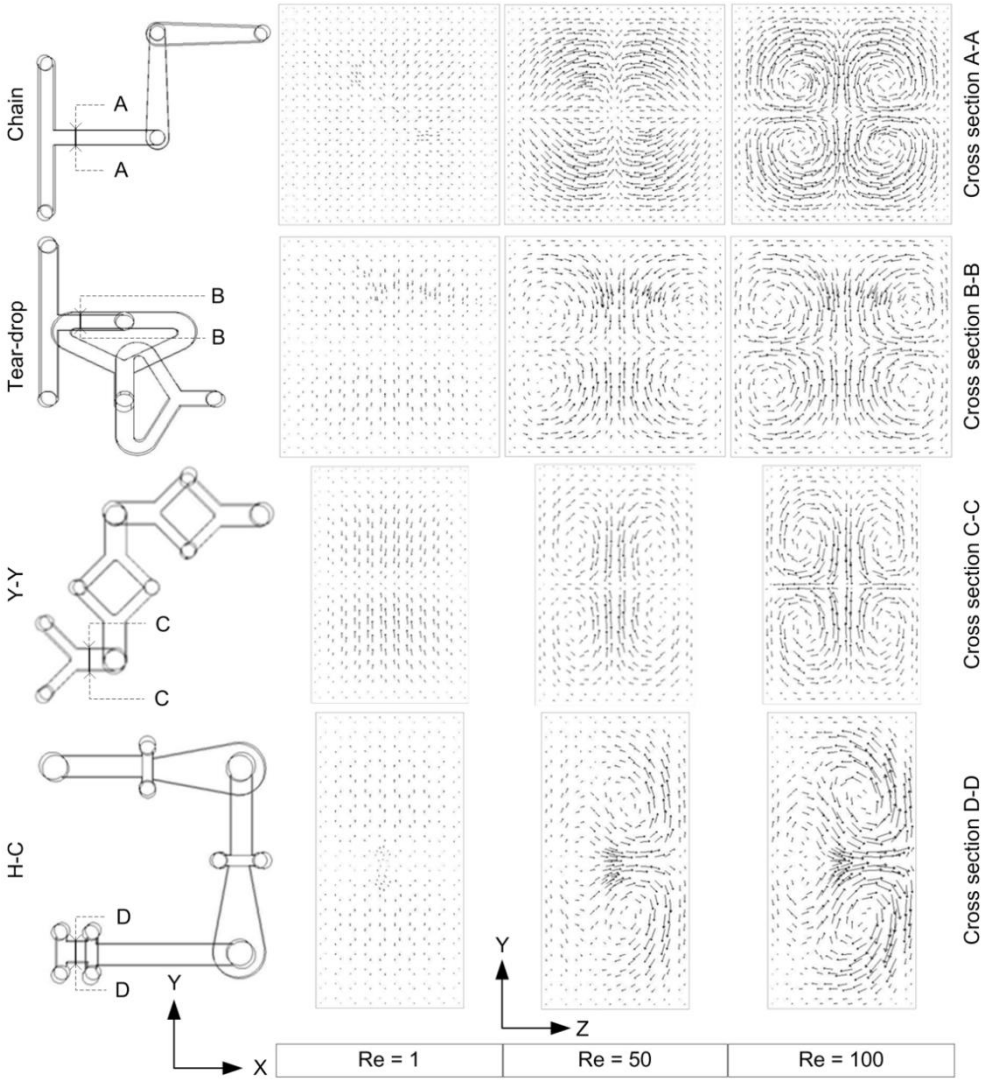

Figure 5.26 Velocity vectors highlighting secondary flow at the rectangular channel just after the inlets of the four micromixers, varying Reynolds numbers

The effect of geometry on secondary flow is summarized in Figure 5.27. The velocity vectors are plotted on the *Y–Z* plane at the exit of the second element of each micromixer, at different Reynolds numbers. In particular, in order to estimate the intensity of the secondary flow and to compare it with that of the main flow, this figure also reports the mean value *v* of the main flow velocity and the mean value v_{yz} of the secondary flow velocity. For this purpose, *v* and v_{yz} are calculated as:

$$v = \frac{\sum_{N}^{i=1}(\sqrt{v_{xi}^2 + v_{yi}^2 + v_{zi}^2})}{N} \qquad \textbf{5.2}$$

$$v_{yz} = \frac{\sum_{N}^{i=1}(\sqrt{v_{yi}^2 + v_{zi}^2})}{N} \quad \textbf{5.3}$$

where v_x, v_y and v_z are the components of the flow velocity vector along the *x*, *y* and *z* direction, respectively, and *N* is the number of sample cells in the cross section. As shown, in the case of the Chain mixer, the effect of the secondary flow is negligible over the whole range of Reynolds numbers examined. In the case of the Tear-drop, the mean velocity of the secondary flow becomes only one order of magnitude lower than that of the main flow both at the middle and at the top range of Reynolds numbers; nevertheless, a swirling structure can be detected only at *Re* = 100. Conversely, in the case of the H-C and the Y-Y mixers, a clear swirling structure can be detected already at the mid-range of Reynolds numbers.

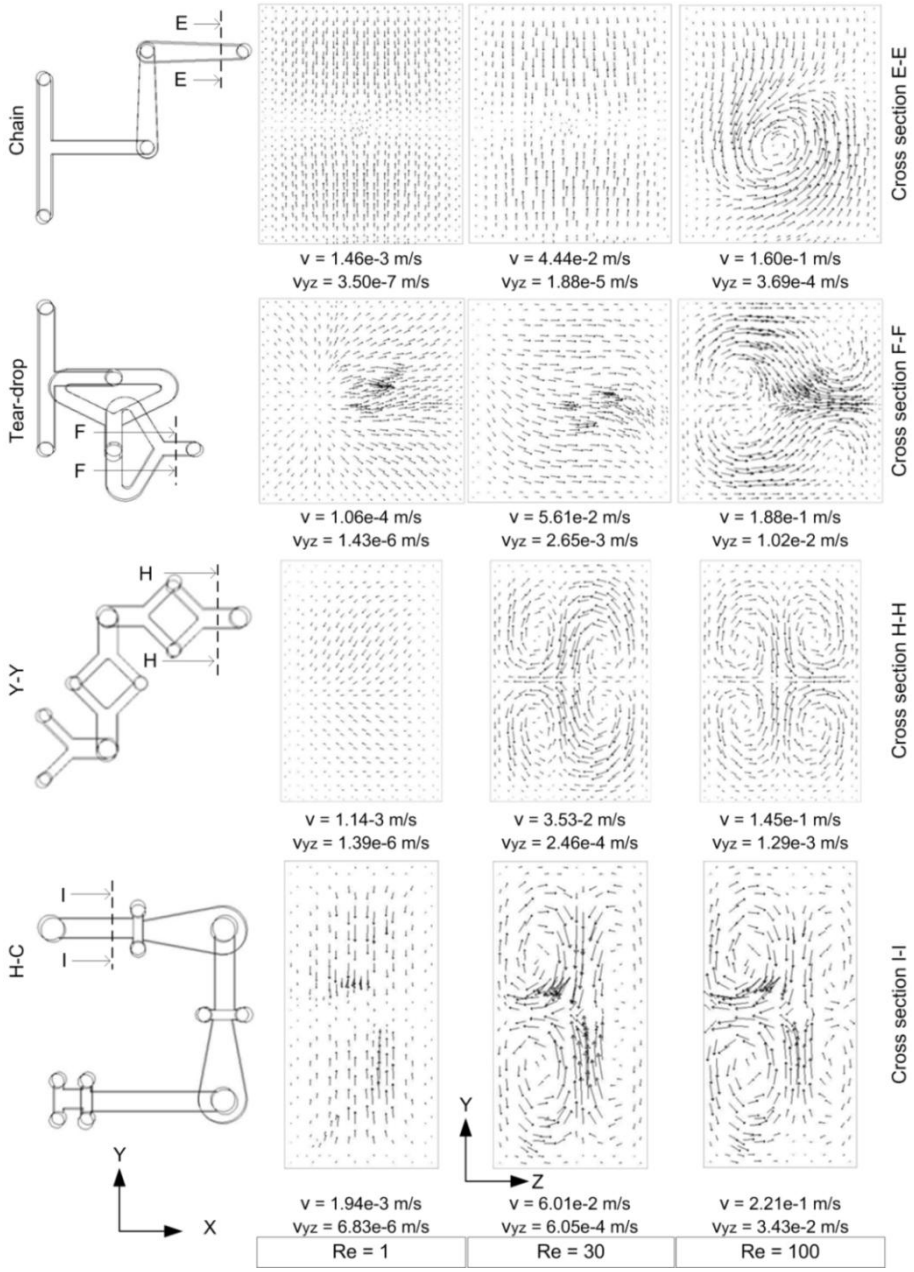

Figure 5.27 Velocity vectors highlighting secondary flow at the exit of the second element of the four micromixers, varying Reynolds numbers

5.4 RTD Analysis

The results of the RTD analysis based on CFD simulations and mean residence time are presented and discussed in this section. RTD is chosen for this work because it serves as a reasonable indicator of the type and extent of mixing in a flow system. Although the concept of RTD is not new when applied to conventional flow systems, its application to the characterization of flow and mixing in micromixers is still novel (116). The RTD of four mixers were measured numerically for

different Reynolds numbers. The various parameters (mean residence time, CoV, variance and skewness) were computed using equations 4.3 to 4.10 and the corresponding data are presented in Table 5.10.

Table 5.10 Results of the numerical RTD analysis at different Reynolds numbers

Name	Re	Residence time (sec)	CoV	Variance	Skewness
Chain	1	16.656	0.3178	44.046	34.548
	10	1.770	0.2964	0.4535	2.592
	30	0.5164	0.3882	0.8495	0.3505
	100	0.1365	0.2255	0.00182	0.0295
Tear-drop	1	27.087	0.3767	220.238	222.693
	10	2.7246	0.2845	0.39809	3.7532
	30	0.7655	0.2992	0.987	0.7149
	100	0.2237	0.2263	0.00445	0.0441
Y-Y	1	32.142	0.3190	186.3927	132.366
	10	3.2521	0.3267	1.9515	4.0635
	30	1.0561	0.3079	0.1897	0.7813
	100	0.2968	0.1964	0.00576	0.05137
H-C	1	41.897	0.2599	204.329	151.876
	10	4.293	0.2664	2.7732	8.6432
	30	1.331	0.1916	0.1276	0.7068
	100	0.4208	0.1533	0.00727	0.06319

The virtue of different design of mixers generates flow/mixing patterns that should lead to narrower RTD, which can in principle also favor high conversion with improved yield and selectivity. Therefore, by imposing certain geometric constraints on a microchannel with associated mixing mechanism(s) for mixing enhancement, flow pattern can be improved in a manner that flow is dominated by transverse or radial mixing instead of back mixing. This transverse mixing leads to narrow RTD for good reactor performance in a flow microchannel. In this context, the smaller the variance or the CoV, the narrower RTD, and better the mixing quality.

Figure 5.28 shows the density distribution of fluid inside each element of the four mixers at *Re* =10. It can be seen that the particles experience a high peak followed by a long tail which is due to particles trapped in the channel that take longer time to get out of the system. It is also clear that

particle spend more time inside the Y-Y and H-C mixers than the Chain and Tear-drop mixer (see Table 5.10), which is due to their long channel length.

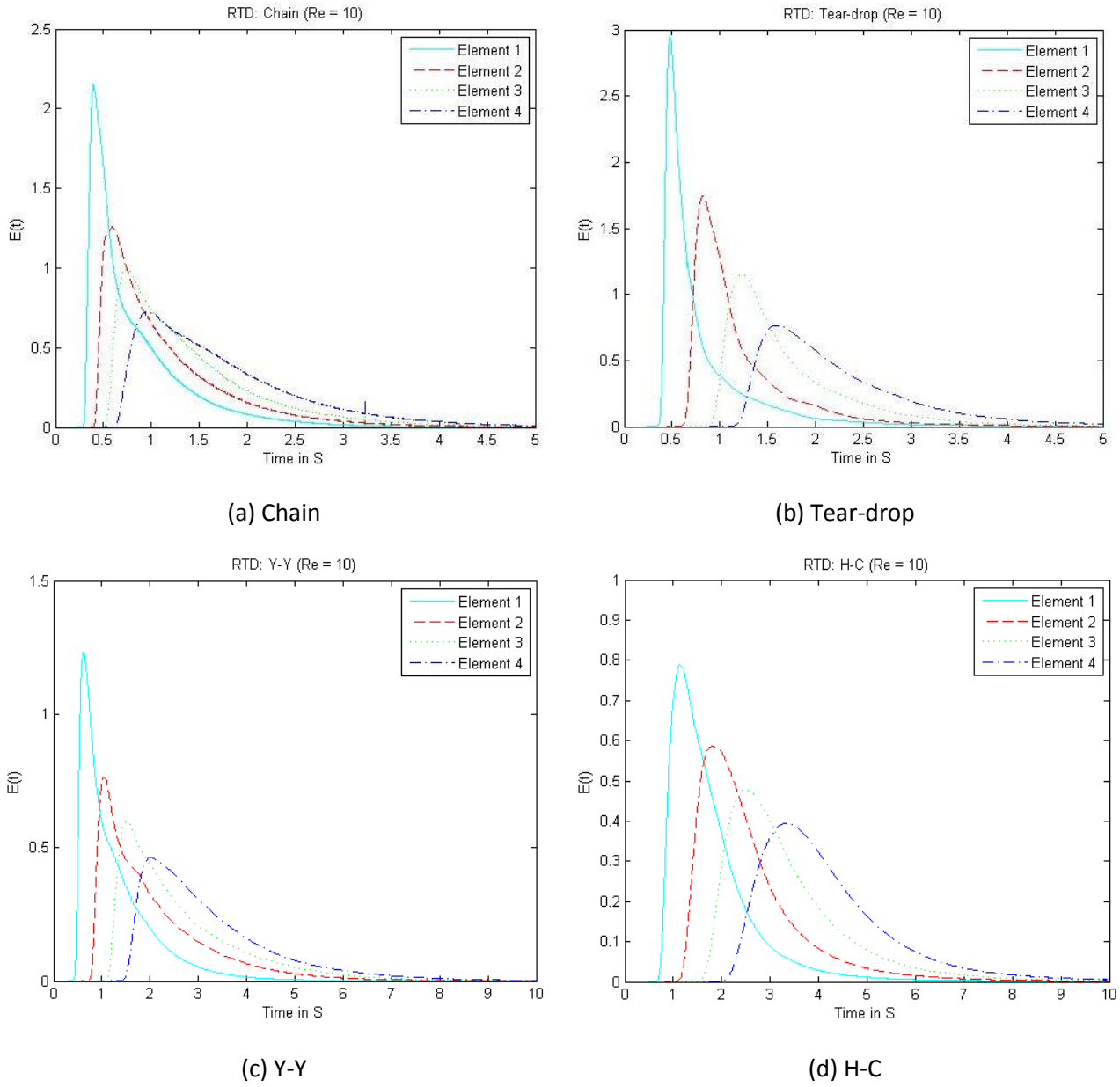

(a) Chain (b) Tear-drop

(c) Y-Y (d) H-C

Figure 5.28 Density distribution curves of four investigated micromixers at *Re* = 10

To compare different micromixers, the normalized density distribution of particles with respect to dimensionless time (E (θ) vs. θ) was constructed at different Reynolds number as shown in Figure 5.29. Generally, all micromixers show similar behavior. At low Reynolds numbers the distributions are broader and at higher Reynolds numbers the RTD curves become narrower and more

symmetric. A curve with a sharp peak or narrower peak, which also gives low value of CoV, denotes better mixing efficiency. It is notable from Table 5.10 that the values of CoV and variance decrease with the increase of Reynolds numbers for both the Y-Y and the H-C mixers, which indicates the generation of secondary flow due to the helical fluid motion; as a result radial mixing have effect on total mixing performance. In the case of the Chain and the Tear-drop mixers, going from Reynolds number 10 to 30, the values of CoV and variance increase, which predicts a low mixing efficiency at that range.

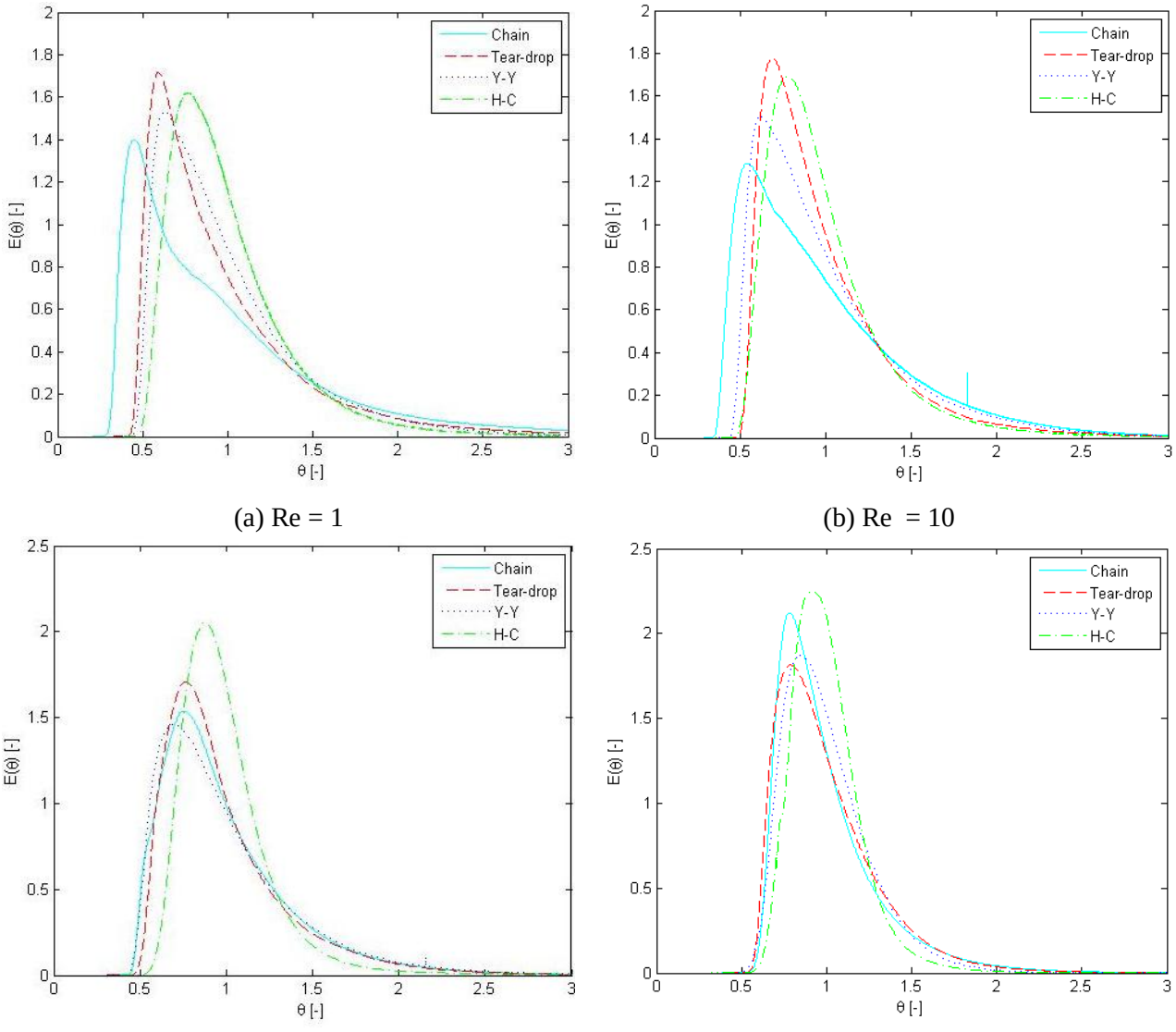

(a) Re = 1 (b) Re = 10

(c) Re = 30 (d) Re = 100

Figure 5.29 Normalized RTD of four investigated mixers at different Reynolds numbers

References

1. *Experimental investigation of passive micromixers conceptual design using the layout optimization method.* **Liu Y., Deng Y., Zhang P., Liu Z., Wu Y.** 2013, J. Micromech. Microeng., Vol. 23, pp. 1-10.

2. *Passive Mixers in Microfluidic Systems: A Review.* **Lee C. Y., Wang W. T., Fu L. M.** 2015, Micromachines, Vol. 6.

3. *Design and Simulation of passive mixing in microfludic systems with geometric variation.* **Jeon W., Shin C. B.** 2009, Chemical Engineering Journal, Vol. 152, pp. 575-582.

4. *Micromixers—a review.* **Nguyen N., Wu Z.** 2005, J. Micromech. Microeng., pp. 1-16.

5. *A planer microfludic mixer based on logarithmic spirals.* **Scherr T., Quitadamo C., Tesvich P., Park D. S., Tiersch T., Hayes D., Choi J., Nandakumar K., Monroe W. T.** 2012, J. Micromech. Microeng. , Vol. 22, pp. 1-10.

6. *Mixing performance of a planer micromixer with circular obstructions in a curved microchannel.* **Alam A., Afzal A., Kim K. Y.** 92, 2015, Chemical Engineering Research and Design, pp. 423-434.

7. *Modeling and Optimization of Y-Type Micromixers.* **Rudyak V., Minakov A.** 2014, Micromachines, Vol. 5, pp. 886-912.

8. *Rotation effect in split and recombination micromixing.* **Lee S. W., Lee S. S.** 2008, Sensors and Actuators, Vol. 29, pp. 364-371.

9. *Optimization of microscale vortex generators in a microchannel using advanced response surface method.* **Cho H. H, Kim B. S., Kwak B. S., Shin S., Lee S., Kim K. M., Jung H. I.** 2011, International Journal of Heat and Mass Transfer, Vol. 54, pp. 118-125.

10. *A review on mixing in microfluidics.* **Suh Y. K., Kang S.** 2010, Micromachines, Vol. 1, pp. 82-111.

11. *Micromixers—a review on passive and active mixing principles.* **Hessel V., Löwe H., Schönfeld F.** 2008, Chemical Engineering Science, Vol. 60, pp. 2479-2501.

12. *Microfluidic Mixing: A Review.* **Lee C., Chang C., Wang Y., Fu L.** 2011, Int. J. Mol. Sci., Vol. 12, pp. 3263-3287.

13. *Rapid magnetic microfluidic mixer utilizing AC electromagnetic field.* **Wen C. Y., Yeh C. P., Tsai C.H., Fu L. M.** 2009, Electrophoresis, Vol. 30, pp. 4179-4186.

14. *Numerical analysis of a rapid microfluidic mixer.* **Wen C. Y., Liang K. P., Chen H., Fu L. M.** 2011, Electrophoresis, Vol. 32, pp. 3268-3276.

15. *Micromixer-assisted polymerization processes.* **Bally F., Serra C. A., Hessel v., Hadziioannou g.** 2011, Chem. Eng. Sci., Vol. 616, pp. 1449-1462.

16. *Enhancing particle dispersion in a passive planar micromixer using rectangular obstacles.* **Bhagat A. A. S., Papautsky I.** 2008, J. Micromech. Microeng., Vol. 18, pp. 1-9.

17. *Mixing analysis in a three-dimensional serpentine split-and-recombine micromixer.* **Hossain S., Kim K. Y.** 2015, Chemical Engineering Research and Design, Vol. 100, pp. 95-103.

18. *Modeling and optimization of Y-type micromixers.* **Rudyak v., Minakov a.** 2014, Micromachines, Vol. 5, pp. 886-924.

19. *Performance comparison of micromixers.* **Falk L., Commenge J. M.** 2010, Chemical Engineering Science, Vol. 65, pp. 405-411.

20. *Passive mixers in microfluidic systems: A review.* **Lee C. Y., Wang W. T., Liu C. C., Fu L. M.** 2016, Chemical Engineering Journal, Vol. 288, pp. 146-160.

21. *Micromixing Within Microfluidic Devices.* **Capretto L., Cheng W., Hill M., Zhang X.** 2011, Top Curr Chem., Vol. 304, pp. 27-68.

22. **Nguyen, N T.** *Micromixers: Fundamentals, Design and Fabrication.* s.l. : William Andrew.

23. *A novel generation of 3D SAR-based passive micromixer: efficient mixing and low pressure drop at a low Reynolds number.* **Viktorov V., Nimafar M.** 2013, J. Micromech. Microeng., Vol. 23, pp. 1-13.

24. *Micropumps, microvalves, and micromixers within PCR microfluidic chips: advances and trends.* **Zhang C, Xing D, Li.** 2007, Biotechnol Adv., Vol. 25, pp. 483–514.

25. *A highly uniform lamination micromixer with wedge shaped inlet channels for time resolved infrared spectroscopy.* **Buchegger W., Wagner C., Lendl B., Kraft M., Vellekoop M.** 2011, Microfluid. Nanofluid., Vol. 10, pp. 889-897.

26. *A novel passive micromixer: Lamination in a planar channel system.* **Tofteberg T., Skolimowski M., Andreassen E., Geschke O.** 2010, Microfluid. Nanofluid., Vol. 8, pp. 209-215.

27. *Experimental and numerical investigation into mixing efficiency of micromixers with different geometric barriers.* **Lee C. Y., Lin C. F., Hung M. F., Tsai C. H., Fu L. M.** 2006, Mater. Sci. Forum, pp. 505-507.

28. *Performance analysis of a folding flow micromixer.* **Chen Z., Bown M. R., O'Sullivan B., Maclnnes J. M., Allen R. W. K., Mulder M., Blom M., Oever R. V.** 2009, Microfluid Nanofluid, Vol. 6, pp. 763-774.

29. *Chaotic Serpentine Mixer Efficient in the Creeping Flow Regime: From Design Concept to Optimization.* **Kang T. G., Singh M. K., Anderson P. D., Meijer H. E. H.** 2009, Microfluid Nanofluid, Vol. 6, pp. 763-774.

30. *Forced assembly and mixing of melts via planar polymer micro-mixing.* **Moon D., Migler K. B.** 2010, Polymer, Vol. 51, pp. 3147–3155.

31. *Compact mixing using multiple splitting, stretching, and recombining flows.* **Neerincx P. E., Denteneer R. P. J., Peelen S., Meijer H. E. H.** 2011, Macromol. Mater. Eng., Vol. 296, pp. 349–361.

32. *A rapid three-dimensional vortex micromixer utilizing self-rotation effects under low Reynolds number conditions.* **Lin C. H., Tsai C. H., Fu L. M.** 2005, J. Micromech. Microeng., Vol. 15, pp. 935–943.

33. *Understanding and optimizing the SMX static mixer.* **Singh M. K., Anderson P. D., Meijer H. E. H.** 2009, Macromol. Rapid Commun., Vol. 30, pp. 362-376.

34. *An efficient micromixer based on multidirectional vortices due to baffles and channel curvature.* **Wu R., Tsai C.** 2011, Biomicrofluidics, Vol. 5, p. 014103.

35. *Theoretical and experimental characterization of a low-Reynolds number split-and-recombine mixer.* **Hardt S., Pennemann H., Schonfeld F.** 2006, Microfluid Nanofluid, Vol. 2, pp. 237-248.

36. *Induced charge electro osmotic mixer: Obstacle shape optimization.* **Jain M., Yeung A., Nandakumar K.** 2009, Biomicrofluidics, Vol. 3, p. 022413.

37. *Novel index for micromixing characterization and comparative analysis.* **Jain M., Nandakumar K.** 2010, Biomicrofluidics, Vol. 4, p. 031101.

38. *Experimental and theoretical scaling laws for transverse diffusive broadening in two-phase laminar flows in microchannel.* **Ismagilov R. F., Stroock A. D., Kenis P. J. A., Whitesides G., Stone H. A.** 2000, Appl. Phys. Lett., pp. 2376-2378.

39. *Quantitative analysis of molecular interactive in a microfluidic channel: the T-sensor.* **Kamholz A. E., Weigl B. H., Finlayson B. A., Yager P.** 1999, Anal. Chem., pp. 5340-5347.

40. *Molecular diffusive scaling laws in pressure-driven microfluidic channels: deviation from one-dimensional Einstein approximations.* **Kamholz A. E., Yager P.** 2002, Sensors and Actuators, pp. 117-121.

41. *Micro T-mixer as a rapid mixing micromixer.* **Wong S. H., Ward M. C. L., Wharton C. W.** 2004, Sensors and Actuators, Vol. B 100, pp. 359-379.

42. *Simulation of miscible diffusive mixing in microchannels.* **Sullivan S. P., Akpa B. S., Matthews S. M., Fisher A. C., Gladden L. F., Johns M. L.** 2007, Sensors and Actuators, Vol. B 123, pp. 1142-1152.

43. *Modulating passive micromixing in 2-D microfluidic devices via discontinuities in surface energy.* **Swickrath M. J., Burns S. D., Wnek G. E.** 2009, Sensors and Actuators, Vol. B 140, pp. 656-662.

44. *A highly efficient 3D micromixer using soft PDMS bonding.* **Cha J., Kim J., Ryu S. K., Park J., Jeong Y., Park S., Park S., Kim H. C., Chun K.** 2006, J. Micromech. Microeng., Vol. 16, pp. 1778-1782.

45. *Steering of liquid mixing speed in interdigital micro mixers-from very fast to deliberately slow mixing.* **Lob P., Drese K., Hessel V., Hardt S., Hofmann C., Lowe H., Schenk R., Schonfeld F., Werner B.** 2004, Chem. Eng. Technol., Vol. 27, pp. 340-345.

46. *A split and recombination micromixer fabricated in a PDMS three-dimensional structure.* **Lee S. W., Kim D. S., Lee S. S., Kwon T. H.** 2006, J. Micromech. Microeng., Vol. 16, pp. 1067-1072.

47. *Fast mixing by lamination. In: Proceedings.* **Branebjerg J., Gravesen P., Krog J., Nielsen C.** San Diego, CA. : s.n., Febuary 2002. IEEE 9th annual international workshop on micro electro mechanical systems (MEMS'96). pp. 441-446.

48. *Simple quantitative optical method for monitoring the extent of mixing applied to a novel microfluidic mixer.* **Munson M., Yager P.** 63–71, Anal. Chim. Acta, Vol. 507.

49. *A 3D micromixer fabricated with dry film resist.* **Radadia A, Cao L., Jeong H., Shannon M., Mase R. l.** Hyogo, Japan : s.n., 2007. IEEE 20th international conference on micro mechanical systems (MEMS'07). pp. 361-364.

50. *A novel microreactor with 3D rotating flow to boost fluid reaction and mixing of viscous fluids.* **Fang W., Yang J.** 2009, Sensors and Actuators B, Vol. 140, pp. 629–642.

51. *Multivortex micromixing.* **Sudarsan A., Ugaz V.** 2006, Proc. Natl. Acad. Sci., Vol. 103, pp. 7228–7233.

52. *Hydrodynamic focusing on a silicon chip:mixing nanoliters in microseconds.* **Knight J., Vishwanath A., Brody J., Austin R.** 1998, Phys. Rev. Lett., Vol. 80, pp. 3863-3866.

53. *Hydrodynamic focusing for a micromachined flow cytometer.* **Lee G., Hung C., Ke B., Huang G., Hwei B., Lai H.** 2001, J. Fluids Eng., Vol. 123, pp. 672–679.

54. *Hydrodynamic focusing in microchannels under consideration of diffusive dispersion: theories and experiments.* **Wu Z., Nguyen N.** Sensors and Actuators B, Vol. 107, pp. 965–974.

55. *Rapid mixing using two-phase hydraulic focusing in microchannels.* **Wu Z., Nguyen N.** Biomed Microdevices, Vol. 7, pp. 13–20.

56. *Mixing processes in a zigzag microchannel: finite element simulations and optical study.* **Mengeaud V., Josserand J., Girault H.** 2002, Anal. Chem., Vol. 74, pp. 4279–4286.

57. *Helical flows and chaotic mixing in curved micro channels.* **Jiang F., Drese K., Hardt S., Kupper M., Schonfeld F.** 2004, AIChE J., Vol. 50, pp. 2297–2305.

58. *Simulation of helical flows in microchannels.* **Schonfeld S., Hardt S.** 2004, AIChE J., Vol. 50, pp. 771–778.

59. *Topologic mixing on a microfluidic chip.* **Chen J., Meiners J.** 2004, Appl. Phys. Lett., Vol. 84, pp. 2193-2195.

60. *Passive mixing in a three-dimensional serpentine microchannel.* **Liu R. H., Stremler M., Sharp K., Olsen M., Santiago J., Adrian R., Aref H., Beebe D.** 2000, J. Microelectromech. Syst., Vol. 9, pp. 190–197.

61. *Ultrafast microfluidic mixer and freezequenching device.* **Lin Y., Gerfen G., Rousseau D., Yeh S.** 2003, Anal. Chem., Vol. 75, pp. 5381–5386.

62. *Patterning flows using grooved surfaces.* **Stroock A. D., Dertinger S., Whitesides G., Ajdari A.** 2002, Anal. Chem., Vol. 74, pp. 5306–5312.

63. *Investigation of the convective motion through a staggered herringbone micromixer at low Reynolds number flow*. **Hassell D. G., Zimmerman W.** 2006, Chem. Eng. Sci., Vol. 61, pp. 2977–2985.

64. *Chaotic mixing in microchannels.* **Stroock, A. D.** 2002, Science, Vol. 295, pp. 647-651.

65. *An injection micromixer fabricated by improved SU-8 processingfor biochemical microfluidic systems.* **Liu C., Ling Z., Lian K., Goettert J., Hormes J.** 2005, Proc. of SPIE, Vol. 6122.

66. *An integrated liquid mixer/valve.* **Voldman J., Gray M. L., Schmidt M. A.** 2000, J. Microelectromech. Syst, Vol. 9, pp. 295–302.

67. *Design of rapid micromixers using CFD.* **Larsen U. D., Rong W., Telleman P.** Sendai, Japan : s.n., 1999. Proc. Transducers'99, 10th Int. Conf. on Solid-State Sensors and Actuators. pp. 200-203.

68. *Dynamic pattern formation in a vesiclegenerating microfluidic device.* **Thorsen T., Roberts R., Arnold F., Quake S.** 2001, Phys. Rev. Lett., Vol. 86, pp. 4163–4166.

69. *Formation of droplets and bubbles in a microfluidic T-junction – scaling and mechanism of break-up.* **Garstecki P., Fuerstman M., Stone H., Whitesides G.** 2006, Lab Chip, Vol. 6, pp. 437–446.

70. *Droplet microfluidics.* **Teh S., Lin R., Hung L., Lee A.** 2008, Lab Chip, Vol. 8, pp. 198–220.

71. *Microfluidic systems for chemical kinetics that rely on chaotic mixing in droplets.* **Bringer M. R., Gerdts C. J., Song H., Tice J. D., Ismagilov R. F.** 2004, Math. Phys. Eng. Sci., p. 1087.

72. *A fast microfluidic mixer based on acoustically driven sidewall-trapped microbubbles.* **Ahmed D., Mao X., Juluri B., Huang T.** 2009, Microfluid Nanofluid, Vol. 7, pp. 727-731.

73. *High-throughput micromixers based on acoustic streaming induced by surface acoustic wave.* **Luong T., Phan V., Nguyen N.** 2011, Microfluid Nanofluid, Vol. 10, pp. 619-625.

74. *A soft-lithographed chaotic electrokinetic micromixer for efficient chemical reactions in lab-on-chips.* **Campisi M., Accoto D., Damiani F., Dario P.** 2009, J. Micro-Nano Mech., Vol. 5, pp. 69-76.

75. *Electrokinetically driven flow mixing utilizing chaotic electric fields.* **Chen C. K., Cho C. C.** 2008, Microfluid Nanofluid, pp. 785-793.

76. *Mixing enhancement in microfluidic channel with a constriction under periodic electro-osmotic flow*. **Lim C., Lam Y., Yang C.** 2010, Biomicrofluidics, Vol. 4, p. 014101.

77. *A simplified design of the staggered herringbone micromixer for practical applications.* **Du Y., Zhang Z., Yim C., Lin M., Cao X.** 2010, Biomicrofluidics, Vol. 4, p. 024105.

78. *Quantitative characterization of micromixing simulation.* **Zhang Z., Yim C., Lin M., Cao X.** 2008, Biomicrofluidics, Vol. 2, p. 034104.

79. *Thermal mixing of two miscible fluids in a T-shaped microchannel.* **Xu B., Wong T., Nguyen N., Che Z., Chai J.** 2010, Biomicrofluidics, Vol. 4, p. 044102.

80. *A rapid magnetic particle driven micromixer*. **Wang Y., Zhe J., Chung B.T.F., Dutta P.** 2008, Microfluid Nanofluid, Vol. 4, pp. 375-389.

81. *Micromixer based on viscoelastic flow instability at low Reynolds number.* **Lam Y., Gan H., Nguyen N., Lie H.** 2009, Biomicrofluid, Vol. 3, p. 014106.

82. *Application of electrokinetic instability flow for enhanced micromixing in cross-shaped microchannel.* **Huang M. Z., Yang R. J., Tai C. H., Tsai C. H., Fu L. M.** 2006, Biomed. Microdevices, Vol. 8, pp. 309-315.

83. *Physics and application of microfluidic in biology.* **Beebe D. J., Mensing G. A., Walker G. M.** 2002, Annu. Rev. Biomed. Eng., Vol. 4, pp. 261-286.

84. *Lab-on-a-chip for drug development.* **Weigl B, Bardell R, Cabrera.** 2003, Adv. Drug Deliv. Rev., Vol. 55, pp. 349-377.

85. *Experimental Investigation of Split and Recombination Micromixer in Confront with Basic T- and O- type Micromixers.* **Nimafar M., Viktorov V., Martinelli M.** 2012, International Journal of Mechanics and Applications, Vol. 2, pp. 61-69.

86. *Experimental comparative mixing performance of passive micromixers with H-shaped sub-channels.* **Nimafar M., Viktorov V., Martinelli M.** 2012, Chemical Engineering Science, Vol. 76, pp. 37-44.

87. *Design and simulation of passive micromixers based on capillary.* **Zhang Y., Hu and Wu H.** 2012, Microfluid Nanofluid, Vol. 13, pp. 809-818.

88. *Use of electrochemical microsensors for hydrodynamics study in crossing microchannels.* **Huchet F., Havlica J., Legentilhomme P., Montillet A., Comiti J., Tihon J.** 2008, Microfluid Nanofluid, Vol. 5, pp. 55-64.

89. *Analysis of chaos and FRET reaction in split-and-recombine microreactors.* **Chen Y. T., Fang W. F., Liu Y. C.** 2011, Microfluid Nanofluid, Vol. 11, pp. 339-352.

90. *Electrokinetic mixing in microfluidic systems.* **Chang C.C., Yang R. J.** 2007, Microfluid Nanofluid, Vol. 3, pp. 501-525.

91. *Serpantine microfluidic mixer made in LTCC.* **Malecha k., Golonka L., Baldyga J., Jasinska M., Sobieszuk P.** 2009, Sensors and Actuators B, Vol. 143, pp. 400-413.

92. *Improved serpentine laminating micromixer with enhanced local advection.* **Park J.M., Kim D.S., Kang T.G., kwon T.H.** 4, 2008, Microfluidic Nanofluidic, pp. 513-523.

93. *A state-of-the-art Review of Mixing in Microfluidic Mixers.* **Mansur E. A., Mingxing Y. E., Yundong W., Youyuan D.** 16, 2005, Chinese Journal of Chemical Engineering, Vol. 4, pp. 503-516.

94. *Toward numerical prototyping of labs-on-chip: modeling for integrated microfluidic devices.* **D., Erickson.** 1, 2005, Microfluidic Nanofluidic, pp. 301-318.

95. *A numerical design study of chaotic mixing of magnetic particles in a microfluidic bio-separator.* **Zolgharni M., Azimi S. M., Bahmanyar M. R., Balachandran W.** 2007, Microfluidic Nanofluidic, Vol. 3, pp. 677-387.

96. *Interfacial configurations and mixing performances of fluids in staggered curved-channel micromixers.* **Chen J. J., Shie Y. S.** 2012, Microsyst Technol, Vol. 18, pp. 1823-1833.

97. *Experimental investigation of a scaled-up passive micromixer with uneven interdigital inlet and teardrop obstruction elements.* **Cook K. J., Fan Y. F., Hassan I.** 2012, Exp. Fluids, Vol. 52, pp. 1257-1261.

98. *Deign of confluence and bend geometry for rapid mixing in microchannels.* **Aoki A., Fukuda T., Maeda N., Mae K.** 2013, Chemical engineering Journal, Vol. 227, pp. 198-202.

99. *A Review on the Analysis and Experiment of Fluid Flow and Mixing in Micro-Channels.* **Suh Y. K., Jayaraj S., Kang S.** 2007, Journal of Mechanical Science and Technology, Vol. 21, pp. 536-548.

100. *Microfluidic mixing using periodically induced secondary potential in Electroosmotic flow.* **Jeong S., Park J., Kim J. M., Park S.** 2011, Journal of Electrostatics, Vol. 69, pp. 429-434.

101. *Passive micromixers for applications in the microreactor and μTAS fields, Microfluidic Nanofluidic.* **Hardt S., Drese K. S., Hessel V., Schonfeld F.** 2005, Microfluidic Nanofluidic, Vol. 1, pp. 108-118.

102. *Mixing of a split and recombine micromixer with tapered curved microchannels.* **Sheu T. S., Chen S. J., Chen J. J.** 2012, Chemical Engineering science, Vol. 71, pp. 321-332.

103. *Numerical study of the effect on mixing of the position of fluid stream interface in a rectangular microchannel.* **Ansari M. A., Kim K. Y., Kim S. M.** 2010, Microsyst. Technol., Vol. 16, pp. 423-434.

104. *Numerical and experimental investigation on liquid mixing in static micromixers.* **Engler M., Kockmann N., Kiefer T., Woias P.** 2004, Chemical Engineering Journal, Vol. 101, pp. 315-322.

105. *Evaluation of Floor-grooved Micromixers Using Concentration-channel Length Profiles.* **Du T., Zhang Z., Yim C., Lin M., Cao X.** 2010, Micromachines, Vol. 1, pp. 19-33.

106. *Mixing performance of a planar micromixer with circular chambers and crossing constriction channels.* **Alam A., Kim K.** 2013, Sensors and Actuators B: Chemical, Vol. 176, pp. 639-352.

107. *Multiobjective Optimization of a Micromixer with Convergent–Divergent Sinusoidal Walls.* **Afzal A., Kim K. Y.** 2015, Chemical Engineering Communications, Vol. 202, pp. 1324-1334.

108. *Laminar mixing in different interdigital micromixers: II. Numerical simulations.* **Hardt S., Schönfeld F.** 2003, AIChE J., Vol. 49, pp. 578-584.

109. *Combining two orthgonal secondary flows to enhance the mixing in a annular duct.* **Zambaux J. A., Harion J. L., Russeil S., Bouvier P.** 2015, ChemE, Vol. 94, pp. 702-713.

110. *Numerical investigation of mixing performance in microchannel T-junction with wavy structure.* **Solehatia N., Baea J., Sasmitob A. P.** 2014, Computers & Fluids, Vol. 96, pp. 10-19.

111. *Convective mixing and chemical reactions in microchannels with high flow rates.* **Kockmann N., Kiefer T., Engler M., Woias P.** 2006, Sensors and Actuators B: Chemical, Vol. 117, pp. 495-508.

112. *The theory of short-circuiting in continuous-flow mixing vessels in series and the kinetics of chemical reactions in such systems.* **MacMullin R. B., Weber M.** 1935, Trans. Am. Inst. Chem. Eng., Vol. 31, pp. 409-458.

113. *Continuous flow systems: distribution of residence times.* **V., Danckwerts P.** 1953, Chem. Eng. Sci., Vol. 2, pp. 1-13.

114. *Numerical and experimental studies of mixing characteristics in a T-junction microchannel using residence-time distribution.* **Adeosun J. T., Lawal A.** 2009, Chemical Engineering Science, Vol. 64, pp. 2422-2432.

115. *Numerical investigation of the effect of geometrical parameters on the performance of a micro-reactor.* **Kanaris A. G., Mouza A. A.** 2011, Chemical Engineering Science, Vol. 66, pp. 5366-5373.

116. *Residence-time distribution as a measure of mixing in T-junction and multilaminated/elongational flow micromixers.* **Adeosun J. T., Lawal A.** 2010, Chemical Engineering Science, Vol. 65, pp. 1865-1874.

Chapter 6. Basic of Droplet and Bubble

Since the advent of microfluidics approximately two decades ago, there has been a steady increase in the interest and development of tools for fluid flow at the micro-scale (1). Microfluidic can be found in numerous applications, such as emulsification, chemical synthesis, biomedical diagnostics applications, food and drug screening (2) (3). Many food products are based on oil in water emulsions (salad dressings, cream, beverages) or water in oil (butter, margarine) and air foams in fluids (cakes, aerated chocolate, ice cream, soft drinks) (4) (5). Compared to conventional techniques that use reaction vessels, test tubes or microtiter plates, microfluidic technology offers several unique advantages: (i) much less volume of sample or reagents is used, which is practical and reduces costs; (ii) the diagnostic results or the molecular products are obtained in a shorter time, because the high surface-to-volume ratios at the micro-scale lead to shorter heat and mass transfer times; (iii) miniaturization allows for an increase in parallelization and automation (6).

At the micro-length scale, interfacial and viscous effects dominate over bulk forces, and fluid inertia is often negligible. As a consequence of these physical constraints, the characteristic features of multiphase flows in microfluidic environments are unique. Emulsions and foams formation have rich dynamics that are affected by many parameters, including the flow rates of the different fluid phases, their viscosities, densities and interfacial tension, surface chemistry, and device geometry (7) (8).

In years to come, the food processing industry will be increasingly involved in the design of foods for quality, health and pleasure as well as reducing products cost (9). Most processed foods such as frozen products, emulsions, beverages, baked products, etc. are multi-component dispersed systems whose success at the marketplace depends on how a phase (gas, liquid or solid) is distributed within a continuous matrix (10) (11). It is well known that the majority of elements contribute to these transport properties, physical and rheological behavior, texture and sensorial traits of foods are below 100 μm range (12). Improvement on the quality of existing food as well as the creation of new products is to be based on invention at the microscopic and colloidal level. As microfluidic methods offer controlled environments for the production of bubbles and droplets, they have

become established as reliable alternatives to more conventional bulk methods for the generation of mono-dispersed emulsions and foams (13).

Mono-dispersed droplets have been generated via a number of methods in microfluidic devices, including geometry dominated break-up (14) (15), cross-flow shear in T-junction microchannel (16) (17) (18) (19) (20) (21) (22), and hydrodynamic flow-focusing (23) (24) (25). These methods enable formation of dispersions with highly attractive features, particularly the control over the size and narrow distribution of the sizes of individual droplets. With the rapid development of droplet formation techniques in microfluidic devices, several applications for the microfluidic chemical processing based on droplets have been demonstrated, including production of mono-dispersed micro-particles (26) (27) (28) (29), enhancement of mixing (30) (31), crystallization of proteins (32), synthesis of nanoparticles (33) (34), and micro-chemical analysis (35) (36).

There are three major microchannel geometries that are used to generate micron-sized bubbles: T-junction, co-flow and flow-focusing (37). The most studied device for the production of bubbles is the T-junction device (16) (20) (38), where volume and energy content ratio of products can be increased and homogeneity of the sample can also be improved (39). One of the well-known way to produce bubbles is to place the needle through which the gas is injected in a coaxial liquid co-flow, which is proved to substantially reduce the bubble diameter with respect to the case in which the surrounding liquid is quiescent (40) (41) (42) (43). However, even in this case, the diameter of the bubbles formed scale with the needle injection diameter. Bubbles sizes become much less than the injection needle diameter if flow-focusing geometry is employed (44) (45). The key idea that permits such size reduction is that the gas is injected within a highly convergent liquid flow that decreases the diameter of the gas ligament.

6.1 Microdroplet

Microdroplet is a micron size liquid droplet suspend in a second immiscible liquid. Generally an emulsion contains liquid droplet. An emulsion is a mixture of two immiscible liquids, where one liquid is dispersed in the form of small drops in another liquid that forms a continuous phase (46). Common types of emulsions include oil-in-water (O/W) and water in oil (W/O). Emulsions typically contain droplet diameters ranging from hundreds of nanometers to tens of micrometers. The majority of microfluidic methods produce droplet diameters ranging from a few micrometers to hundreds of micrometers in a uniform, evenly spaced, continuous stream (8).

6.2 Microdroplet Production

The power of droplet-based microfluidic systems lies in the formation of uniform droplets and particles, thus fine control over the size, shape, and mono-dispersity of droplets is of the utmost importance (47). Although the same basic principles and materials are used, a variety of techniques have been developed for droplet generation (48). Microfluidic methods for forming droplets can be either passive or active. Most methods are passive, relying on the flow field to deform the interface and promote the natural growth of interfacial instabilities. These methods avoid moving parts and explicit external actuation. Passive methods can be grouped into three categories, characterized by the nature of the flow field near pinch off: (i) breakup in co-flowing streams, (ii) breakup in cross-flowing streams and (iii) breakup in elongational or stretching dominated flows (8). The description of some devices used for the droplet production is given below.

6.2.1 T-junction Device

In T-junction configuration, the inlet channel containing the dispersed phase perpendicularly intersects the main channel which contains the continuous phase as shown in Figure 6.1. The two phases form an interface at the junction, and as fluid flow continues, the tip of the dispersed phase enters the main channel. The shear forces generated by the continuous phase and the subsequent pressure gradient cause the head of the dispersed phase to elongate into the main channel until the neck of the dispersed phase thins and eventually breaks the stream into a droplet (47). This type of geometry was first demonstrated by Thorsen et al. (16), who produced mono-dispersed droplets with pressure controlled laminar flow in micro-channels. The sizes of the droplets can be changed by altering the fluid flow rates, the channel widths, or by changing the relative viscosity between the two phases. T-Junctions are not limited to single inlets as more complicated schemes have been used for performing chemical reactions (31) and forming gas plugs (49) and droplets of alternating composition (50).

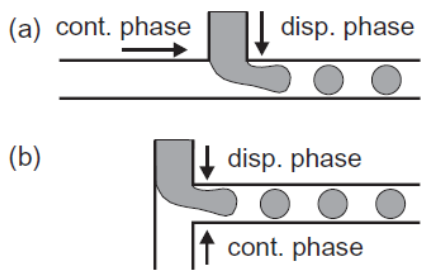

Figure 6.1 Schematic of various T-junction geometries. (a) 'regular T-. (b) 'Head on' geometry (2)

6.2.2 Flow-focusing Device

The flow-focusing (FF) geometry was first proposed by Anna et al. (23) and Dreyfus et al. (51). As demonstrated in Figure 6.2, it consists of three inlet channels converging into a main channel via a narrow orifice. The dispersed phase, contained in the middle channel, is squeezed by continuous phase flows from two opposing side channels. Both phases pass through the small orifice that is located downstream of the three channels. Finally, the stream of the dispersed phase becomes narrow and breaks into droplets (6). The sizes of the droplets can decrease by increasing flow rates of the continuous phase. Additionally, an increase in oil flow rates also increases the frequency of droplet generation (47). Many variations of the basic flow focusing device (FFD) geometry have recently been developed to improve the control over the size and size distribution of the droplets (6). Since recently, these developments can be assisted by numerical (Lattice Boltzmann) simulations, which have seen their first application to flow-focusing (52) and cross-flow geometries (53).

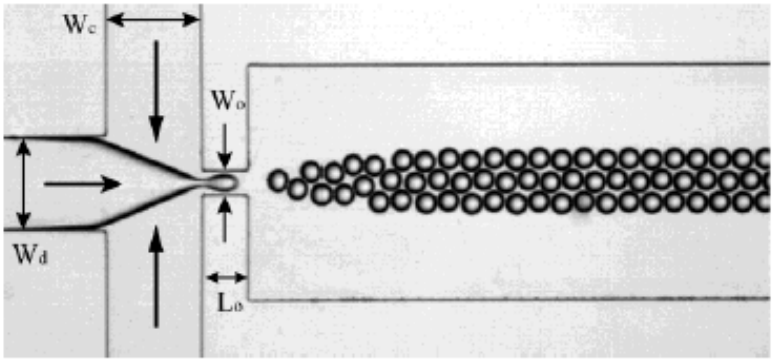

Figure 6.2 Droplet formations in flow focusing device. The widths of the inlets of dispersed phase and continuous phase, as well as the orifice are indicated as W_d, W_c and W_o ($W_d = W_c = 200$ µm; $W_o = 50$ µm). The length of orifice is indicated as L_o (100 µm) (6)

6.2.3 Co-flow Device

Co-flow microfluidic devices consist of coaxial assemblies of capillaries on glass slides. One of the inherent advantages of these devices is that their wettability can be easily and precisely controlled by a surface reaction with an appropriate surface modifier. Also, these devices offer the distinct capability of creating truly three dimensional flows, which is critical for specific applications. The co-flow technique was first developed outside of a microfluidic device to generate highly uniform gas bubbles in a liquid (54). The concept of droplet production in co-flowing streams was first applied to liquid/liquid systems by Umbanhowar et al. (55). Shah et al. (46) discussed a circular glass capillary with an outer diameter of 1–2 mm where coaxial alignment of the two capillaries is

ensured by choosing the capillaries such that the outer diameter of the circular capillary is the same as the inner dimensions of the square capillary. One fluid flows inside the circular capillary while the other fluid flows through the square capillary in the same direction, resulting in a coaxial flow of the two fluids (Figure 6.3 a) (46). When the fluids flow at low rates, individual mono-dispersed drops are formed periodically at the tip of the capillary orifice, in a process termed dripping (Figure 6.3 b). If we increase the flow rate of either fluid beyond a certain critical limit, the result is a jet, a long stream of the inner fluid with drops forming downstream (Figure 6.3 c).

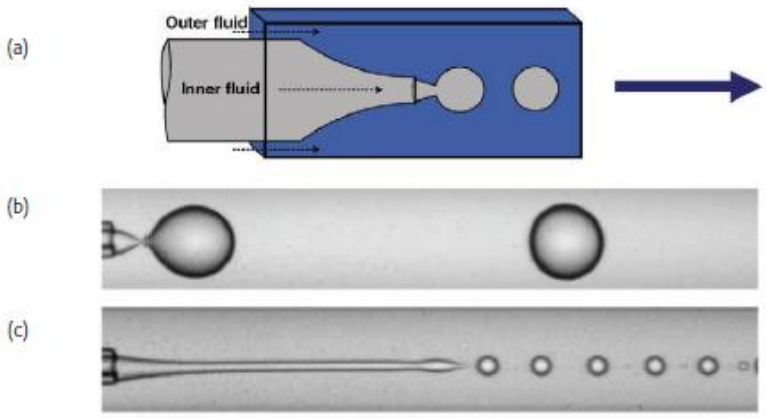

Figure 6.3 Single emulsions in a co-flow microfluidic device. (a) Schematic of a co-flow microcapillary device for making droplets. Arrows indicate the flow direction of fluids and drops. (b) Image of drop formation at low flow rates (dripping regime). (c) Image of a narrowing jet generated by increasing the flow rate of the continuous fluid above a threshold value while keeping the flow rate of the dispersed phase constant (46)

Castro-Hernandez et al. (56) studied in detail the process of drop formation from long, widening jets, in microfluidic co-flowing devices. Their experimental device was made of two coaxially aligned capillary tubes, as shown in Figure 6.4. The inner capillary tube was cylindrical, with a tip tapered to an inner diameter D_i that is varied between 40μm and 60μm, and an outer diameter of approximately 80μm. By changing the values of the control parameters, which include inner fluid and outer-fluid viscosities and flow rates, the droplet size can be controlled in desire range; it also extended the criterion for jetting to occur as a function of the Reynolds number of the inner fluid.

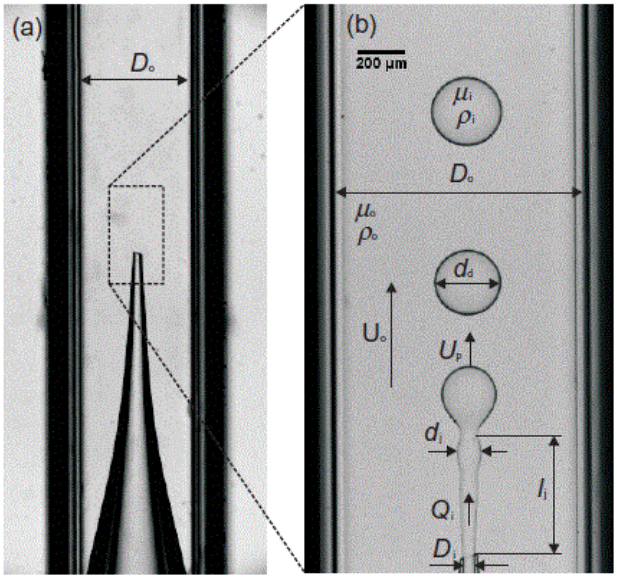

Figure 6.4 Close up view of the tapered portion of the injection tube. Note that the untapered portion adjusts to the inner side of the outer squared capillary tube. (b) Co-flowing device operated in the widening regime, characterized by a long liquid jet growing in diameter downstream of the injection tube (56)

6.3 Microbubble

Kurup and Naik (57) defined microbubble as small spherical bubbles comprising of gas, remain distinct from each other having size range micrometer usually 1‑100 µm. Tabeiet and others (58) defined microbubble as an extremely small bubbles usually less than 100 µm in diameter that can be uniformly distributed in liquid. Microbubble is defined as an extremely small bubble, usually a few hundred micrometers in diameter, that can uniformly suspended in liquid such as blood. It is seen that researchers have not yet reached conformity on the definition of microbubbles (59). Bjerknes et al. (60) gave a brief description about the characterization of microbubbles.

Microbubbles have three components and a schematic of a bubble with its different components as shown in Figure 6.5.

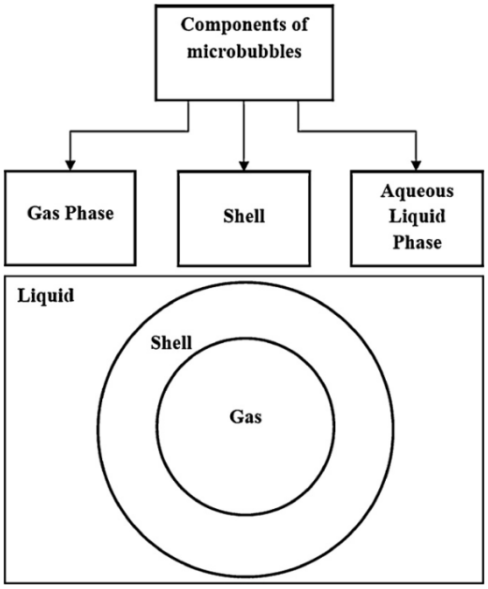

Figure 6.5 Component of microbubbles (57)

6.4 Microbubble Production

Microbubbles can be generated by numbers of ways. Researchers had made several efforts to develop a generator which can produce microbubbles with a minimal power requirement (59). Conventional methods to incorporate bubbles into a liquid or viscoelastic medium include: (i) nucleation of gas bubbles in a liquid which is supersaturated; (ii) shaking or beating the liquid; (iii) generating a gas by fermentation or chemical reaction; (iv) blowing gas through a thin nozzle or single orifice; and (v) by sparging or blowing gas through a porous plate. Novel methods to incorporate bubbles to foods include: (i) microdevices; (ii) membrane; (iii) electrochemical, and (iv) ultrasound.

6.4.1 Microdevices

The application of micro-machining techniques in nano-technology has prompted the use of microfluidic devices (MFDs). MFDs are process elements that deal with small amounts of fluids (10^{-6} - 10^{-9} L) that flow in channels where at least one characteristic dimension on the order of 10 - 100 μm (61). They have the advantage of precise fabrication and replication, portability, small volume and short reaction times (62). The hydrodynamics on the micron scale of MFDs involves significant effects of interfacial tension, rheology and laminar flow, thus allowing a better analytical and reactive performance (14). Generally MFDs are divided in to two main categories, (i) Flow focusing technique and (ii) Microchannel technique.

6.4.1.1 Flow-focusing

Flow-focusing is one of the low power consuming methods to generate the microbubbles. In this method, liquid and gas are inserted into a compartment of the generator through small needles. Gas-liquid flow rates are controlled by programmable syringe pumps. At the chamber exit, droplets are formed and continued over distance from tens of micron to millimeters. Because of capillary instability these droplets breaks into mono-dispersed microbubbles, which can be collected in container. Ganan-Calvo and Gordillo (44) developed flow-focusing device to generated mono-dispersed microbubbles.

Skurtys et al. (63) investigated air in gelatin solutions in a 2.75 mm vertical tube coupled to a microfluidic device as shown in Figure 6.6. The device has two connection chambers (D_L = 1 mm) and a gas tube (D_g) of diameter 500 µm. Two different orifice diameters (D_o) were used: 250 and 500 µm. Air and gelatine solutions (1%, 3% and 5% w/w) were mixed in the microfluidic device to produce steady flows of microbubbles by controlling liquid and gas volumetric flow rates. They found that, gas and liquid flow rates have more effect than tube diameter, orifice aspect ratio and orifice to tube diameter ratio on the various effects such as the transition from bubbly flow to a polyhedral foam, as well as the size of the foam cells.

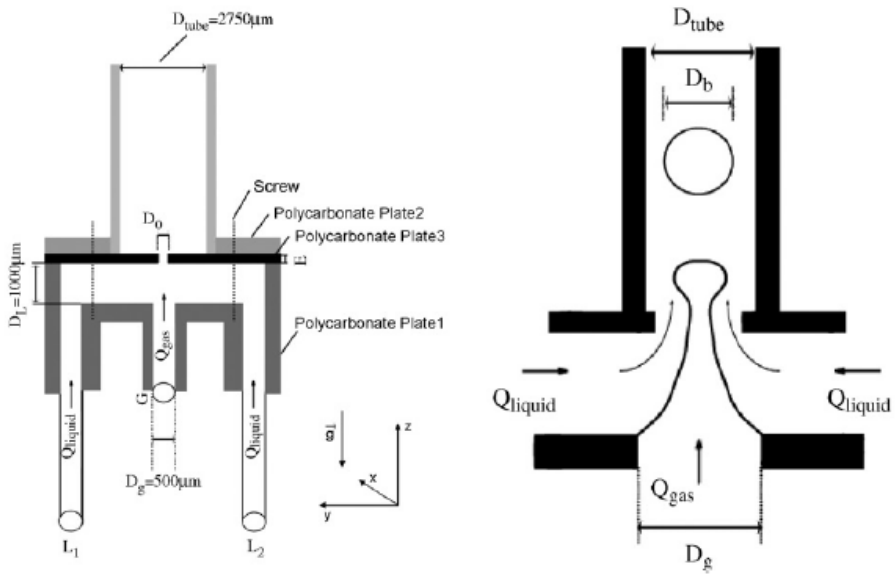

(a) (b)

Figure 6.6 Schematic of a flow focusing device (a) detail of the device, (b) diagram showing the air-liquid flow patterns at the entrance of glass tube (63)

6.4.1.2 Microchannel

The operational principle of microchannel (MC) devices is to drive the disperse-phase fluids to pass through a microchannel structure which has a designed geometry. In this method mono-dispersed microbubble is produced by using microchannels. Yasuno et al. (64) generated mono-dispersed microbubble by microchannel technique as shown in Figure 6.7 . The average size of microbubble they produced ranged from 33.6 to 51.1 µm. The microchannel module was filed with continuous liquid phase and then dispersed gas phase was passed through microchannel. Mono-dispersed microbubbles were formed from the microchannel. MC is a promising technology to enhance the quality of biphasic food products, such as emulsions and foams, since these devices can generate uniform droplets or bubbles in liquids of micro and nano sizes.

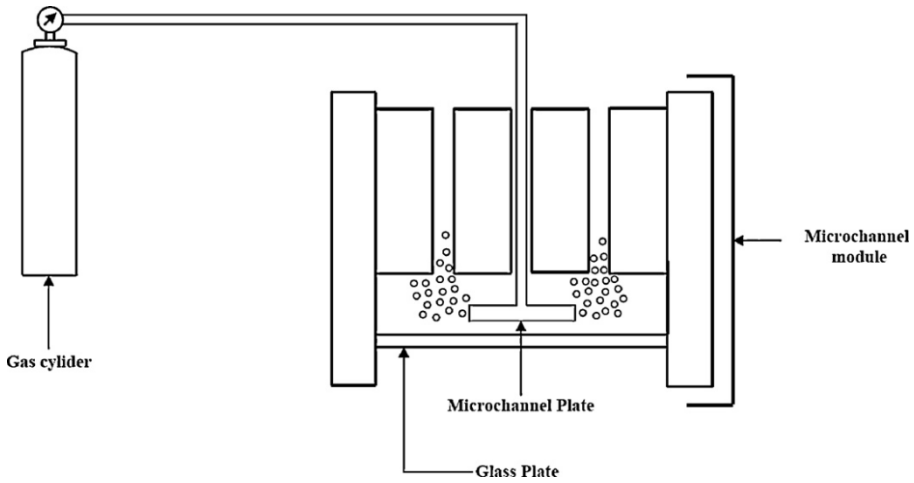

Figure 6.7 Microchannel technique for microbubbles production (65)

6.4.2 Membrane

Membranes have been used to incorporate air bubbles into different fluids (surfactant and protein solutions). Membrane processes use an applied pressure to force the gaseous phase through the membrane into the continuous liquid phase as shown in Figure 6.8 (66) (67). Although many types of membranes (e.g., ceramic, metallic and polymeric) could be used to disperse gases, Shirasu Porous Glass (SPG) membranes are preferred because of their homogeneity of pore structure and high-mechanical strength (68). Surface properties of membranes (hydrophilic/ hydrophobic surface) influence particle characteristics for liquid/liquid dispersions. It is essential that the membrane surface is wetted by the continuous phase (69).

In membrane processing, bubble diameter increases with both gas flow rate and pore size (70). The porosity of the membrane surface is an important parameter because it determines the distance

between two adjacent pores. This distance is critical to ensure that two adjacent bubbles do not come sufficiently close to coalesce (66).

The main limitation of the membrane process is a low dispersed phase flux through the membrane associated with mono-dispersed bubbles. However, membrane systems are particularly suitable for large scale production because they are easy to scale-up, by adding more membranes to a module (66).

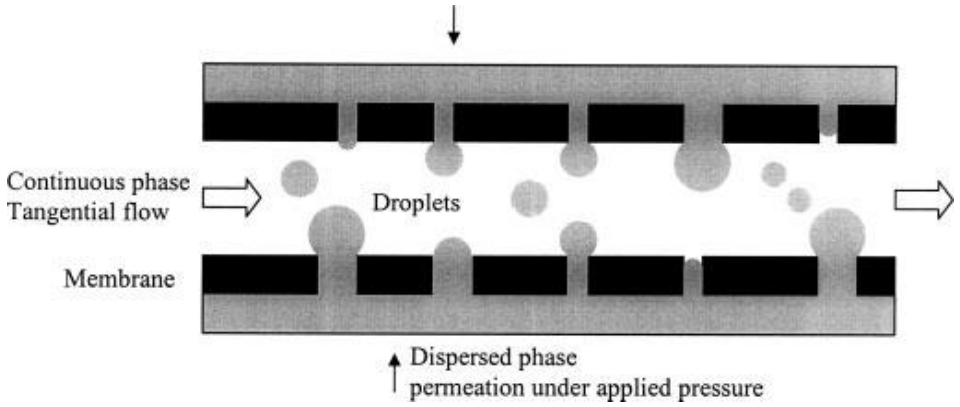

Figure 6.8 Schematic diagram of the membrane emulsification process (66)

6.4.3 Electrochemical

Gas bubbles generated by electrochemical reactions have attracted research interest in many disciplines. Since electrochemical reactions occur primarily in aqueous solutions, gases like hydrogen and oxygen are usually generated in the form of bubbles at the surface of electrodes as shown in Figure 6.9 (65) (71). Gases detach from these surfaces as soon as the buoyancy force overcomes the surface tension effects holding the bubble in place. Electrolysis can generate small bubbles in the order of micro or nanometers (72) using tapping mode AFM demonstrated that the formation of bubbles at the surface of electrodes is a sequential process of formation, growth and coalescence of nanobubbles, followed by the release in the form of microbubbles.

Although electrolytic bubble generators may prove practical at laboratory scale, they may not be viable at production levels due to high cost, low energy efficiency, etc. Further development is needed before such devices become practical for large scale applications requiring formation of a cloud of bubbles (73).

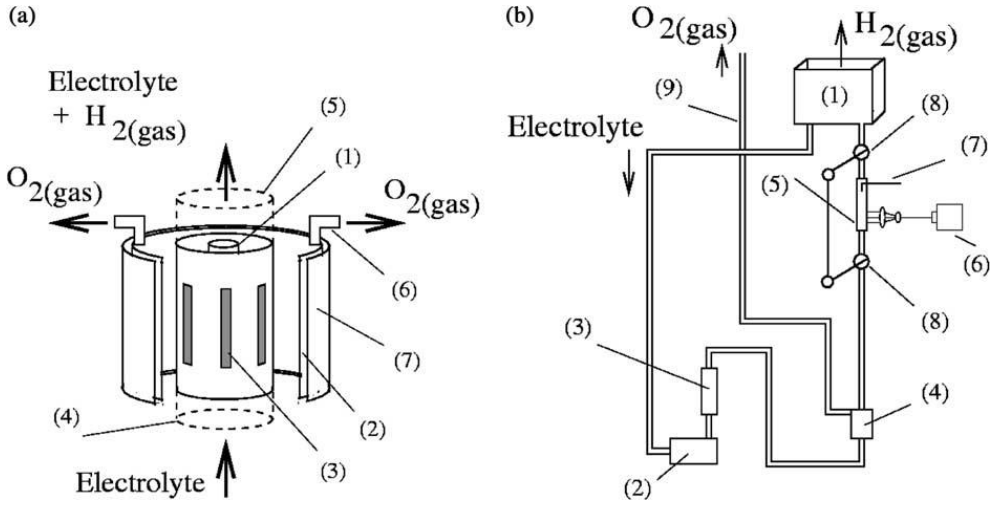

Figure 6.9 An electrochemical bubble appliance; (a) EBBA and (b) Phi50 experiment rig (65)

6.4.4 Ultrasound

Another way of creating microbubbles is acoustic cavitation that implies the formation, growth, and implosive collapse of microscopic bubbles in liquids subjected to high-intensity ultrasound (generally between 20 and100 kHz) (74). Depending on the liquid and conditions used, these bubbles may be on the order of nanometers or micrometers in diameter (75). The application of high-intensity ultrasound cause changes in proteins that may be used advantageously in bubble formation. Ultrasonication increased the surface activity of proteins thus lowering the surface tension of bovine serum albumin solutions and increasing the rate of protein adsorption at the air water interface (76), which concluded that the magnitude of the structural and functional changes induced in proteins could be controlled by varying sonication time and highlighted that potential future applications may include controlled alterations of lipid and gas interfaces in emulsions, foams and gels (5).

One problem using ultrasound is that the collapse of bubbles in a multi-bubble cavitation field produces hot spots (effective local temperatures of ≈ 5000 ºC have been reported) and pressures of ≈ 1000 atm (74) (77), phenomena that may affect thermolabile and pressure-sensitive food components. Also, as a result of cavitation of microbubbles, free radicals may be formed which can promote undesirable chemical reactions (77).

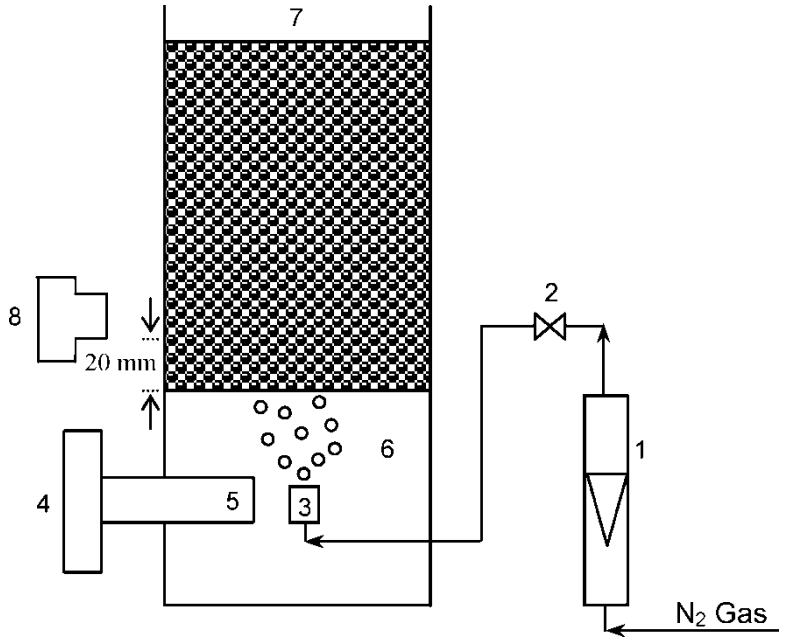

Figure 6.10 Foam generation setup: (1) rotameter; (2) control valve; (3) gas sparger; (4) sonicator; (5) ultrasound probe; (6) surfactant solution; (7) foam; (8) camera (75)

6.5 Characteristics Parameters

The behavior of dispersed phases, either gas–liquid (foams) or liquid–liquid (emulsions), common in many macroscopic food systems is relatively well understood (78). At levels below the micrometer scale, some effects negligible at the macroscopic level become important; for example, those related to surface tension, energy dissipation and fluidic resistance (79). Moreover, different from the macro-scale, a special attention must be paid to the wetting phenomena of the fluid on the substrate. But the most important problem is not 'macro' vs. 'micro' but rather that of the relative importance of various effects, and the way to address it is by using dimensionless numbers (9). Some of the characteristics dimensionless numbers important in microfluidic is mentioned below.

6.5.1 Capillary Number

The Capillary number (*Ca*) plays an important role in the characterization of multi-phase flow. It compares viscous effects to surface tension effects acting across an interface. It is defined as:

$$Ca = \frac{\mu v}{\sigma} \qquad 6.1$$

where μ is the viscosity of the continuous phase, v is the velocity of the continuous phase, and σ is the interfacial tension between the continuous and dispersed phases. Above a certain critical Capillary number, droplet break off occurs. It is important to note that the critical capillary number

is system dependent as different values have been reported by various groups using different geometries (47). To realize this number, it is important to consider the relative viscosity between the discrete and continuous phases. Selection of a more viscous continuous phase will facilitate formation of droplets. For the formation of water-in-oil (W/O) emulsions, the continuous phase commonly consists of oils or water-immiscible organic solvents, which tends to be naturally more viscous than water. In the case of oil-in-water (O/W) emulsions, the addition of viscous water-miscible fluids such as glycerol into the aqueous continuous phase improves shearing of the more viscous oily discrete phase.

6.5.2 Bond Number

The Bond number quantifies the relative importance of the gravity and the interfacial tension to the interface between the two immiscible liquids. It is defined as:

$$Bo = \frac{\Delta \rho g L^2}{\sigma} \tag{6.2}$$

where L is a representative length scale (e.g., the radius of a capillary tube). Generally, in a microfluidic device, the gravitational effects are small compared to those caused by the surface tension, i.e., for an air bubble of characteristic length 100 μm in water: $Bo \sim 10^{-4}$. In a liquid–liquid system, *Bo* will be even lower because the density difference is smaller.

6.5.3 Weber Number

Another important dimensionless parameter is the Weber number or droplet Weber number:

$$We = \frac{\rho L v^2}{\sigma} \tag{6.3}$$

We gives the relative importance of the fluid's inertia compared to its surface tension. The quantity is useful in analyzing the formation of droplets and bubbles. Although the length scales involved are small, the dependence on the velocity can give large *We*, as in the axisymmetric flow focusing bubble generator where $We \sim 400$ (44).

6.6 Liquid Properties

6.6.1 Viscosity

The viscosities of dispersed and continuous phases have important effect on the performance of microchannel emulsification processes. The average droplet diameter of W/O emulsions was reported to increase with increasing continuous phase viscosity (80) and for O/W emulsions, the average droplet diameter was reported to decrease with increasing dispersed phase viscosity (81). In general, the droplet size scales with the viscosity ratio; at high viscosity ratio, the droplet size is constant, and at low viscosity ratio, the droplet size increases (see Figure 6.11). This can be interpreted as follows: as long as the continuous phase can flow onto the terrace freely (compared to the to-be-dispersed phase flow), the neck will break rapidly, and the droplet size will not be influenced. If the continuous phase is very viscous, this will prevent the neck from collapsing rapidly; keep the droplet connected to the feed channel for a longer time, and lead to larger droplets (3).

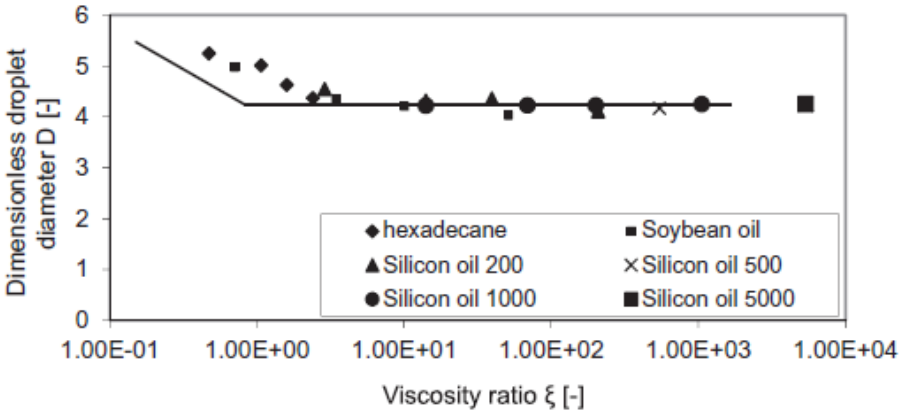

Figure 6.11 Effect of viscosity ratio (gd/gc) on dimensionless droplet diameter D (3)

6.6.2 Interfacial Tension and Surfactant

Surfactants play two important roles in the emulsification process; firstly, they lower the interfacial tension and stabilize the droplet after formation, i.e. prevent coalescence and/or aggregation of emulsions. As a side effect, surfactants may influence the wettability of the emulsification device, therewith indirectly influencing local pressures, and through this, the droplet size. While in classic emulsification methods a low interfacial tension facilitates droplet formation, in microchannel emulsification, this is not the case. At high interfacial tension, the pressure differences between the feed channel and droplet are higher (82). At low interfacial tension, the droplet needs to become

bigger to result in a similar pressure difference. In general, it is expected that for microchannels the droplet formation process is thus slow that the surface will be saturated, i.e. at equilibrium interfacial tension (83).

Surfactants are characterized by several physico-chemical constants: (i) the partition co-efficient, which measures the relative bulk and surface concentrations at equilibrium, as well as (ii) their adsorption and desorption rates on the interface, which measure the chemical kinetics. Finally, any change in the shape of a drop will lead to local contraction or expansion of the interface, which lead to an increase or a decrease, respectively, of surface concentration. All of the above mechanisms can lead to variations of interfacial tension along the drop surface, which will couple back with the drop formation and motion, in addition to influencing droplet fusion. Since different surfactant molecules have different characteristics, changing surfactants can have a major impact in drop behavior (7).

6.7 Summary and Motivation

Droplets, particles, bubbles and capsules sized in the range of micro- and nano-meters are commonly used for delivery of functional or active components in a wide variety of products or as construction elements for more complex structures. Droplets in emulsions are most common structure in pharmaceutical, food and cosmetic products for controlled delivery of drug or nutrition for the amount and pattern desired. Advantages of these microfluidic techniques include the generation of uniform droplets, the precise control of droplet size and shape. Introducing a gas phase into a food matrix not only affects its texture and firmness making the product lighter, but also changes the appearance, color and mouth-feel. Although the final continuous matrix of an aerated food may be liquid (e.g., beer foam), viscoelastic (e.g., marshmallows) or solid (e.g., meringue) bubbles are initially dispersed in the bulk of a liquid solution or a viscous dispersion.

The manufacture of droplets and bubbles involves a bulk liquid phase breaking up and being stabilized in another immiscible liquid phase. Conventional methods of emulsification create droplets through vigorous shear forces exerted through either strong turbulence driven by high speed/pressure or cavity generated by ultrasounds. The use of microfluidic technology for the generation of accurately produced droplets and bubbles has been increasing in recent times and

various microfluidic geometries are used, for example, T-shaped devices, co-flow, and flow-focusing geometries.

Microfluidic has a significant role to play in future progress in the design, preparation and characteristics of food micro-structure: microfluidic-based methods allow for the production of very well-defined droplet based system such as particles and self-assembly vesicles, as well as more complex dispersion such as emulsion and foams which will be applicable in food industries.

Reported results of experimental and numerical studies have enhanced the knowledge and understanding of the dynamics of forming disperses droplets using various immiscible liquids in different micro-devices. The challenge of microfluidic systems lies in the formation of uniform droplets, particles and bubbles; fine control over the size, shape, and poly-dispersity are of the utmost importance. Some of the other limitations related to the production of droplets and bubbles are difficult generation processes, instability over longer period of time; moreover, those devices are not easy to clean and maintain. Thus, a comprehensive investigation needs to be conducted to characterize the droplet and bubble formation, size and frequency distribution in newly developed micro-devices.

6.8 Objectives

This research aims to perform experimental analysis for enhancing the current understanding of forming dispersed droplets and bubbles in various flow regimes, based on the use of new T and H devices using different immiscible liquids. The specific objectives of this research are:

- ✓ To design and develop new micro-devices.
- ✓ To develop innovative process strategies for the production of disperse micro-system, allowing to specially controlling and tuning their shape and homogeneity.
- ✓ Creating stable micro-droplets and micro-bubbles with new properties, especially the number and size distribution.
- ✓ To produce smaller size droplets (W/O) and bubbles (A/O) with low energy.
- ✓ To analyze different droplet and bubble breakup region at different Capillary numbers.

Chapter 7. Design and Development of Micro-devices

One of the most important factors influences the size and shape of the droplet and bubble is the geometrical configuration of micro-devices. In this research two new T-junction devices with modified inputs and two new H devices on the based on split and recombine (SAR) principle were developed for the production of droplets and bubbles. The detail geometrical configuration and fabrication process of these devices is described in this chapter.

7.1 T-1 and T-2 Devices

Conventional T-junction has two inputs and one output. Two new micro-devices named, "T-1" and "T-2" with three inputs and one output were designed as shown in Figure 7.1. The two main inputs (A and B) are 0.8 mm in diameter and the third input (C) is 0.4 mm in diameter. In case of T-1 device, width of the main rectangular channel is 0.8 mm until it reaches the middle of the junction between inputs A and B (see Figure 7.1 a); after that point the width becomes 0.4 mm, in order to exerts more stress on the rest of the microchannel. T-2 devices channel with is always 0.8 mm but there is a "V" cut at the middle of the junction between inputs A and B. In both cases, a tank is added at the output of rectangular channel to collect the products.

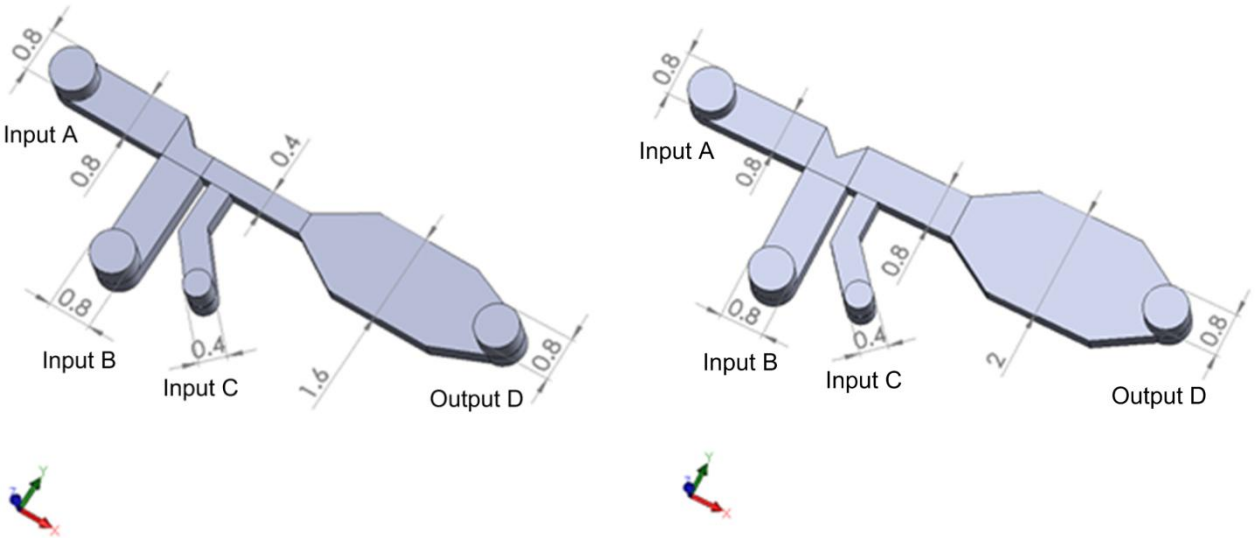

Figure 7.1 Design of T-1 (left) and T-2 (right) devices (all dimensions are in mm)

7.2 H-1 and H-2 Devices

Two new H devices were designed on basics of the work presented by Nimafar et al. (84). In fact these devise are made of a T-junction connected with an H-shape module as shown in Figure 7.2. The H-shape makes it possible to move part of the flow near the wall, in the central zone of the channel along the axial direction and vice versa. H-1 device has one H element and H-2 device has three H elements connected in series. Both devices have two inputs (A and B) and one output (C). The diameter of input and output are 0.4 mm and 0.8 mm, respectively. The width of the rectangular connector is 0.8 mm and a tank is connected at the end of the channel.

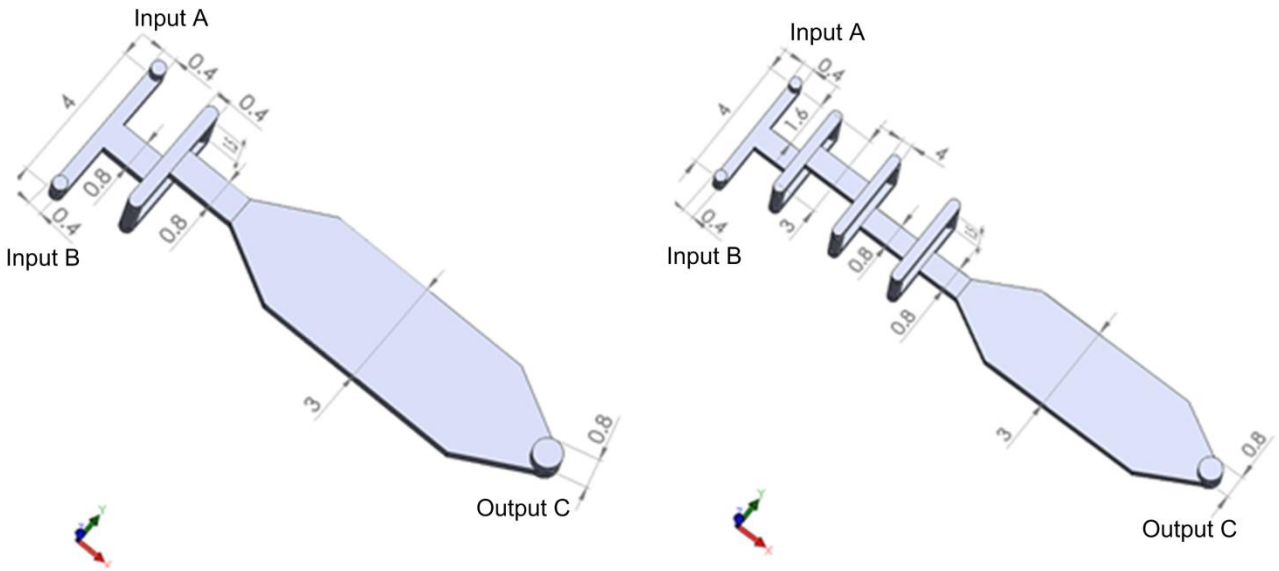

(a) (b)

Figure 7.2 Design of (a) H-1 and (b) H-2 devices (all dimensions are in mm)

7.3 Fabrication of Micro-devices

All prototypes were micro-milled in polycarbonate by a computer numerical control (CNC) Milling and Engraving Machine P20S, KUHLMANN (Germany) at I.T.D sas di Borgna Daniela e Borgna Eugenio &C. (Turin, Italy). The prototypes were made up by overlapping and then clamping a central lamina and one/two covers, one of them provided by two entrances and one exit port as shown in Figure 7.3. The dimensions of prototypes were verified by a profilometer and a maximum error of 1% was found.

(a) T-1 device

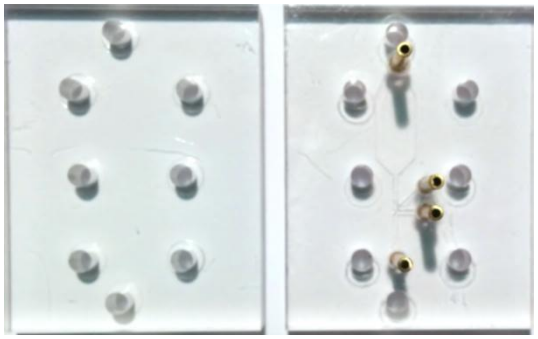

(b) T-2 dvice

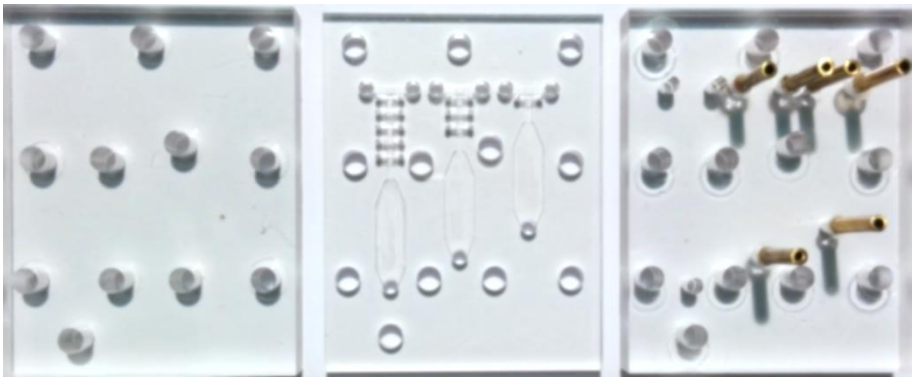

(c) H device

Figure 7.3 Prototypes of micro-devices

Chapter 8. Experimental Technique: Droplet and Bubble

This chapter details all the experimentation techniques used for the production of bubbles and droplets. The procedures can be easily performed in any research laboratory. Flow experiments were carried out using several standard syringe pumps, a compressed air cylinder and test were captured by high speed camera. ImajeJ software was used to analyze the captured images.

8.1 Experimental Equipment

The list of experimental equipment used for this investigation is given below.

1. Injection Syringe
2. Syringe Pump
3. High speed camera
4. Microlens
5. Fluids

These devices and materials are explained and shown separately in this section.

8.1.1 Injection Syringe

Injection glass syringes (20.0 ml) from Tomopal Inc. (Sacramento, USA) were used for the experiments is shown in Figure 8.1.

Figure 8.1 Glass Syringe (20.0 ml)

8.1.2 Syringe Pump

The syringe pumps used in this study is KDS 100 series and KDS 120 series as shown in Figure 8.2.

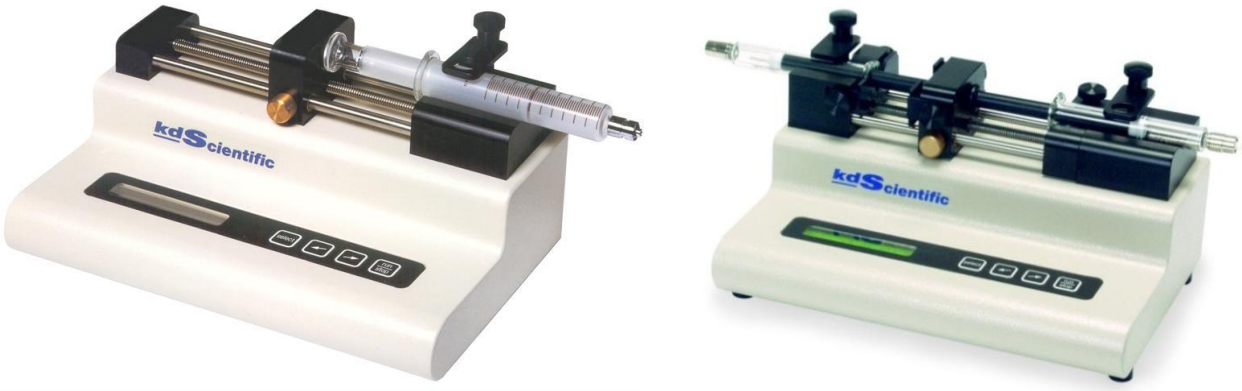

(a) KDS 100 (b) KDS 120

Figure 8.2 Syringe pumps

The flow rate range for this instrument is from 0.1 µl/hr (10µl syringe) to 506 ml/hr (60 ml syringe) with errors less than 1%.

8.1.3 High Speed Camera

NanoSense KMIII CMOS high speed camera was used for capturing the experiment tests (Figure 8.3). The CMOS high speed camera was bought form DANTEC Dynamics, Denmark.

Figure 8.3 NanoSense KMIII CMOS high speed camera

Features of the NanoSense KMIII CMOS:

- Latest CMOS technology
- Unprecedented image quality
- Lower noise (1.7 e^-) than any CCD camera

- High QE and dynamic range
- High resolution (1280×1024 px)
- High frame rate 1KHz

8.1.4 Microlens

To magnify the images of the devices during the experiment Nikon micro Nikkor 105mm lens was used (Figure 8.4).

Figure 8.4 Nikon FX AF MICRO-NIKKOR lens (105 mm)

Features of Nikon micro-lens:

- F Mount Lens/FX Format
- Aperture Range: f/2.8 to 32
- 1:1 Magnification Ratio; Macro Close-Ups
- One Extra-Low Dispersion Glass Element
- Nano Crystal & Super Integrated Coating
- Silent Wave Motor AF System
- Nikon VR Image Stabilization

8.1.5 Fluids

Three immiscible fluids were used in this experimental work. Distilled water and air were used as dispersed phases and silicone oil was used as continuous phase. No surfactant was used in the continuous or dispersed phase. The fluid properties are given in Table 8.1.

Table 8.1 Properties of fluids

Name	Density (Kg/m^3)	Viscosity (Pa s)	Interfacial tension (N/m)
Water	1000	1.0×10^{-3}	Water-oil ≈ 0.035
Air	1.184	1.98×10^{-5}	Air-oil ≈ 0.08
Silicone oil	950	4.8×10^{-2}	Oil-water ≈ 0.035

8.2 Experimental Setup

The experimental system in this present investigation consisted of three major components: (i) fluids, (ii) a test section and (iii) a visualization system. In case of droplet/bubble production, two different liquids named continuous phase and disperse phase were employed. Both the phases were discharged by syringe pumps into the inputs of prototype. To observe the droplet/bubble formation inside the main channel and tank, a high-speed CMOS camera (NanoSense KMIII), microscopic lens (Nikon FX AF) and light were installed above the main microchannel of the test section. Recording rate of 100 fps was used for visualization study, which was sufficient to record the droplet/bubble formation processes. All the experiments were conducted at room temperature. Two experimental setups are used in this work.

- Positive pressure setup: Type-1
- Negative pressure setup: Type-2

8.2.1 Positive Pressure Setup

Figure 8.5 (a) shows the schematic of the experimental flow visualization apparatus used to investigate droplet dispersion in the positive pressure setup (type-1). Inputs of the prototype are connected to the syringe pumps which contain water and silicone oil. The syringe pumps work in the forward/positive direction, so positive pressure is used for the production of droplet. In case of bubble production, one of the inputs is connected to the compressed air cylinder and compressed air was regulated by a valve as shown in Figure 8.5 (b).

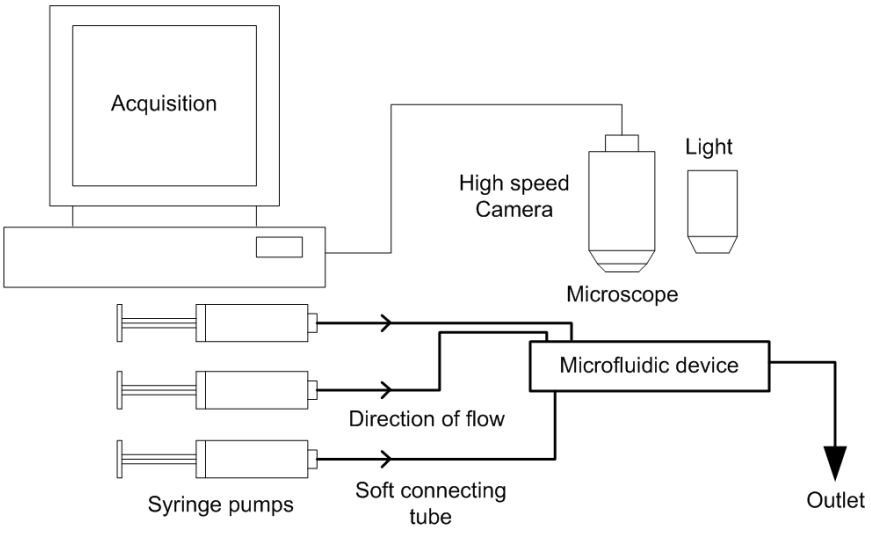

(a) Droplet production configuration

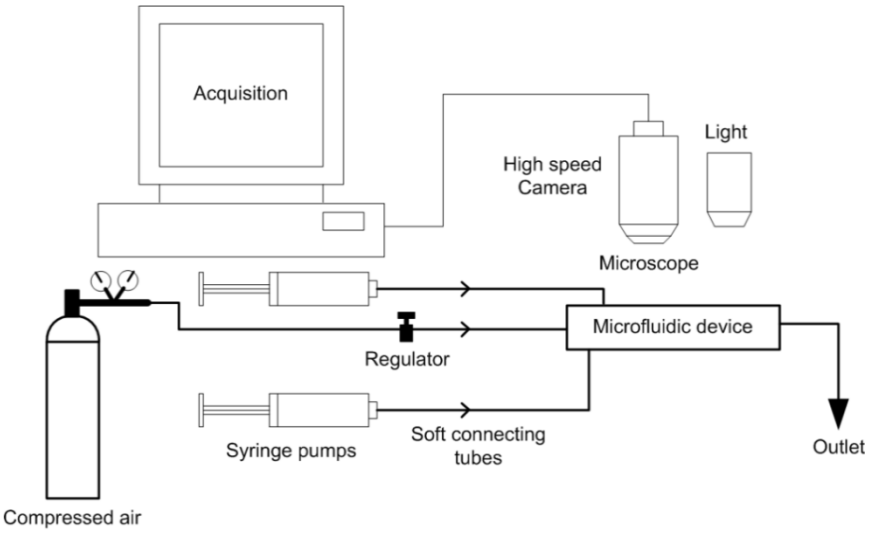

(b) Bubble production configutration

Figure 8.5 Schematic of the positive pressure experimental test: Type-1

8.2.2 Negative Pressure Setup

Figure 8.6 shows the schematic diagram of the negative experimental setup (type-2) for the production of bubble. One or two inputs, depending on the prototype, are connected to the silicone oil reservoir and one input is open to the atmosphere with a regulator. The syringe pump is connected to output of the device which works in the reverse/negative direction, so the negative pressure acts as the working force.

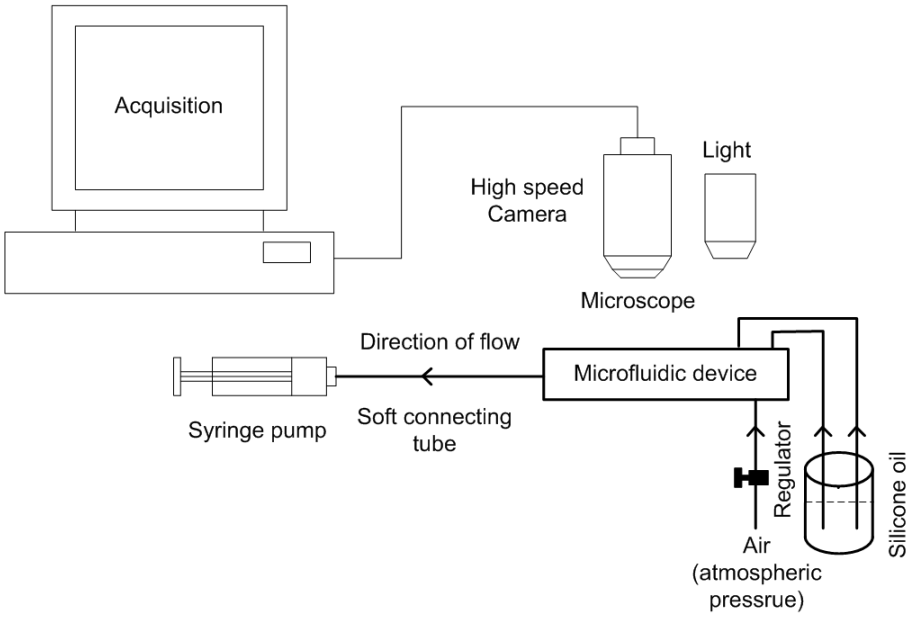

Figure 8.6 Schematic of the negative pressure experimental test: Type-2

8.3 Preparation of Droplet and Bubble

Water droplet in silicone oil (W/O) and air bubble in silicone oil (A/O) were produced utilizing new T and H devices. Water droplet was produces only using positive pressure (type-1) setup. In this case, both the dispersed phase (water) and continuous phase (silicone oil) were injected into the devices at well-controlled flow rates utilizing several syringe pumps. While fluids sample stream flows through the micro-droplet generation area, breakup of the droplet occurs and a high speed CMOS camera was used to record the droplet generation process. Figure 8.7 presents the schematic view of continuous and dispersed flow in type-1 setup.

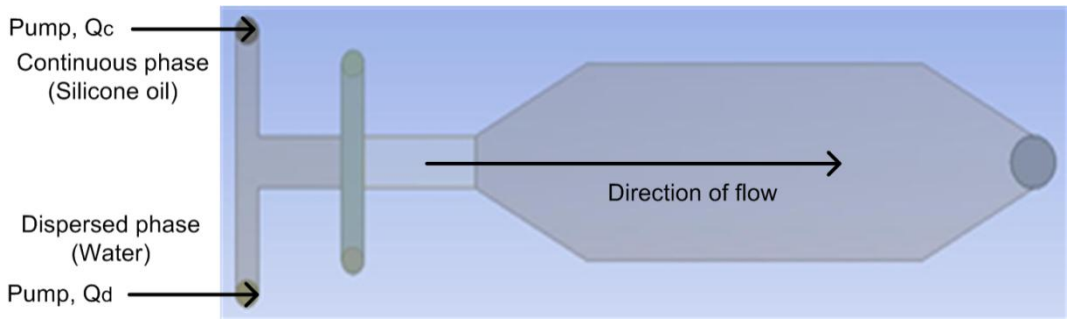

(a) H-1 device

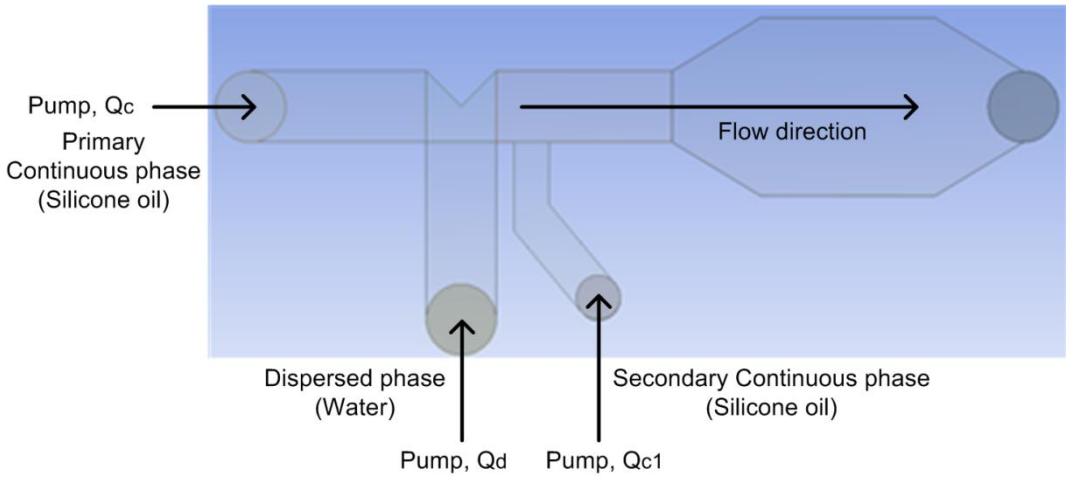

(b) T-2 device

Figure 8.7 Schematic diagram of continuous and disperse flows in type-1 setup during droplet production

Whereas air bubble was produces using both positive pressure (type-1) and negative pressure (type-2) setups. In the case of type-1, continuous phase (silicone oil) was injected into the inputs of the device via syringe pumps and dispersed phase (air) was supplied from a cylinder containing compressed air. In the case of type-2, a syringe pump was attached to the output of the prototype, and one input was open to air with a regulator and other inputs were connected to silicone oil container. The syringe pump works in the reverse way and production of droplet/bubble occurs inside the device. The micro-droplets/micro-bubbles inside the tank were observed and recorded by the CMOS camera. Figure 8.8 presents the schematic view of continuous and dispersed flow direction during type-2 setup.

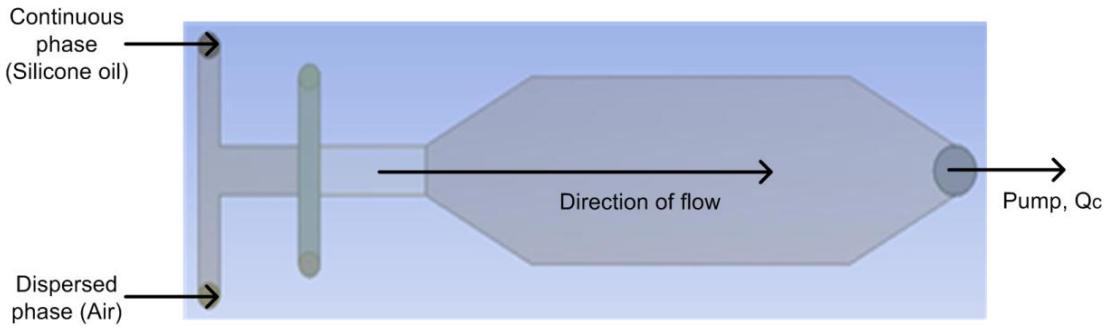

(a) H-1 device

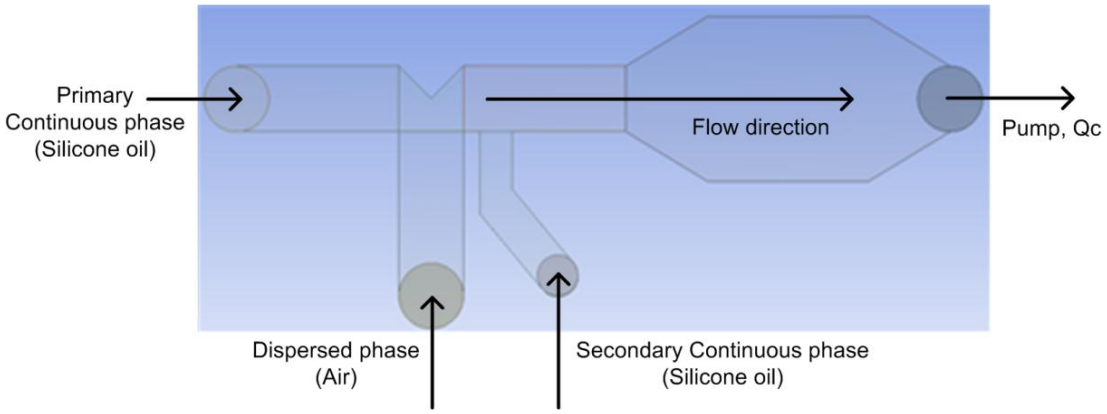

(b) T-2 device

Figure 8.8 Schematic diagram of continuous and disperse flows in type-2 setup during bubble production

8.4 Measurement of Droplet and Bubble

Water droplet in silicone oil and air bubble in silicone oil were prepared using various micro-devices. To produce droplets and bubbles continuous and disperse phases are introduced separately in the micro devices. Both photographs and movies were taken via high speed camera to analyze size distribution and frequency generation via image analysis technique. The diameter of droplet and bubbles were computed using ImageJ software. Around 100 different droplets and bubbles were measured and mean value was taken. Then, frequency of generation was obtained by determining the average period between ten successive droplets/bubbles breakup.

Chapter 9. Results and Discussion: Droplet and Bubble

One of the main goals of this work is to design new micro-devices for the production of small homogeneous droplets and bubbles using low energy. We investigate two-phase flow in four newly designed microfluidic devices which consist of two/three channels as inlets and a connecting channel leading to a wider outlet section which is called tank. Over a broad range of flow rates of 10 ~ 230 ml/h in 400 ~ 800 μm microchannels, corresponding to Capillary numbers of 0.01 ~ 0.18, a two-phase flow map is presented. The flow patterns are distinguished as flow related squeezing and dripping regime. These phenomena are interpreted as Capillary instability, squeezing and shearing by considering the contribution of different forces acting at the oil-water and oil-air interface. The developed devices provide us with a broad choice to generate droplets and bubbles of different size and number by modifying the continuous and dispersed flow rates.

9.1 Water in Silicone Oil Droplet (W/O)

Two immiscible phases (water and silicone oil) are fed into inlets by syringe pumps. They meet at the entrance of the constriction channel, forming water in oil flow due to the wettability of the channel walls. Study of control and reproducibility of drop size for the different continuous and dispersed flow rate was carried out for T-1, T-2, H-1 and H-2 devices. Droplet was created by positive pressure (type-1) experiment where silicone oil and water were the continuous and disperse phase, respectively.

Firstly, diameters of droplets found in experimental tests for different devices were captured by CMOS camera. Roughly 100 droplets were measured using ImageJ software and a normal distribution was found for all the cases, as an example, Figure 9.1 shows the distribution of droplet size in H-1 device at Q_c = 100 ml/h and Q_d = 5 ml/h. Afterward mean value is taken as average diameter for all the cases.

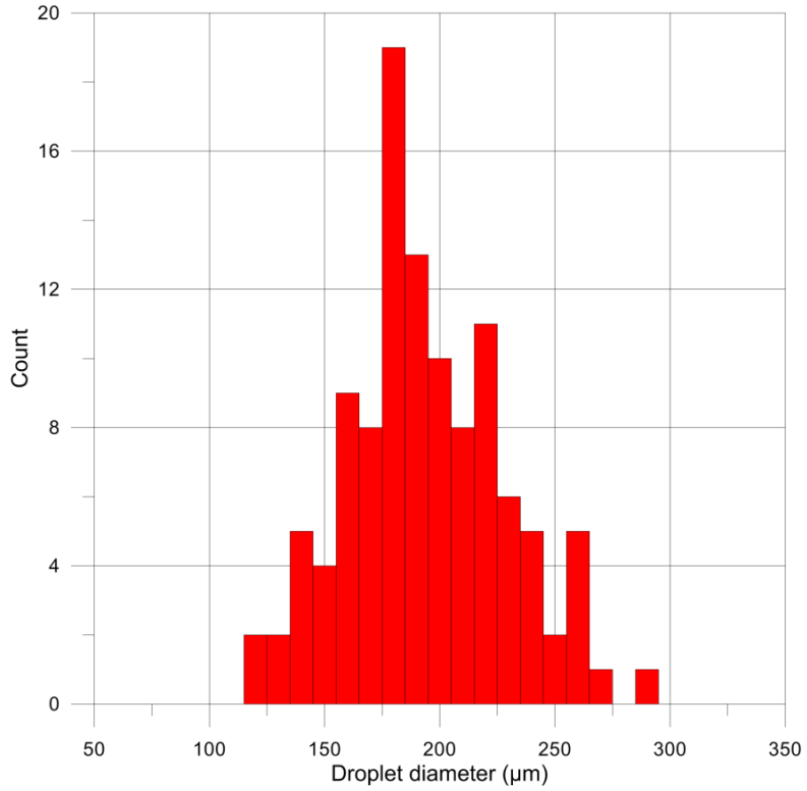

Figure 9.1 Droplet size distribution in H-1 device at Q_c = 100 ml/h and Q_d = 5 ml/h

9.1.1 Droplet in H Devices

The influence of dispersed flow rate (Q_d) on the drop size is studied for H-1 device. Figure 9.2 shows the generation of droplet inside the H-1 device for two dispersed flow rate, 5 ml/h and 10 ml/h. It is noticeable that drop size decreases with the increase of continuous flow rate. Comparing the pictures, it is clear that size of droplet becomes slightly bigger when dispersed flow rate increases from 5 ml/h to 10 ml/h.

Dispersed flow rate, Q_d = 5 ml/h	Dispersed flow rate, Q_d = 10 ml/h
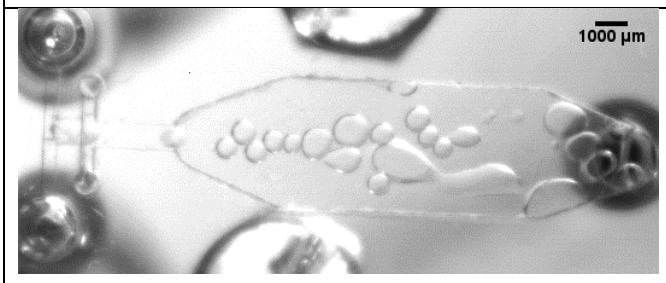	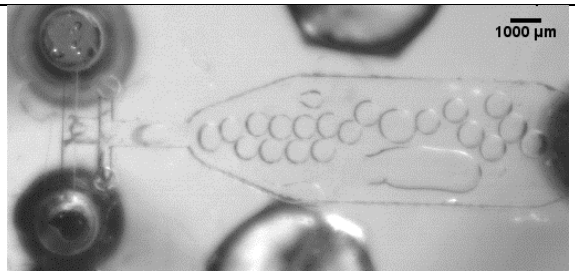
Q_c = 30 ml/h	Q_c = 20 ml/h
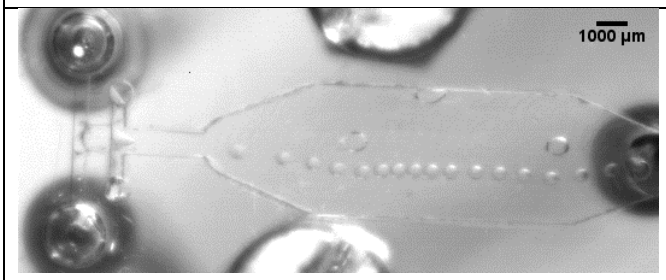	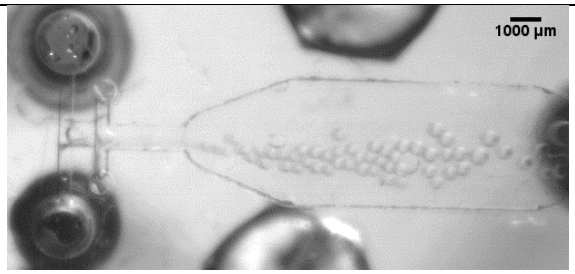
Q_c = 80 ml/h	Q_c = 100 ml/h
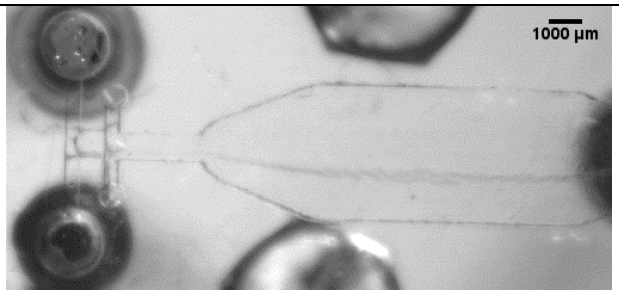	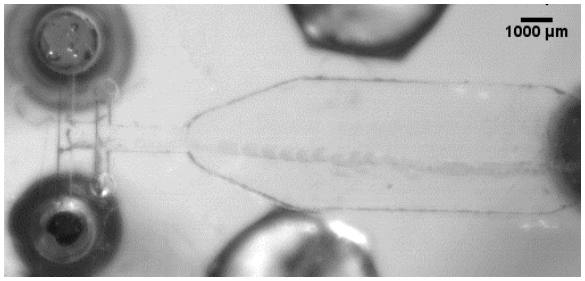
Q_c = 150 ml/h	Q_c = 150 ml/h

Figure 9.2 Microdroplets in H-1 device at various continuous flow rates

Figure 9.3 illustrates the dependency of drop size on two dispersed flow rate in H-1 device. Droplet size decreases with the increase of continuous flow for both dispersed flow rate. It is obvious that drop size depends strongly on continuous flow rate rather than the dispersed flow rate.

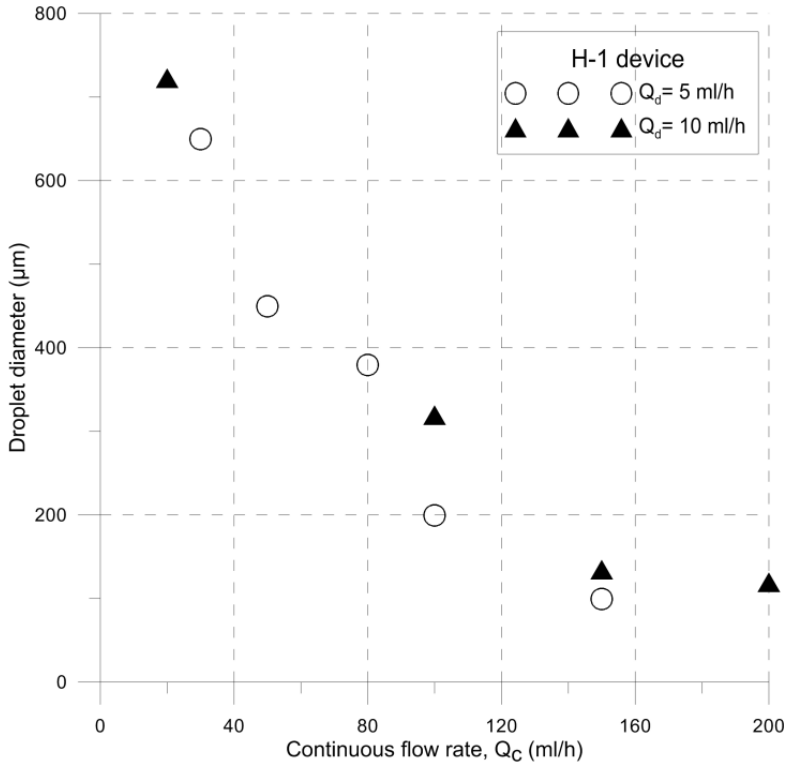

Figure 9.3 Dependency of droplet size on dispersed flow rate in H-1 device

Afterword, the influence of continuous flow rate on the size of droplet size was also tested. The droplet size decrease with the increase of continuous flow rate when the dispersed flow rate remain constant in both H-1 and H-2 devices as shown in Figure 9.2 and Figure 9.4. Values of droplet size and frequency of generation in H-1 and H-2 devices are given in Table 9.1.

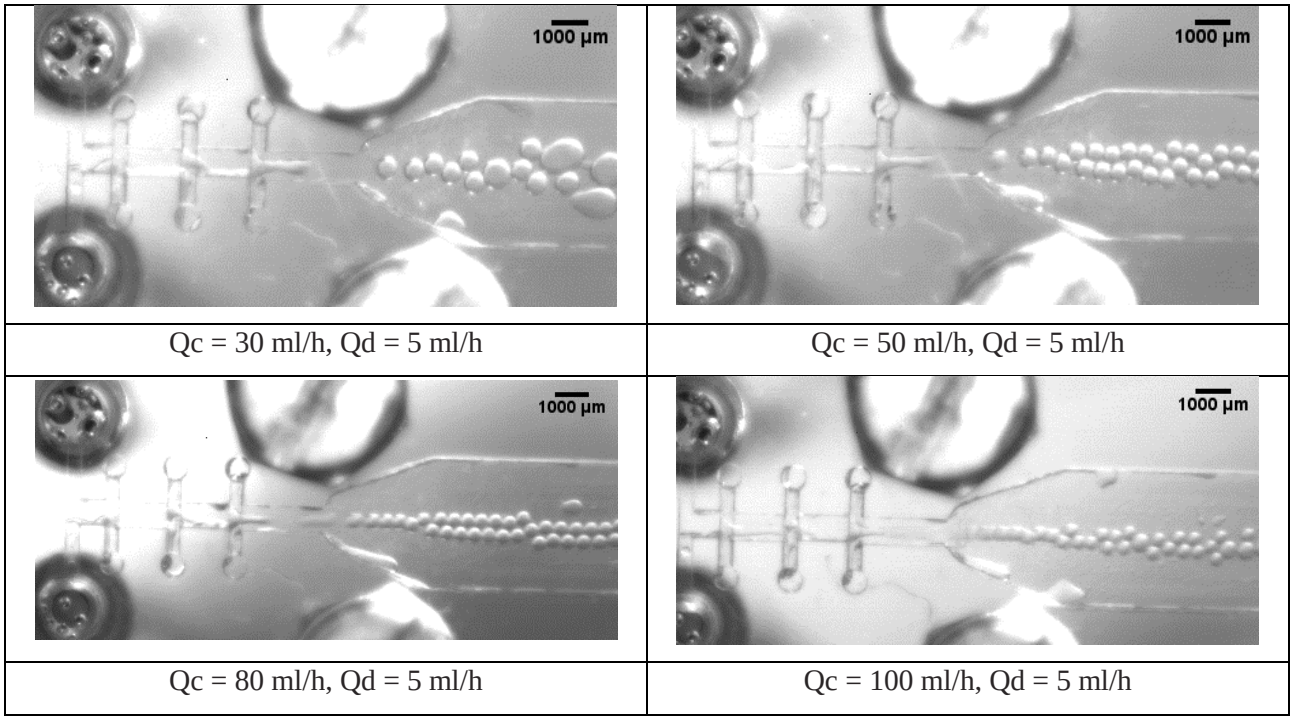

Figure 9.4 Microdroplets in H-2 device at constant dispersed flow rate (Q_d = 5 ml/h)

Table 9.1 Flow rate, mean diameter and frequency related to the production of droplet in H-1 and H-2 devices

Name of device	Continuous flow rate (Q_c) (ml/h)	Dispersed flow rate (Q_d) (ml/h)	Ca	Mean diameter (µm)	Frequency (Hz)
H-1	30	5	0.035721	650	0.5
	50	5	0.059536	450	1.25
	80	5	0.095257	380	2.5
	100	5	0.119071	200	8
	150	5	0.178607	100	15
	20	10	0.023814	723	0.75
	100	10	0.119071	320	10
	150	10	0.178607	135	-
	200	10	0.238143	120	-
H-2	30	5	0.035721	570	0.5
	50	5	0.059536	450	1.25
	80	5	0.095257	330	2.5
	100	5	0.119071	310	8
	150	5	0.178607	170	15

Figure 9.5 shows the dependency of droplet size on the ratio of continuous and dispersed flow rates (Q_c/Q_d) for H-1 and H-2 devices. As seen, drop size decreases with the increase of the ratios; at the beginning (at low value of Q_c/Q_d), H-2 device gives smaller droplet then H-1 device but at the end, H-1 yields the better result.

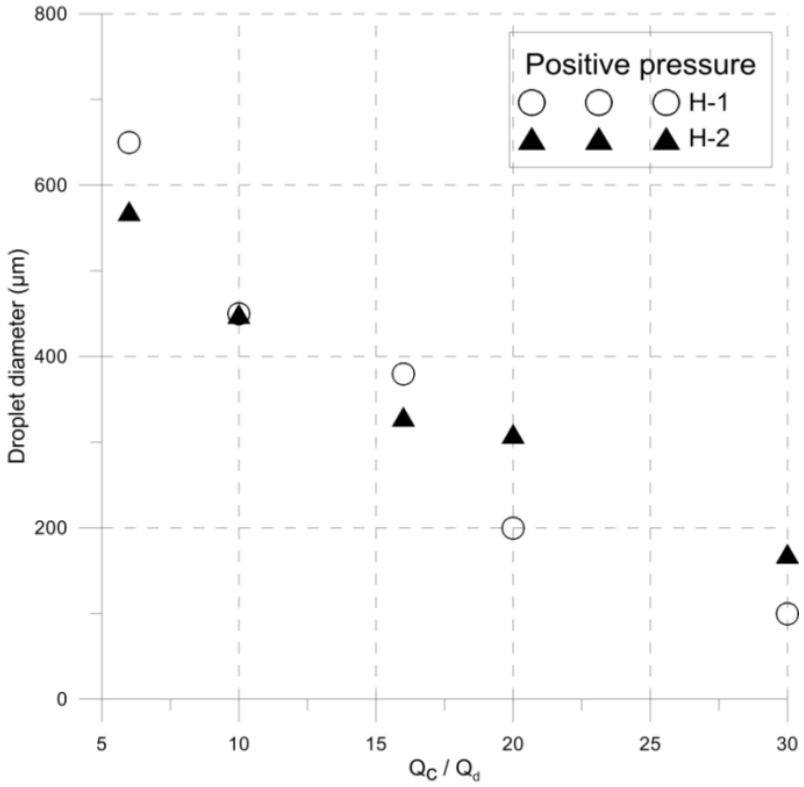

Figure 9.5 Droplet diameters vs. Q_c/ Q_d in H-1 and H-2 devices

9.1.2 Droplet in T Devices

Experimental tests for the generation of droplet in T-1 device were also performed at different continuous flow rate. Figure 9.6 shows the droplet generated at two constant dispersed flow rates of 5 ml/h and 10 ml/h while changing the continuous flow rate. It is evident that size of the droplet decreases with the increase of continuous flow rate, as expected.

Dispersed flow rate, Q_d = 5 ml/h	Dispersed flow rate, Q_d = 10 ml/h
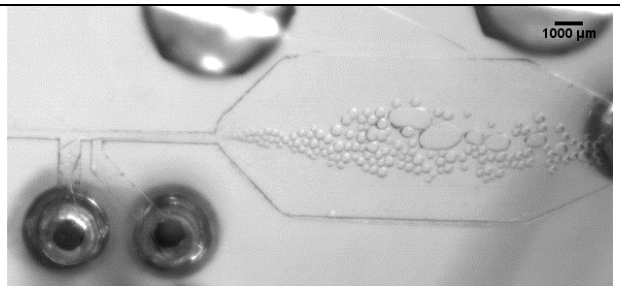	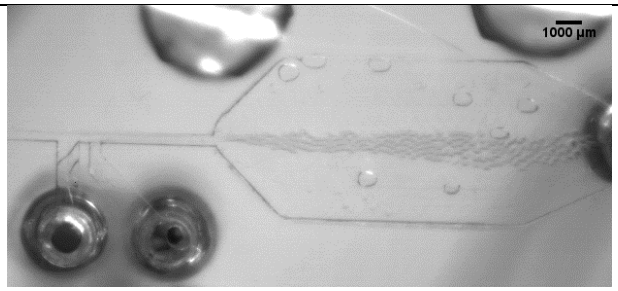
Q_c = 30 ml/h, Q_{c1} = 10 ml/h	Q_c = 100 ml/h, Q_{c1} = 10 ml/h
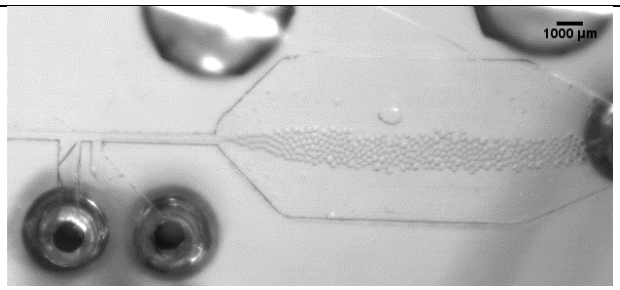	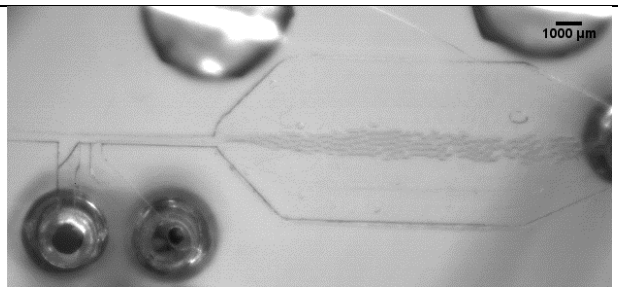
Q_c = 80 ml/h, Q_{c1} = 10 ml/h	Q_c = 100 ml/h, Q_{c1} = 20 ml/h
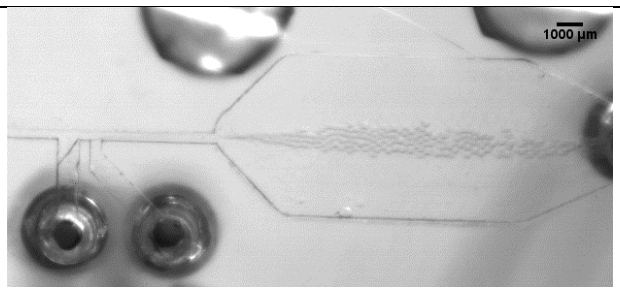	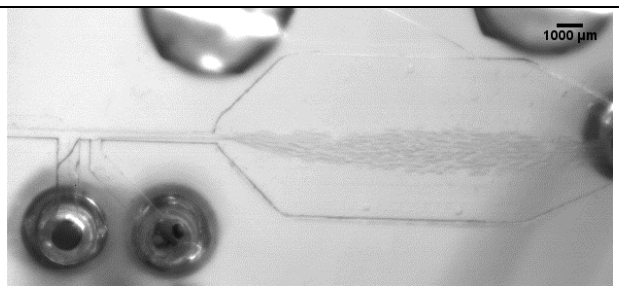
Q_c = 100 ml/h, Q_{c1} = 10 ml/h, Q_d = 5 ml/h	Q_c = 150 ml/h, Q_{c1} = 10 ml/h

Figure 9.6 Droplets in T-1 device at various continuous flow rates

Similarly the production of droplet in T-2 device was also examined. Figure 9.7 shows the droplet size decreases with the increase of both continuous and dispersed flow rates. The value of droplet diameter, frequency of generation related to flow rate for T-1 and T-2 devices are given in Table 9.2.

Dispersed flow rate, Q_d = 5 ml/h	Dispersed flow rate, Q_d = 10 ml/h
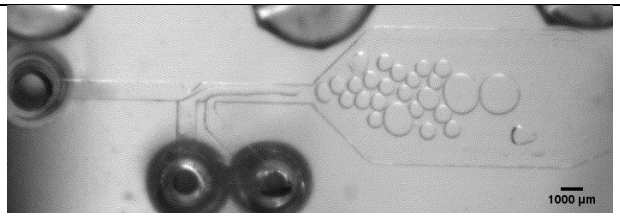	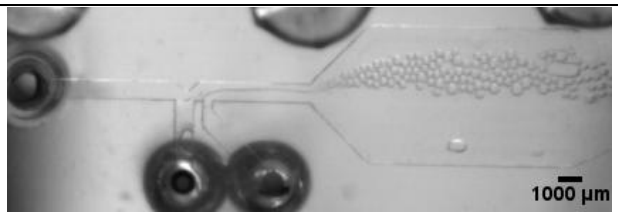
Q_c = 10 ml/h, Q_{c1} = 10 ml/h	Q_c = 50 ml/h, Q_{c1} = 50 ml/h
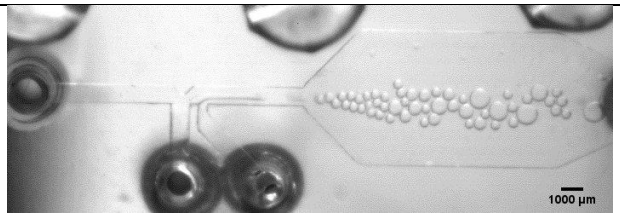	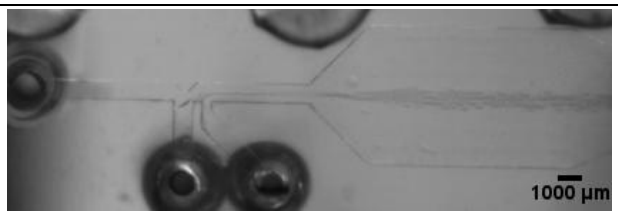
Q_c = 20 ml/h, Q_{c1} = 50 ml/h, Q_d = 5 ml/h	Q_c = 80 ml/h, Q_{c1} = 50 ml/h
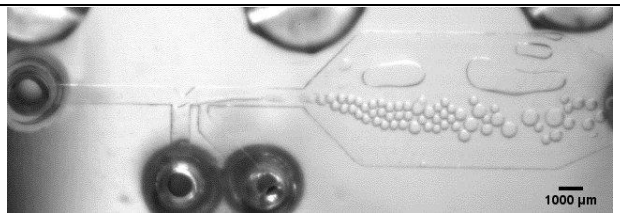	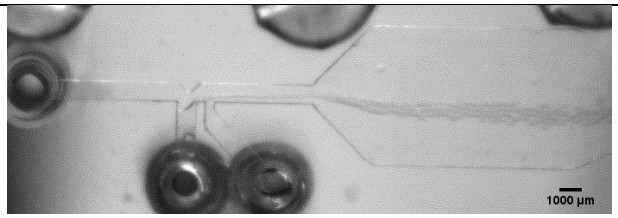
Q_c = 50 ml/h, Q_{c1} = 20 ml/h	Q_c = 100 ml/h, Q_{c1} = 50 ml/h

Figure 9.7 Droplets in T-2 device at various continuous and dispersed flow rates

Table 9.2 Flow rate, mean diameter and frequency related to the production of droplet in T-1 and T-2 devices

Name of device	Continuous flow rate (Q_c) (ml/h)	Secondary continuous flow rate (Q_{c1}) (ml/h)	Dispersed flow rate (Q_d) (ml/h)	Ca	Mean diameter (µm)	Frequency (Hz)
T-1	10	10	5	0.011907	380	1
	30	10	5	0.035721	205	6
	50	10	5	0.059536	180	10
	80	10	5	0.095257	170	15
	100	10	5	0.119071	145	21
	130	10	5	0.154793	115	35
	100	10	10	0.119071	130	-
	100	20	10	0.119071	130	-
	150	10	10	0.178607	90	-
T-2	10	10	5	0.011907143	625	0.7
	20	20	5	0.023814286	360	1.25
	50	50	10	0.059535714	300	10
	80	80	10	0.095257143	130	21
	100	100	10	0.119071429	120	28
	150	100	10	0.178607143	100	40
	150	150	20	0.178607143	80	53

Dependency of droplet size on the ratio of continuous flow rate and dispersed flow rate (Q_c/Q_d) was also studied for T-1 and T-2 devices. Figure 9.8 reviles that droplet size decreases as the value of ratio increase, as like H devices.

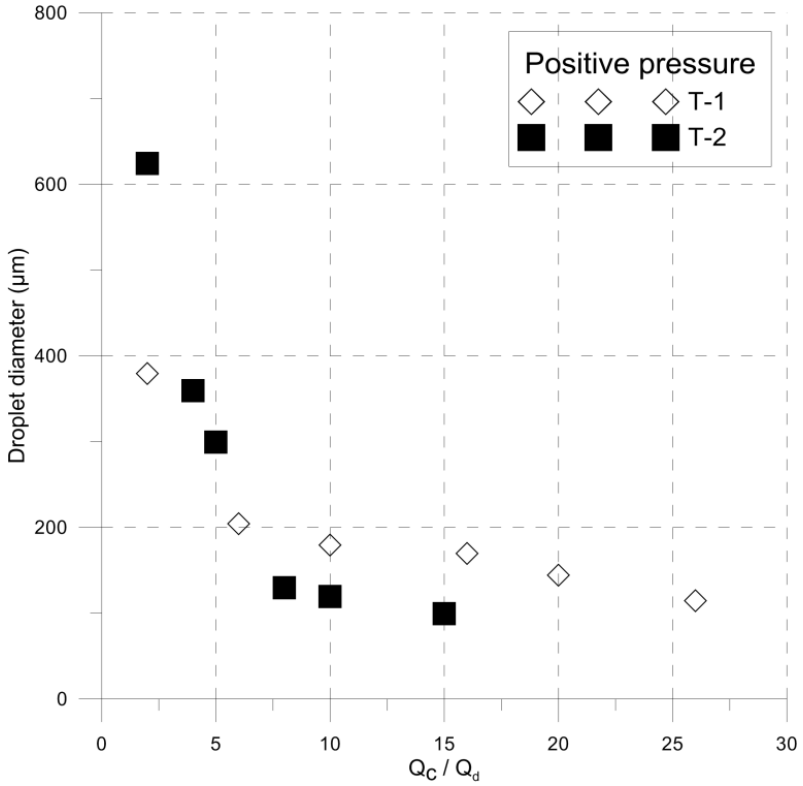

Figure 9.8 Droplet diameters vs. Q_c/Q_d in T-1 and T-2 devices

9.1.3 Droplet Breakup Regime

The mechanism of droplet breakup inside the devices was observed. Transition from one droplet formation regime to another regime is strongly dependent on the Capillary (Ca) numbers of the continuous phase. Two regimes are commonly observed for the production of droplets in T-junction device: (i) the squeezing regime where the generated droplet blocks the channel of the continuous phase fluid and creates a pressure drop across the droplet, and (ii) the dripping regime where the size of the droplets is much smaller than the dimensions of the channel of the continuous phase fluid. In the squeezing regime, because droplets restrict the flow of continuous phase fluid, there is an increased pressure upstream, which plays an essential role in the droplet pinch-off.

In this research work, two droplet breaking regimes were found for four devices. Figure 9.9 shows the squeezing and dripping regime at the inlet section of H-1 and T-1 devices when Capillary

numbers were varied. When Capillary number is low, (Ca<0.1) cross-flow shear force caused by the continuous phase fluid is much lower comparing to the interfacial force and cannot rupture the dispersed phase to drops. So the two-phase flow is in plugs flow regime. In this regime, the interfacial force dominates the shear force, and the dynamics of break-up is dominated by the pressure drop across the plug as it forms, which we call the squeezing regime. When Ca>0.1, the cross-flow shear force is large enough to play an important role in the process of break-up, and the two phase flow is in drops flow regime. In this regime, the dynamics of break-up is dominated by the forces balance between shear force and interfacial force, which we call the dripping regime.

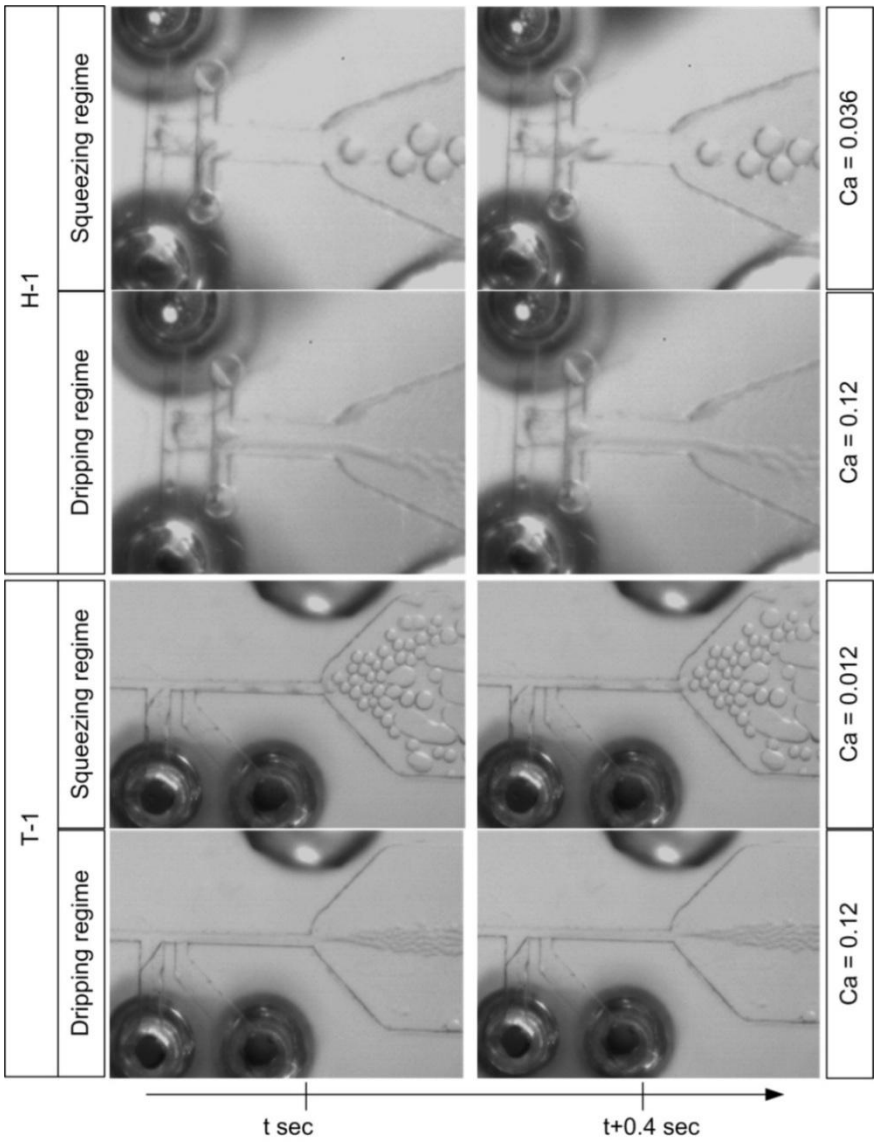

Figure 9.9 Phase diagram for microfluidic H-1 and T-1 devices at different Capillary numbers

9.1.4 Comparison of Droplet Size

Over a wide range of flow rates of both phases were used for the experiments tests which generate reasonable uniform sized droplets. The volume of these droplets can be adjusted by changing the rates of flow of both dispersed phase (Q_d) and continuous phase (Q_c). We are interested in droplet generation and how the sizes of the droplets formed in various devices depend on the continuous flow rates. Figure 9.10 illustrates the dependence of droplet diameter on continuous flow rates (Q_c) in four examined devices as well as in a coflow device presented by Castro et al. (56). They used water-glycerol mixture and different polydimethylsiloxane oils as continuous and dispersed phases in a coflow device where the outer capillary and inner capillary diameter was 1000 µm and 50 µm, respectively. As seen in Figure 9.10, all curves show the same trend, drop size decrease with the increase of flow rate. Our examined devices give significantly smaller drop compare to the results published by Castro et al. Among the five devices, T-1 and T-2 give the best value at all examined flow rate. It is worth mentioning that the minimum dimension of H and T devices are 400 µm and 800 µm, respectively. Here, we can create droplet of about 100 µm in diameter, which is at least 4 times less in dimension than that of the devices. Therefore the energy consumption is certainly low. Whereas, the coflow device presented by Castro and others can generate droplets which are much bigger than the device geometry.

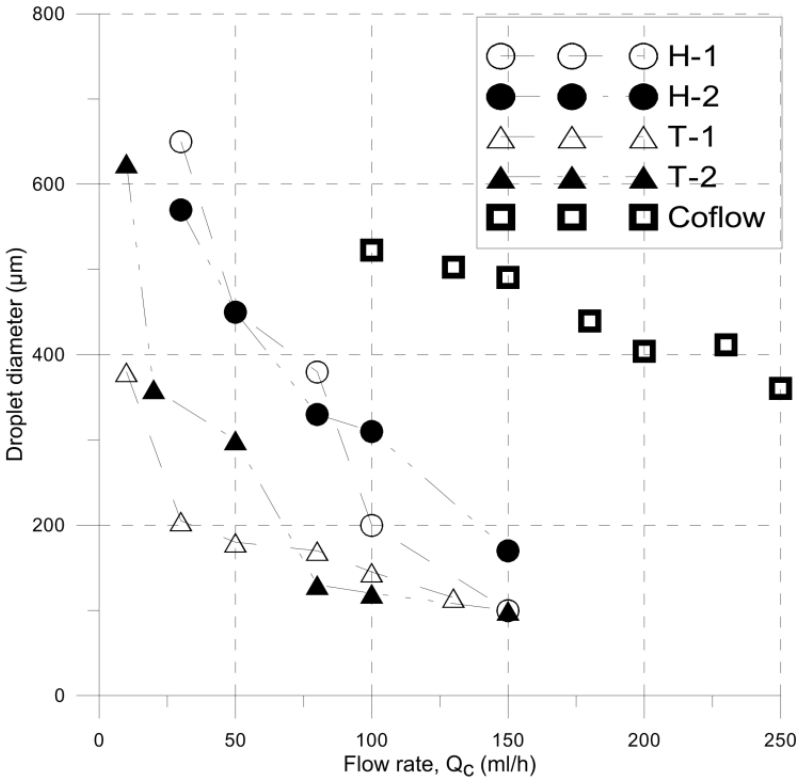

Figure 9.10 Dependency of drop size on the continuous flow rate in T-1, T-2, H-1, H-2 devices and in a coflow (56) device

9.1.5 Comparison of Droplet Generation Frequency

Frequency of droplet formation depends on the shape and geometry of device, and total flow rate of continuous and dispersed phases. For a particular device the number of droplet generation will increase with the increase of flow rate. This phenomenon is illustrates in Figure 9.11 for four examined devices. Number of droplet generation increases linearly with the continuous flow rate for T-1 and T-2 devices and they also provide the highest yield rate. But in the case of H-1 and H-2 devices, droplet production rate is much low.

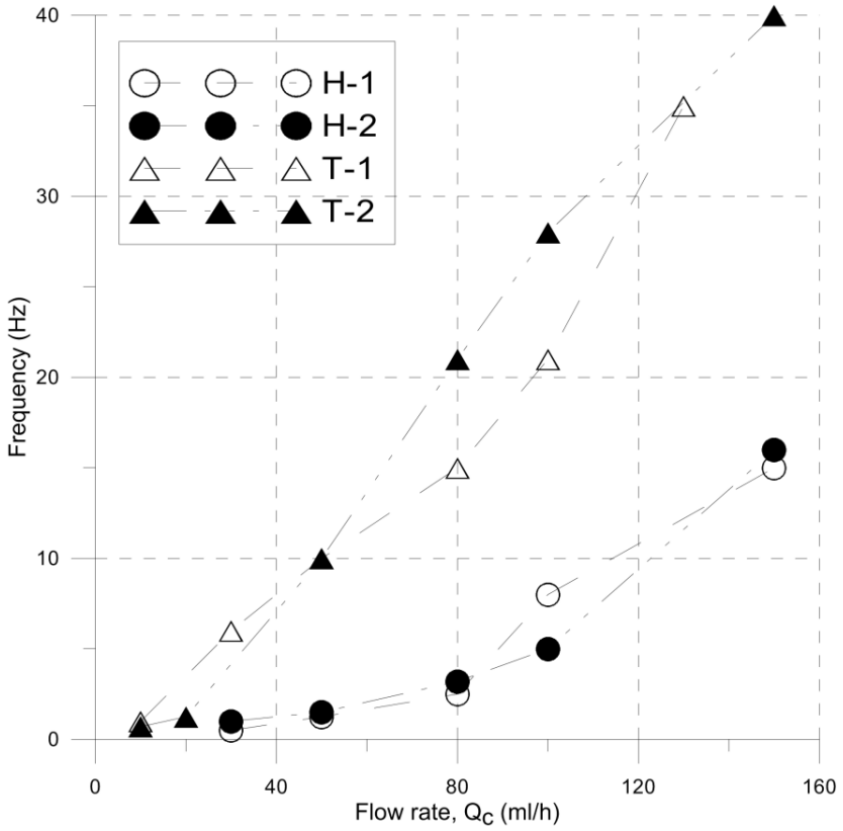

Figure 9.11 Frequency of droplet formation at different continuous flow rate in H-1, H-2, T-1 and T-2 devices

9.2 Air Bubbles in Silicone Oil (A/O)

The possibility of mono-dispersed microbubble formation was tested by positive pressure (type -1) and negative pressure (type-2) experimental setups. Four devices namely, T-1, T-2, H-1 and H-2 were used for the microbubble production. The bubble size and production rate was computed by image analysis technique.

At first, bubbles created in positive and negative pressure experimental tests were captured and roughly 100 bubbles were measured using ImageJ software. Figure 9.12 shows the distribution of bubble size in H-1 device at Q_c = 200 ml/h. Afterward mean value is taken as average diameter for all the cases.

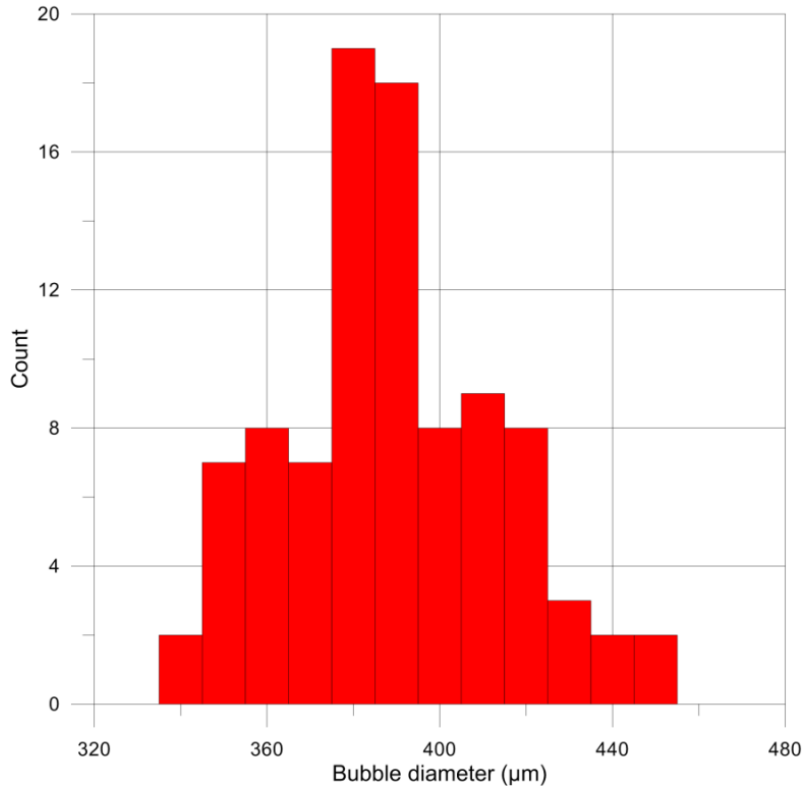

Figure 9.12 Bubble size distribution in H-1 device at Q_c = 200 ml/h

9.2.1 Bubble in H Devices

The comparison between bubbles generation in H-1 device using positive and negative pressure at different continuous flow rate is presented in Figure 9.13. In the case of positive setup, big bubbles were created at the exit of H-1 device and afterward coalescence occurred between successive bubbles. Therefore big irregular bubbles can be seen inside the tank. But at high flow rate uniform

regular bubbles were found. On contrary, negative pressure gives small periodic bubble at almost all examined flow rates. Size of bubbles decreases with the increase of flow rates for both cases.

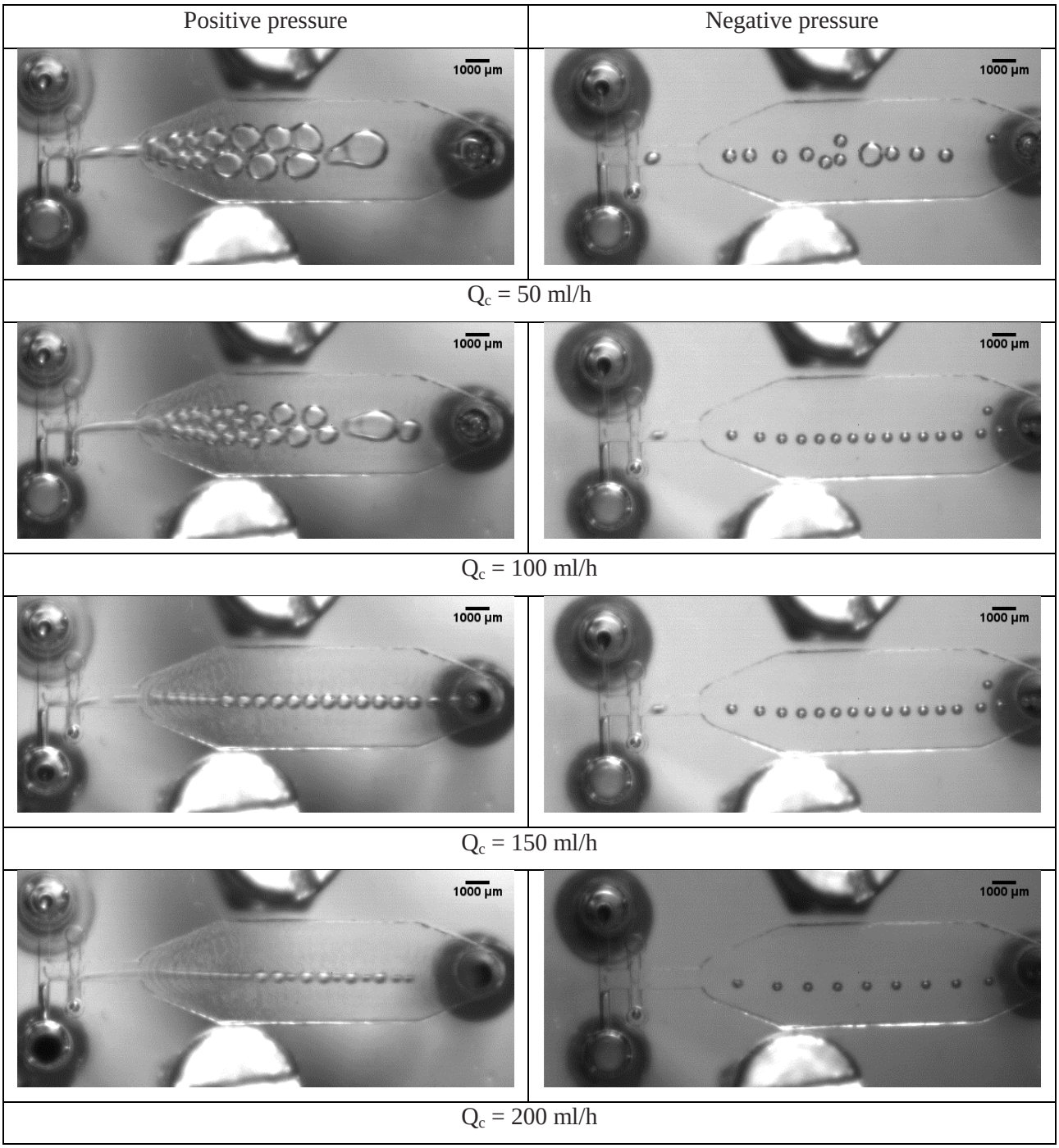

Figure 9.13 Microbubbles in H-1 device at various flow rates

Figure 9.14 shows the comparison of bubbles generation using positive and negative pressure setups in H-2 device. As like H-1 device, coalescence of bubbles also occurred inside the tank in both positive and negative tests. H-2 device in made up of 3 H-modules connected in series, so breakup of bubbles took place inside each H-module. Therefore several rows of asymmetric bubbles can be seen inside the tank. Again the bubble size and production rate depends on the flow rate. As the flow rate increases the bubble diameter decreases. The values of mean diameter and frequency of bubbles generation in H-1 and H-2 devices is given in Table 9.3.

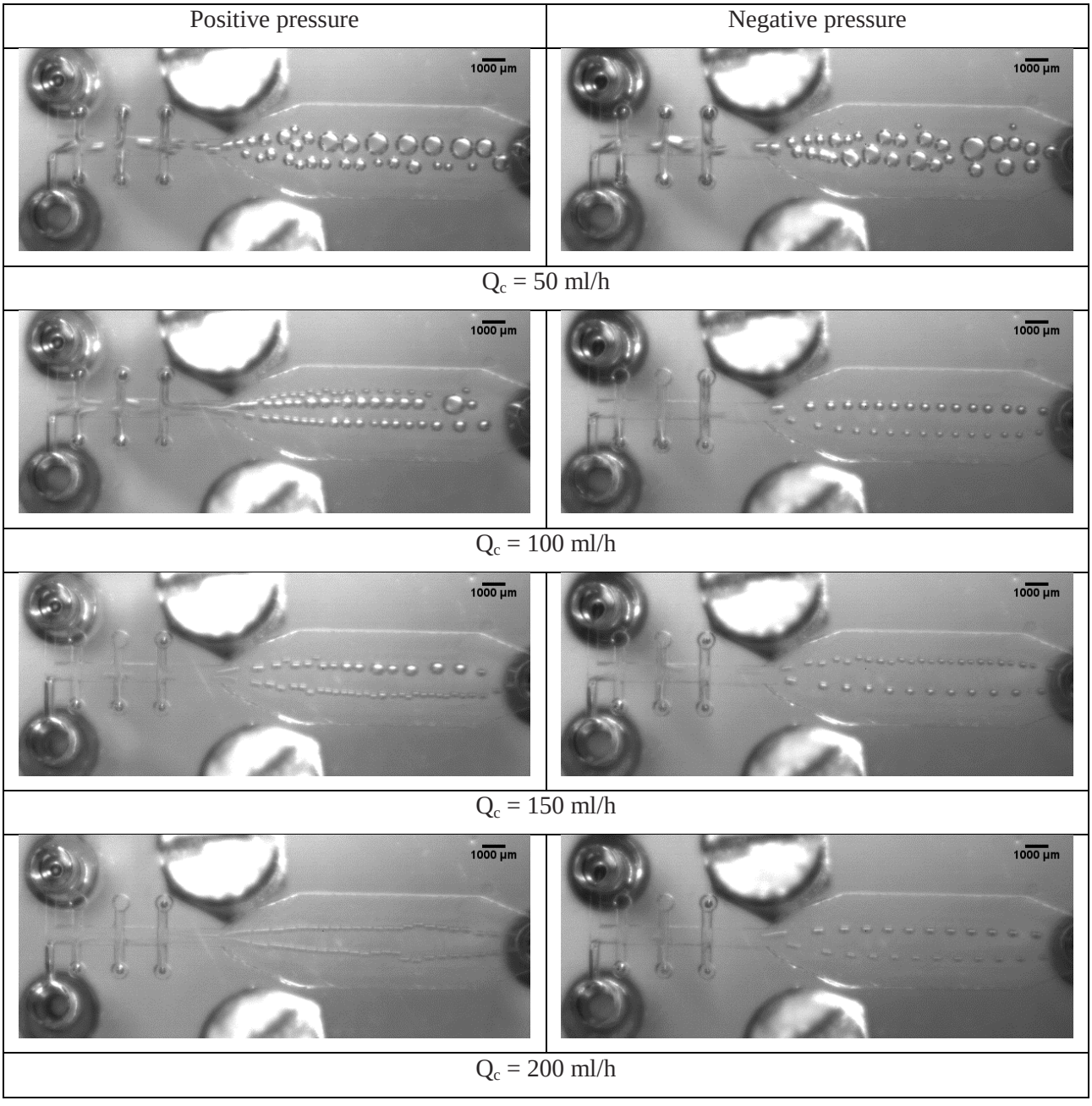

Figure 9.14 Microbubbles in H-2 device at various flow rates

Table 9.3 Flow rate, mean diameter and frequency related to the production of bubble in H-1 and H-2 devices

Name of device	Flow rate (ml/h)	Ca	Positive pressure (Type-1)		Negative pressure (Type-2)	
			Mean diameter (µm)	Frequency (Hz)	Mean diameter (µm)	Frequency (Hz)
H-1	20	0.010419	880	1.25	635	0.25
	50	0.026047	640	2.5	510	0.35
	100	0.052094	440	5	405	0.45
	150	0.078141	300	6.4	390	0.55
	200	0.104188	285	10	330	1.1
	230	0.119816	250	20	250	1.75
H-2	20	0.010419	440	1	500	0.2
	50	0.026047	385	3.5	280	0.6
	100	0.052094	215	11	225	3
	150	0.078141	200	18	150	4
	200	0.104188	180	20	140	5.1
	230	0.119816	130	32	500	0.2

9.2.2 Bubble in T Devices

The generation of bubbles was also investigated in T-1 and T-2 devices using positive and negative pressure setups. Bubble size and uniformity depends upon the physical properties of the liquid, the gas and liquid flow rates and the dimensions and profile of the orifice and channels. Figure 9.15 illustrates the bubble generation at different continuous flow rate in T-1 device using negative and positive pressure tests. Regular symmetric small bubbles can be seen in case of negative presser setup and diameter of bubbles decreases with the flow rate. Whereas big chaotic bubbles are seen when positive pressure setup was used.

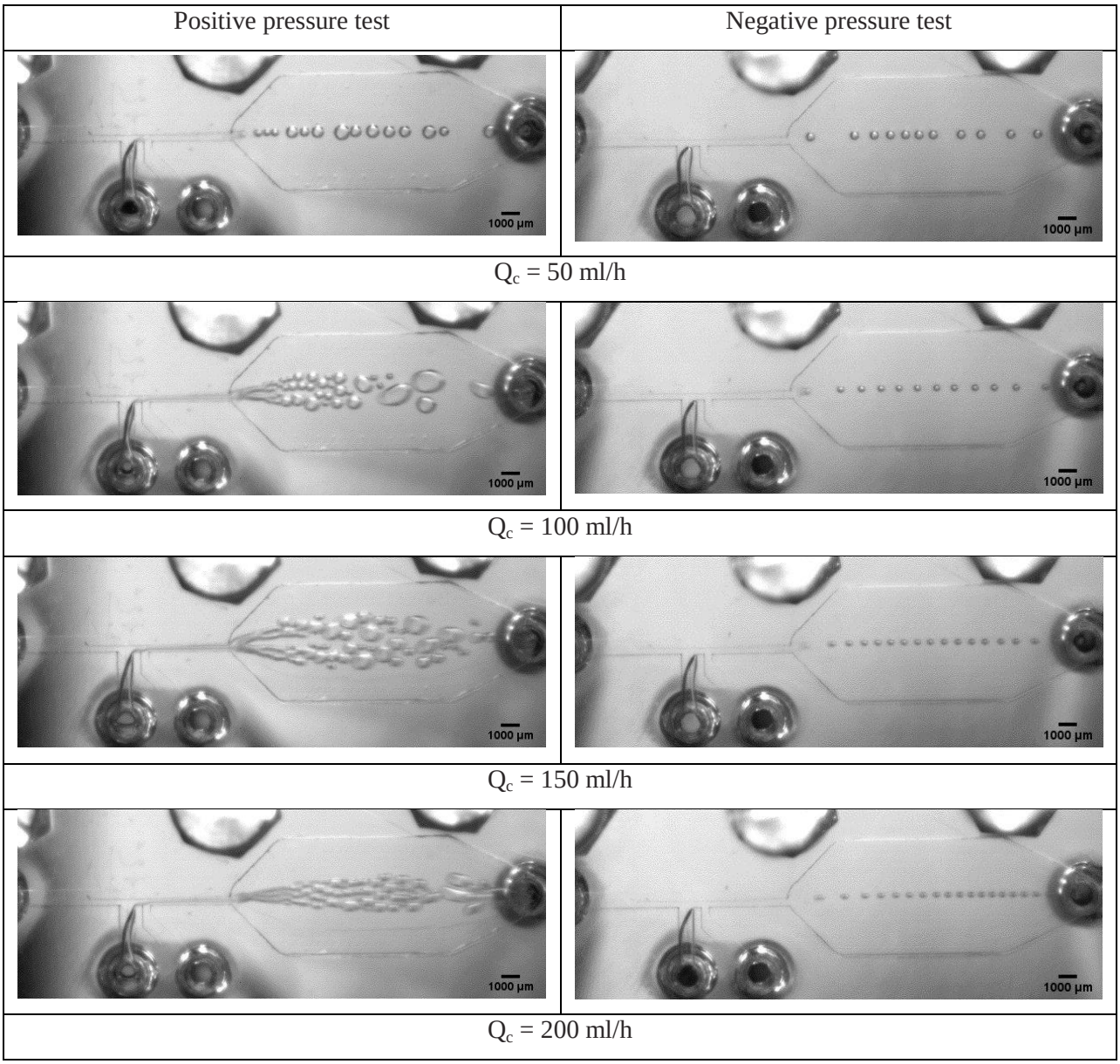

Figure 9.15 Microbubbles in T-1 device varying continuous flow rates

Again, Figure 9.16 shows the same phenomenon in case of T-2 device, negative pressure setup gives small regular bubbles. Table 9.4 shows the values of bubble size and frequency of production under different experimental conditions for T-1 and T-2 devices.

Positive pressure test	Negative pressure test
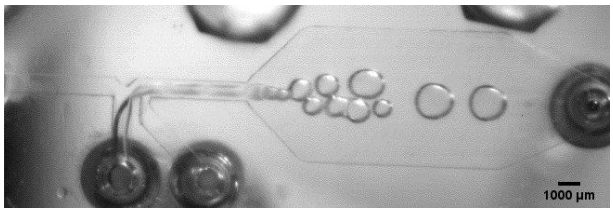	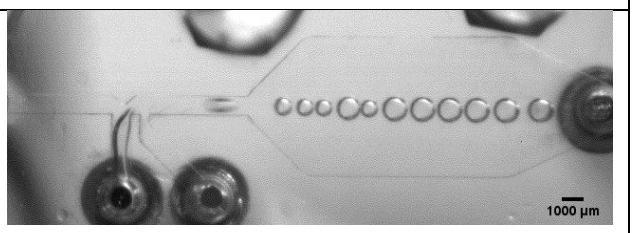
Q_c = 50 ml/h	
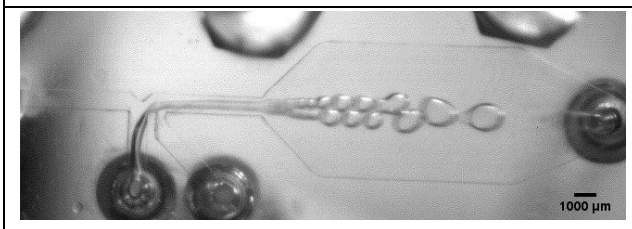	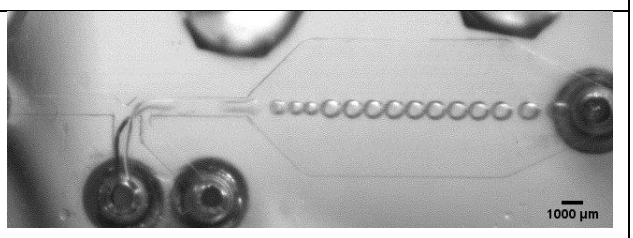
Q_c = 100 ml/h	
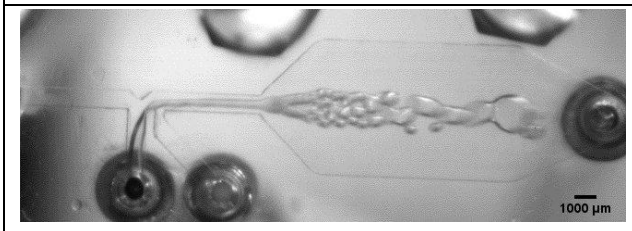	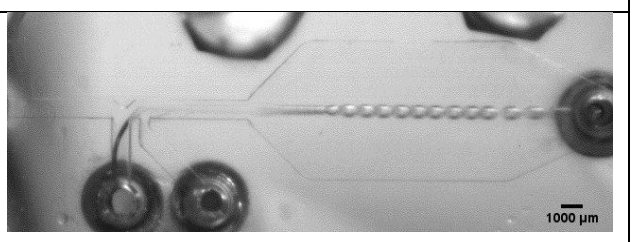
Q_c = 150 ml/h	
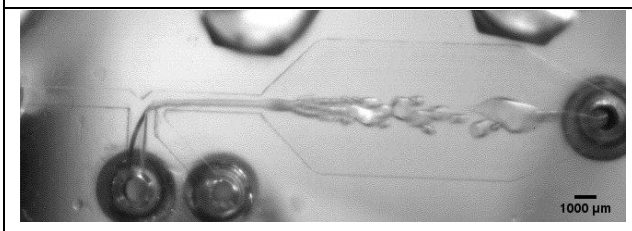	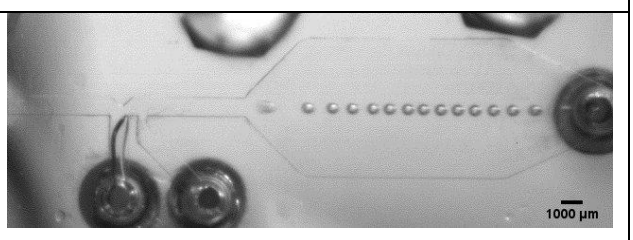
Q_c = 200 ml/h	

Figure 9.16 Microbubbles in T-2 device varying continuous flow

Table 9.4 Flow rate, mean diameter and frequency related to the production of bubble in T-1 and T-2 devices

Name of device	Flow rate (ml/h)	Ca	Positive pressure (Type 1)		Negative pressure (Type 2)	
			Mean diameter (µm)	Frequency (Hz)	Mean diameter (µm)	Frequency (Hz)
T-1	20	0.010419	620	1	500	0.18
	50	0.026047	410	1.5	390	0.3
	100	0.052094	255	10	285	0.45
	150	0.078141	240	15	250	1.75
	200	0.104188	225	22	230	2.35
	230	0.119816	210		208	2.8
T-2	20	0.010419	890	1.5	995	0.35
	50	0.026047	580	5	670	0.9
	100	0.052094	460	11	580	2.2
	150	0.078141	350	20	420	3
	200	0.104188	290	32	345	5
	230	0.119816	250	40	290	6

9.2.3 Bubble Breakup Regime

Bauble breakup at the inlet section of four devices was also studied. When the imposed dispersed pressures and continuous pressures are comparable ($P_d \sim P_c$), the droplet size increases with increasing dispersed phase pressure P_d. Bubble do not form when the pressures are significantly different from each other. For example, if the dispersed phase pressure is significantly smaller than the continuous phase pressure P_c, the gas phase cannot enter the junction region. In this studied, two bubble breakup regime was found for four examined devices. As an example, Figure 9.17 shows the squeezing and dripping regime inside of H-1 and T-2 devices. At small Capillary value (Ca<0.05), squeezing regime can be seen, where the air blocks the constriction channel, and the subsequent build-up of the outer liquid pressure (oil) leads to breakup at the junction. When the continuous phase pressure is increases which implies relative high Capillary value (Ca>0.05), dripping regime is found.

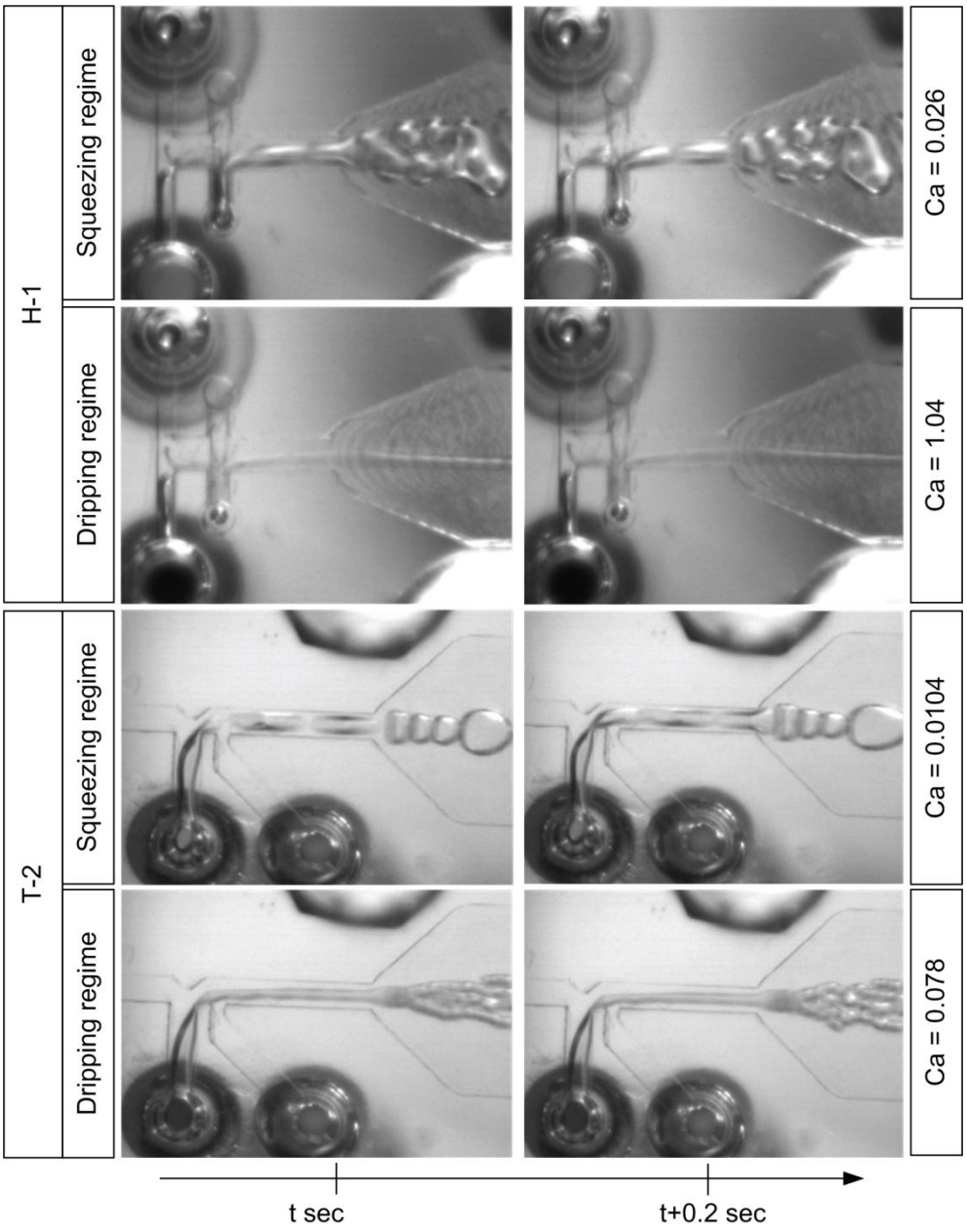

Figure 9.17 Phase diagram for H-1 and T-2 devices at different Capillary numbers

9.2.4 Comparison of Bubble Size

The effect of different geometries and flow rates on bubble size was investigated. Two different experimental methods were used to produce bubbles in four different devices. Figure 9.18 summarizes the relationship between bubble size and flow rate for negative and positive pressure tests. As seen, all curves show the same trend: diameter of bubbles decrease with the increase of continuous flow rates. At low flow rate (50 ml/h), size of bubble produces by different devices varies quite a bit; as the flow rate increases the variation of bubble size reduce and finally around 200-300 µm bubble can be found. It is also notable that negative pressure gives more symmetric regular small bubble than positive pressure test.

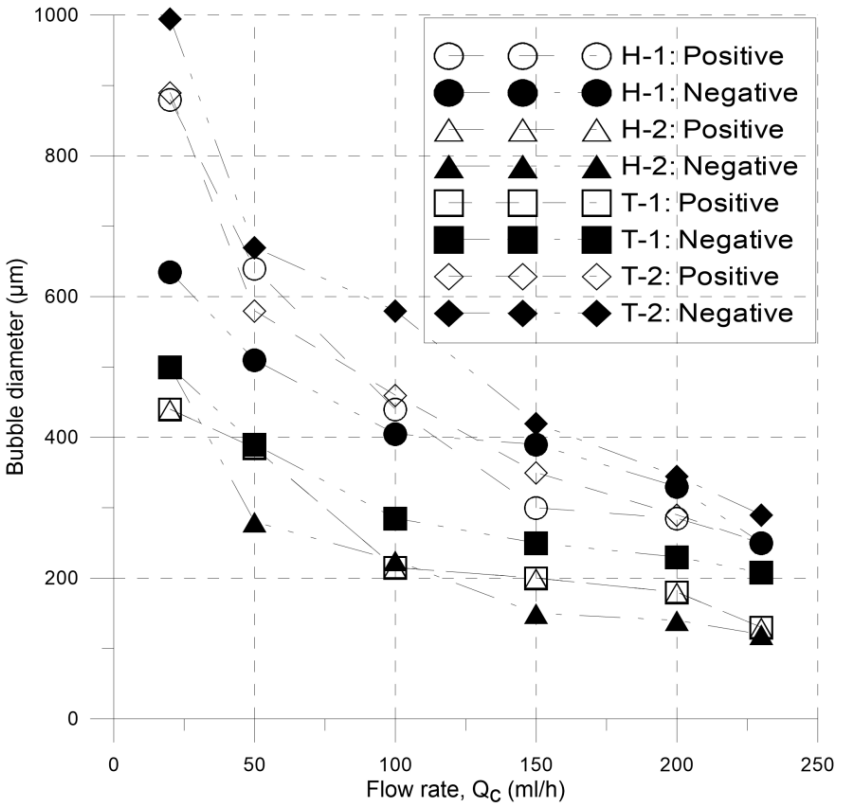

Figure 9.18 Dependency of bubble size on the continuous flow rate in H-1, H-2, T-1 and T-2 devices

9.2.5 Comparison of Bubble Generation Frequency

Figure 9.19 compares the number of bubbles generated per second at various examined flow rates. The frequency of bubble generation is high for all four devices in case of positive pressure setup; T-1 and T-2 devices provide the best production rate among four devices. Negative pressure setup gives poor bubble generation rate. The primary reasons for this may lie in the difference between effective flow rates inside different microchannels.

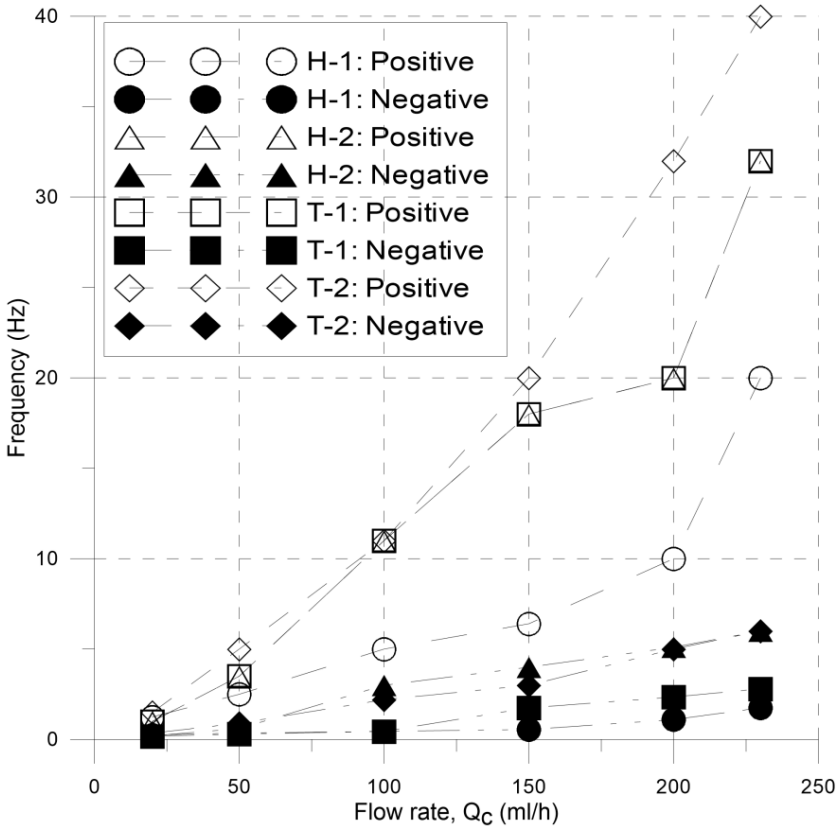

Figure 9.19 Frequency of bubble formation at different continuous flow rate in H-1, H-2, T-1 and T-2 devices

References

1. *The origins and the future of microfluidics.* **M., Whitesides G.** 2006, Nature, pp. 368-373.

2. *Droplet based microfluidics.* **Seemann R., Brinkmann M., Pfohl T., Herminghaus S.** 2012, Rep. Prog. Phys., Vol. 75, pp. 1-41.

3. *Spontaneous droplet formation techniques for monodisperse emulsion preparation-Prespective for food applications.* **Maan A. A., Schroen K., Boom R.** 2011, Journal of Food Engineering, pp. 334-346.

4. *Controlled production of food emulsion using microfluidics.* **Pulido-de-Torres C., Amici E., Gallarino A., Silva M. D., Jousse F.** 2006, Nanotech, Vol. 2, pp. 686-689.

5. *Aerated food gels:fabrication and potential applications.* **Zuniga R. N., Aguilera J. M.** 2008, Trends in Food Science & Technology, pp. 176-187.

6. *Droplets Formation and Merging in Two-Phase Flow Microfluidics.* **Gu H., Duits M. H. G., Mugele F.** 2011, Int. J. Mol. Sci., pp. 2572-2597.

7. *Dynamics of microfluidic droplets.* **Baroud C. N., Gallaire F., Dangla R.** 2010, Lab on a Chip, pp. 2032-2045.

8. *Microfluidic methods for generating continuous droplet streams.* **Christopher G. F., Anna S. L.** 2007, J. Phys. D: Appl. Phys., pp. R319-R336.

9. *Applications of Microfluidic Devices in Food Engineering.* **Skurtys O., Aguilera J. M.** 2008, Food Biophysics, pp. 1-15.

10. *Product engineering of dispersed systems.* **Schubert H., Ax K., Behrend O.** 2003, Trends Food Sci. Tech., pp. 9-16.

11. *Creation and characterization of aerated food products.* **Campbell G. M., Mougeot E.** 1999, Trends Food Sci. Tech., pp. 283-296.

12. *Why food microstructure.* **M., Aguilera J.** 2005, Journal of Food Engineering, pp. 3-11.

13. *Dripping and jetting in microfluidic multiphase flows applied to particle and fiber synthesis.* **Nunes J. K., Tsai S. S. H., Wan J., Stone H. A.** 2013, J Phys D Appl Phys., pp. 1-39.

14. *Silicon array of elongated through-holes for monodisperse emulsion droplets.* **Kobayashi I., Nakajima M., Chun K., Kikuchi Y., Fujita H.** 2001, AIChE J , Vol. 48, pp. 1639-1644.

15. *Prediction of droplet diameter for microchannel emulsification: prediction model for complicated microchannel geometries.* **Sugiura S., Nakajima M., Seki M.** 2004, Ind. Eng. Chem. Res., Vol. 43, pp. 8233-8238.

16. *Dynamic pattern formation in a vesicle-generating microfluidic device.* **Thorsen T., Roberts R., Arnold F., Quake S.** 2001, Phys. Rev. Lett., Vol. 86, pp. 4163-4166.

17. *Shear force induced monodisperse droplet formation in a microfluidic device by controlling wetting properties.* **Xu J. H., Luo G. S., Li S. W., Chen G. G.** 2006a, Lab Chip, Vol. 6, pp. 131-136.

18. *Preparation of highly monodisperse droplet in a T-junction microfluidic device.* **Xu J. H., Li S. W., Tan J., Wang Y. J., Luo G. S.** 2006b, AIChE J , Vol. 9, pp. 3005–3010.

19. *Controllable preparation of monodisperse O/W and W/O emulsions in the same microfluidic device.* **Xu J. H., Li S. W., Tan J., Wang Y. J., Luo G. S.** 2006c, Langmuir, Vol. 22, pp. 7943–7946.

20. *Formation of droplets and bubbles in a microfluidic T-junction scaling and mechanism of break-up.* **Garstecki P., Fuerstman M. J., Stonec H. A., Whitesides G. M.** 2006, Lab Chip, Vol. 6, pp. 437–446.

21. *Theory and numerical simulation of droplet dynamics in complex flows–a review.* **Cristini V., Tan Y. C.** 2004, Lab Chip, Vol. 4, pp. 257-264.

22. *Correlations of droplet formation in T-junction microfluidic devices: from squeezing to dripping.* **Xu J. H., Li S. W., Tan J., Luo G. S.** 2008, Microfluid Nanofluid, Vol. 5, pp. 711-717.

23. *Formation of dispersions using ‘‘flow focusing’’ in microchannels.* **Anna S. L., Bontoux N., Stone H. A.** 2003, Appl. Phys. Lett., Vol. 82, pp. 364-366.

24. *The generation of highly monodisperse droplets through the breakup of hydrodynamically focused microthread in a microfluidic device.* **Xu Q., Nakajima M.** 2004, Appl. Phys. Lett., Vol. 85, pp. 3726-3728.

25. *Formation of simple and compound drops in microfluidic devices.* **Zhou C., Yue P., Feng J. J.** 2006, Phys. Fluids, Vol. 18, pp. 1-14.

26. *Novel microreactors for functional polymer beads.* **Nisisako T., Torii T., Higuchi T.** 2004, Chem. Eng. J., Vol. 101, pp. 23-29.

27. *Generation of monodisperse particles by using microfluidics control over size, shape, and composition.* **Xu S., Nie Z., Seo M., Lewis P., Kumacheva E., Stone H. A., Garstechi P., Weibel D. B., Gitlin I., Whitesides G. M.** 2005, Angew. Chem. Int. Ed., Vol. 44, pp. 724-728.

28. *Monodisperse double emulsions generated from a microcapillary device.* **Utada A. S., Lorenceau E., Link D. R., Kaplan P. D., Stone H. A., Weitz D. A.** 2005, Science, Vol. 308, pp. 537-541.

29. *Nucleation rate measurement of colloidal crystallization using microfluidic emulsion droplets.* **Gong T. Y., Shen J. Y., Hu Z. B., Marquez M., Cheng Z.** 2007, Langmuir, Vol. 23, pp. 2919-2923.

30. *A microfluidic system for controlling reaction networks in time.* **Song H., Tice J. D., Ismagilov R. F.** 2003, Angew. Chem. Int. Ed., Vol. 42, pp. 767-772.

31. *Microfluidic platform for the generation of organic-phase microreactors.* **Cygan Z. T., Cabral J. T., Beers K. L., Amis E. J.** 2005, Langmuir, Vol. 21, pp. 3629-3634.

32. *A droplet-based composite PDMS/glass capillary microfluidic system for evaluating protein crystallization conditions by microbatch and vapordiffusion methods with on-chip X-ray diffraction.* **Zheng B., Tice J. D., Roach L. S., Ismagilov R. F.** 2004, Angew. Chem. Int. Ed., Vol. 43, pp. 2508–2511.

33. *Production of titania nanoparticles by using a new microreactor assembled with same axle dual pipe.* **Takagi M., Maki T., Miyahara M., Mae K.** 2004, Chem. Eng. J., Vol. 101, pp. 269-276.

34. *Preparation of monodisperse SiO2 nanoparticles by membrane emulsification using ideally ordered anodic porous alumina.* **Yanagishita T., Tomabechi Y., Nishio K., Masuda H.** Langmuir, Vol. 20, pp. 554-555.

35. *Quantitative extraction using flowing nano-liter droplet in microfluidic system.* **Kumemura M., Korenaga T.** 2006, Anal. Chim. Acta, Vol. 558, pp. 75-79.

36. *Microfluidic liquid–liquid extraction system based on stopped-flow technique and liquid core waveguide capillary.* **Sun M., Du W. B., Fang Q.** s.l. : 70, Talanta , pp. 392–396.

37. *Periodic generation and transport of micro air bubble in co-flowing of water in microchannels.* **Quan X., Chen G., Cheng P.** 2010, International Communications in Heat and Mass Transfer, Vol. 37, pp. 992–997.

38. *Production of monodispersed micron sized bubbles at high rates in a microfluidic device.* **Chen c., Zhu y., Leech P. W., Manasseh R.** 2009, Appl. Phys. Lett., Vol. 95, p. 144101.

39. *Preparation of a Micro-Porous Alginate Gel Using a Microfluidic Bubbling Device.* **Martynov S., Wang X., Stride E. P., Edirisinghe M. J.** 2010, International Journal of Food Engineering, Vol. 6, pp. 1-12.

40. *Perspectives on foam drainage and the influence of interfacial rheology.* **Stone H. A., Koehler S. A., Hilgenfeldt S., Durand M.** 2003, J. Phys.: Condens. Matter, Vol. 15, p. S283.

41. *Bubble diameter on detachment in flowing liquids.* **Al-Hayes R. A. M., Winterton R. H. S.** 1981, Int. J. Heat Mass Transfer, Vol. 24, pp. 223-230.

42. *Volume of a bubble formed at a single submerged orifice in flowing liquid.* **Tsuge H., Hibino S. I., Nojima Y.** 1981, Int. Chem. Eng., Vol. 21, pp. 630-635.

43. *Bubble size prediction in co-flowing streams.* **Hoeve W., Dollet B., Gordillo J. M., Versluis M., Lohse D.** 2011, EPL, Vol. 94, pp. 64001-6.

44. *Perfectly monodisperse microbubbling by capillary flow focusing.* **Ganan-Calvo A. M., Gordillo J. M.** 2001, Phys. Rev. Lett., Vol. 87, pp. 274501-4.

45. *Monodisperse microbubbling: Absolute instabilities in coflowing gas–liquid jets.* **Gordillo J. M., Ganan-Calvo A. M., Perez-Saborid M.** 2001, Phys. Fluids, Vol. 13, p. 3839.

46. *Designer emulsions using microfluidics.* **Shah R. K., Shum H. C., Rowat A. C., Lee D., et. al.** 2008, materialstoday, pp. 18-27.

47. *Droplet microfluidics.* **Teh S., Lin R., Hung L., Lee A. P.** 2007, Lab on a Chip, pp. 198-220.

48. *Reactions in droplets in microflulidic channels.* **Song H., Chen D. L., Ismagilov R. F.** 2006, Angew. Chem. Int. Ed. Engl., pp. 7336-7356.

49. *Using nanoliter plugs in microfluidics to facilitate and understand protein crystallization.* **Zheng B., Gerdts C. J., Ismagilov R. F.** 2005, Angew. Chem., Int. Ed., pp. 2520-2523.

50. *Formation of Droplets of Alternating Composition in Microfluidic Channels and Applications to Indexing of Concentrations in Droplet-Based Assays.* **Bo Zheng, Joshua D. Tice and and Rustem F. Ismagilov.** 2004, Anal. Chem., pp. 4977-4982.

51. *Ordered and disordered patterns in two-phase flows in microchannels.* **Dreyfus R., Tabeling P., Willaime H.** 2003, Phys. Rev. Lett., pp. 1-4.

52. *Simulation of a microfluidic flow-focusing device.* **Dupin M. M., Halliday I., Care C. M.** 2006, Phys. Rev., pp. 1-4.

53. *Three-dimensional lattice Boltzmann simulations of droplet formation in a cross-junction microchannel.* **Wu L., Tsutahara M., Kim L. S., Ha M.** 2008, Int. J. Multiphase Flow, pp. 852-864.

54. *Generation of steady liquid microthreads and micron-sized monodisperse sprays in gas streams.* **M., Ganan-Calvo A.** 1998, Phys. Rev. Lett., pp. 285-288.

55. *Monodisperse Emulsion Generation via Drop Break Off in a Coflowing Stream.* **Umbanhowar P. B., Prasad V., Weitz D. A.** 2000, Langmuir, pp. 347-351.

56. *Scaling the drop size in coflow experiments.* **Castro-Hernández E., Gundabala V., Fernández-Nieves A., Gordillo J. M.** 2009, New Journal of Physics, Vol. 11, p. 075021.

57. *Microbubbles: a novel delivery system.* **Kurup N., Naik P.** 2010, Asian Journal of Pharmaceutical Research and Health Care, pp. 228-234.

58. *Study of microbubble generation by a swirl jet.* **Tabei K., Haruyamu S., Yamaguchi S., Shirai H., Takakusagi F.** 2007, Journal of Environment Engineering, pp. 172-182.

59. *Microbubble generation and microbubble-aided transport process intensification—A state-of-the-art report.* **Parmar R., Majumder S. K.** 2013, Chemical Engineering and Processing:Process Intensification, pp. 79-97.

60. *Preparation of polymeric microbubbles: formation studies and product characterization.* **Bjerknes K., Sontuam P. C., Smistad G., Agerkvist I.** 1997, International Journal of Pharmaceutics, pp. 129-136.

61. *Formation of bubbles and droplets in microfluidic systems.* **Garstecki P., Ganan Calvo A. M., Whitesides G. M.** 2005, Bulletin of the Polish Academy of Science: Technical Sciences, pp. 361-372.

62. *Interfacial tension driven monodispersed droplet formation from microfabricated channel array.* **Sugiura S., Nakajima M., Iwamoto S., Seki M.** 2001, Langmuir, pp. 5562-5566.

63. *Formation of bubbles and foams in gelatin solutions within a vertical glass tube.* **Skurtys O., Bouchon P., Aguilera J. M.** 2008, Food Hydrocolloids, Vol. 22, pp. 706-714.

64. *Monodispersed microbubble formation using microchannel technique.* **Yasuno M., Sugiura S., Iwamoto S., Nakajima M.** 2004, AIChE Journal, pp. 3227-3233.

65. *Electrochemically controlled formation and growth of hydrogen nanobubbles.* **Zhang L., Zhang Y., Zhang X., Li Z., Shen G., Ye M., et al.** 2006, Langmuir, pp. 8109-8113.

66. *The membrane emulsification process - a review.* **Charcosset C., Limayem I., Fessi H.** 2004, Journal of Chemical Technology and Biotechnology, Vol. 79, pp. 209-218.

67. *Recent developments in manufacturing emulsions and particulate products using membranes.* **Vladisavljevic G. T., Williams R. A.** 2005, Advances in Colloid and Interface Science, Vol. 113, pp. 1-12.

68. *Size control of nanobubbles generated from Shirasu-porous-glass (SPG) membranes.* **Kukizaki M., Goto M.** 2006, Journal of Membrane Science, Vol. 281, pp. 386-396.

69. *Effect of pre-heating on the foaming properties of whey protein isolate using a membrane foaming apparatus.* **Bals A., Kulozik U.** 2003, International Dairy Journal, Vol. 13, pp. 903-908.

70. *The influence of pore size, the foaming temperature and the viscosity of the continuous phase on the properties of foams produced by membrane foaming.* **Bals A., Kulozik U.** 2003, Journal of Membrane Science, Vol. 220, pp. 5-11.

71. *Experiments and modeling on electrochemically generated bubbly flows.* **Wedin R., Davoust L., Cartellier A., Byrne P.** 2000, Experimental Thermal and Fluid Science, Vol. 27, pp. 685-696.

72. *Characterization of gellan/gelatin mixed solutions and gels.* **Lee K. Y., Shim J., Bae I. Y., Cha J., Park C. S., Lee H. G.** 2003, Lebensm.-Wiss. u.-Technol, Vol. 36, pp. 795-802.

73. *The effect of surface active solutes on bubble coalescence in the presence of ultrasound.* **Lee J., Kentish S. E., Ashokkumar M.** 2005, Journal of Physical Chemistry, Vol. 109, pp. 5095-5099.

74. *Acoustic cavitation and its chemical consequences.* **Suslick K. S., Didenko Y., Fang M. M., Hyeon T., Kolbeck K. J., McNamara W. B., Mdleleni M. M., Wong M.** 1999, Philosophical Transaction of the Royal Society A, pp. 335-355.

75. *Ultrasound-Assisted Generation of Foam.* **Lim K. S., Barigou M.** 2005, Ind. Eng. Chem. Res., Vol. 44, pp. 3312-3320.

76. *Structural and functional changes in ultrasonicated bovine serum albumin solutions.* **Gu lseren I., Guzey D., Bruce B. D., Weiss J.** 2006, Ultrasonics Sonochemistry, pp. 173-183.

77. *Sonochemistry: science and engineering.* **Thompson L. H., Doraiswamy L. K.** 1999, Industrial & Engineering Chemistry Research, Vol. 38, pp. 1215-1249.

78. **P., Walstra.** *Physical Chemistry of Foods.* s.l. : Marcel Dekker, Inc, 2003.

79. **Gennes P. G., Brochard-Wyart F., Quéré D.** *Capillarity and Wetting Phenomena: Drops, Bubbles, Pearls, Waves.* s.l. : Springer, New York, 2004.

80. *The effect of the hydrophobicity of microchannels and components in water and oil phases on droplet formation in microchannel water-in-oil emulsification.* **Kawakatsu T., Trägårdh G., Trägårdh C., Nakajima M., Oda N., Yonemoto T.** 2001, Colloids and Surfaces A: Physicochemical and Engineering Aspects, pp. 29-37.

81. *Generation of highly uniform droplets using asymmetric microchannels fabricated on a single crystal silicon plate: Effect of emulsifier and oil types.* **Vladisavljevic G. T., Kobayashi I., Nakajima M.** 2008, Powder Technology, pp. 37-45.

82. *Microchannel Emulsification: From Computational Fluid Dynamics to Predictive Analytical Model.* **van Dijke K. C., Schroën K. C. G. P. H., Boom R. M.** 2008, Langmuir, pp. 10107-10115.

83. *EDGE emulsification for food-grade dispersions.* **Dijke K. C., Schroën K., Padt A., Boom R. M.** 2010, Journal of Food Engineering, pp. 348-354.

84. *Experimental comparative mixing performance of passive micromixers with H-shaped sub-channels.* **Nimafar M., Viktorov V., Martinelli M.** 2012, Chemical Engineering Science, pp. 37-44.

Chapter 10. Conclusion

The development of high-quality foods with desirable properties for both consumers and food industries requires a comprehensive understanding and rational design of food micro-structures. The overall processes, including texture, flavor and keeping qualities of food are controlled not only by chemical composition, but also by how the various ingredients are distributed and interact at microscopic length scales. The size, shape and distribution of various ingredients structures greatly influence product quality, stability as well as sensory properties. For these reasons, the designs of new devices for the food manufacturing and characterization as well as the optimization of existing ones are highly desirable. In this context, the adoption of microfluidic technology will change the intervention scale and produce significant improvements.

This work addresses design and characterization of novel micro-devices that have potential applications in food industries and is focused on (i) efficient micromixing, and (ii) production of mono-dispersed microdroplets and microbubbles.

This thesis presents a novel design mechanism of passive microfluidic mixers based on the SAR process, meaning that the two fluids to be mixed are split and recombined successively at each element of a mixer. Mixing of fluids at the micro-scale possess a variety of challenges, many of which arise from the fact that molecular diffusion is the dominant transport mechanism in the laminar flow regime. Though, prior works reported the effectiveness of SAR based micromixers at low Reynolds numbers, more work is required to assess the performance of new SAR based micromixers at a wide range of Reynolds numbers.

Two new micromixers, “H-C” and “Y-Y”, were designed and analyzed. Through folding, rotation, expansion and contraction, along with splitting and recombination processes these mixers cause the formation of a large number of different vertical and horizontal layers of fluids and consequently, minimize diffusion length and maximize mixing performance. The prototypes of the mixers were obtained by micromilling one sheet of polycarbonate foil and providing connecting holes on two other sheets; since there are no obstacles or grooves inside the channel, the manufacturing procedure is simple and cost effective. The performance of the new micromixers was compared to those of two well-known SAR mixers, the Chain and the Tear-drop. Fluid dynamics, mixing

efficiency and pressure drop were studied experimentally and numerically at Reynolds numbers ranging from 1 to 100. Dependency of mixing performance on different inlet flow-rate ratios (1 to 3) was also investigated. An image analysis technique was used to evaluate mixture homogeneity at four target areas (after each element) along the mixer and the experimental results show a good agreement with data obtained by CFD. Among the four micromixers examined, the Chain mixer presents relatively low mixing efficiency at low- and mid-range of Reynolds numbers ($1 \leq Re \leq 45$) while the Tear-drop provides fairly good efficiency except at the middle range of Reynolds numbers ($20 \leq Re \leq 45$). Conversely, the H-C and the Y-Y mixers show an almost flat mixing characteristic over the whole range of Reynolds numbers with a mixing efficiency higher than 90%. Moreover, the mixing efficiencies of the H-C and the Y-Y mixers after second element are higher than that of the other two mixers after fourth element. This is due to the contribution of secondary transverse flow inside the H-C and Y-Y mixers after each element. The effect of inlet flow-rate ratios on the mixing performance varies from one mixer to another. The Chain mixer shows notable dependency on the inlet flow-rate ratios at low Reynolds numbers but the Tear-drop mixer has a significant dependency generally at mid-range of Reynolds numbers. Whereas, both H-C and Y-Y mixes has slight dependency on the inlet flow-rate ratios. It is also found that with the increasing Reynolds numbers, pressure-drop increases for all mixers. Moreover, the Y-Y and the H-C mixers provide much lower pressure-drop among the examined mixers. In addition, RTD analysis at low, middle and high Reynolds numbers confirm that both Y-Y and H-C micromixers have better performance than other two mixers.

The outcomes of the first part of this work pointed out that both new geometries satisfy the design goals of micromixer, namely to keep higher mixing efficiency reducing the channel length and to decrease the pressure-drop. These significant developments can be exploited to design new mixer which will enhance the fluid mixing performance while keeping a low pressure-drop even in case of laminar flow.

Though two-phase microfluidics has obtained enormous attentions lately, its application to microfluidic devices still considered in an immature stage and immense efforts have to be dedicated in the development of more reliable, stable and controllable products. It remains therefore very important to understand and utilize microfluidics fundamentals to design and develop improved micro-devices for many applications.

Two new 2D T-junction and two new 3D H devices were designed and investigated for the creation and manipulation of mono-dispersed droplets and bubbles. The prototypes (T-1, T-2, H-1 and H-2)

were made of a central lamina and two covers, mounted one after another; the central polycarbonate lamina contained the micromilled structure and two covers hosted the inlets and the outlet ports. Production of water droplet in silicone oil (W/O) and air bubble in silicone oil (A/O) were studied using two experimental setups for flow rate from 10 ml/h to 230 ml/h. In the experimental tests, two flow regimes (squeezing and dripping) are observed over a broad range of Capillary numbers (0.01~0.18) inside four devices. Size of droplet and bubble depends strongly on the flow rate of continuous phase rather than the dispersed phase. Moreover, droplet size is relatively large at low continuous flow rate and coalescence took place inside the tank, due to the absence of surfactant; as the continuous flow rate increases more uniform droplets were found. Among the four devices, T-1 and T-2 produce around 100 µm size drops which are four times smaller than the device dimension. In addition, T devices also has relatively high droplet production rate. Positive pressure and negative pressure experimental methods were used to produce air bubble in four different micro-devices. As expected, mean bubble size was found to decrease with increasing continuous flow rate and around 120 µm size bubble was found at a high flow rate (Q_c = 230 ml/h). Moreover, negative pressure setup provides more robust bubble production than positive pressure setup. In contrary, positive pressure setup generates more bubble per unit time than negative pressure setup due to its higher effective flow rate inside the microchannel.

We believe that this study will foster the current knowledge of the design method of micro-devices and will be instrumental in the fulfillment of specific requirements in industrial applications; it will also enhance the understanding of microfluidic technology and its applications to the production of food grade emulsions and foams.

The End